

# Stochastic and reduced order modelling of the wake behind wind turbine towers



jim DTU Wind-0982 July 2025

## Author: iim

#### Title:

Stochastic and Reduced Order Modelling of the Wake behind Wind Turbine Towers

**DTU Wind-M-0982** July 2025

ECTS: 45

Education: Master of Science

Supervisor(s):

Søren Juhl Andersen Christian Grinderslev **DTU Wind & Energy Systems** 

Norbert Warncke
Siemens Gamesa Renewable
Energy

Richard Dwight **TU Delft** 

#### **Remarks:**

This report is submitted as partial fulfillment of the requirements for graduation in the above education at the Technical University of Denmark.

DTU Wind & Energy Systems is a department of the Technical University of Denmark with a unique integration of research, education, innovation and public/private sector consulting in the field of wind energy. Our activities develop new opportunities and technology for the global and Danish exploitation of wind energy. Research focuses on key technical-scientific fields, which are central for the development, innovation and use of wind energy and provides the basis for advanced education at the education.

**Technical University of Denmark** Department of Wind and Energy Systems Frederiksborgvej 399 4000 Roskilde
Denmark
www.wind.dtu.dk

## Stochastic and Reduced Order Modelling of the Wake Behind Wind Turbine Towers

Thesis Report

Jim Wijngaarde



## Stochastic and Reduced Order Modelling of the Wake Behind Wind Turbine Towers

Master's thesis in Wind Energy

Thesis report

by

## Jim Wijngaarde

to obtain the degrees of

Master of Science

in Wind Energy at Technical University of Denmark

Master of Science

in Aerospace Engineering at Delft University of Technology

to be defended publicly on July 24th, 2025

Thesis committee:

Chair: Prof. Dr. S. J. Watson TU Delft – Professor of Wind Energy Systems
Censor: TU Delft – Professor of Wind Energy Systems
TU Delft – Professor of Wind Energy Systems

Supervisors: Dr. N. G. W. Warncke Siemens Gamesa – Loads Engineer

Dr. R. P. Dwight
Dr. S. J. Andersen
Dr. C. Grinderslev

TU Delft – Associate Professor
DTU – Associate Professor
DTU – Assistant Professor

External examiner: TBD

Place: Faculty of Aerospace Engineering, Delft

Project duration: November 2024 – July 2025

Student number: TU Delft 5069785

DTU s233801

An electronic version of this thesis is available at http://repository.tudelft.nl/.







### Preface

This thesis marks the end of two year long journey that took me to Denmark twice. The experience has been immensely rewarding, and the challenges along the way have taught me a great deal about myself.

I have had the privilege to learn from distinguished professors and to meet so many amazing new people.

First and foremost, I thank Norbert Warncke, my daily supervisor at Siemens Gamesa, for his support and guidance. He continuously generously takes his time to present his expertise and offer assistance. I have often sat next to him poring over equations for more than an hour and have massively broadened the mathematical toolsets available to me through his explanations. He really takes his time for his students and I deeply appreciate his commitment.

Next, I want to express my gratitude to my academic supervisors, Søren Andersen, Christian Grinderslev and Richard Dwight. In our meetings we often laughed and joked and you were often very excited about the ideas I brought to the table. You gave me some clear directions what to try and what to avoid throughout the project and I am very grateful for the support.

Lastly, I want to my gratitude to everyone who I got the pleasure to play foosball against at the office. My skills in this area have massively improved. I have learned massively from the kinematics and dynamic effects that balls on a foosball table can exhibit. Often flying throughout the room with multiple hands extending to get a point reduction for the other team. The ball even flew out of the window once and we had to climb down six stories to retrieve it.

Throughout my time at Siemens Gamesa I felt appreciated and useful. I believe that what I have developed in this project may really be used one day. The experiences at this office have enhanced my skills and readiness to take on future endeavours.

Jim Wijngaarde Delft, July 2025

## Contents

Pr	eface		i
No	omen	clature	vi
1	Intr 1.1 1.2	Research Questions	1 1 2
<b>2</b>	${ m Lit}\epsilon$	erature Review	3
	2.1	Cylinder Wakes	$     \begin{array}{r}       3 \\       4 \\       5 \\       8 \\       9 \\       10 \\       12 \\       14 \\       16 \\     \end{array} $
3	Met	thodology	17
J	3.1	SBES simulation and data acquisition	17 17 19
	3.2	Quasi-2D Stochastic Reduced Order Modelling	$\frac{20}{20}$
	3.3	Extending 2D Flow Fields to 3D Using Correlated Fields  3.3.1 Multi-Layer Flow Representation	23 23 23 24 25
4	Res	sults	27
	4.1	Proper Orthogonal Decomposition	27 31
	4.2	Stochastic Reduced Order Model Results	35 35 36
	4.3	Verification of the frequency—shift hypothesis	38 38 39 39 44
	4.4	Verification and Fit of Correlation Coefficient	48 48 53 55

Contents

5	Stre	eam Function and Toroidal-poloidal Decomposition Modal Fitting	<b>58</b>
	5.1	Quasi-2D Modal Fitting Using Toroidal Stream Function Basis	58
	5.2	Basis Choices and the Joukowski Transform	59
		5.2.1 Choice of Modal Basis in the $\zeta$ -plane	60
		5.2.1.1 Enforcing the No-slip Condition	61
		5.2.1.2 Design Matrix with and without Constraint	62
	5.3	Error Quantification of Fits	63
		5.3.1 Local Percentage Speed Error	63
		5.3.2 Global Root-Mean-Square Error (RMSE)	64
		5.3.3 Dependence on $(N_x, N_y)$	64
		5.3.4 Impact of Stream Function Fits on the SROM Reconstruction	65
		5.3.5 Projection and Subspace Errors	67
6	Con	nclusions and Recommendations	69
	6.1	Conclusions	69
	6.2	Recommendations	70
Re	ferer	aces	<b>7</b> 2
$\mathbf{A}$	Spa	tial Modes	77
В	Proof that the Spectral Error Is Equivalent to a Variance Ratio		<b>7</b> 9
$\mathbf{C}$	Rot	ational Extension of the MAC Criterion	80
D	Der	ivation of mass conservation for Hermite stream function basis	81
${f E}$	Correlation Coefficient Fits		
$\mathbf{F}$	Spatial Modes RMSE Plots		

## List of Figures

2.1	Von Kármán vortex street. Reproduced from [7]	3
2.2	Boundary layer and wake around cylinder. Reproduced from [8] p. 3	4
2.3	Velocity and vorticity distribution in boundary layer. Reproduced from [8] p. 7	4
2.4	Strouhal number variation with Reynolds number for smooth and rough cylinder surfaces.	
	Reproduced from [11]	4
2.5	Effect of turbulence on the Strouhal number [14] p. 409	5
2.6	Spanwise shear on a cylinder [15] p. 19	6
2.7	Effect of shear in the approach flow on vortex-shedding frequency. Circles: Strouhal	
	number based on the centre-line velocity $U_c$ . Dashed lines: Strouhal number based on the	
	local velocity, $U_{\text{local}}$ . $Re = 2.8 \times 10^4$ . Shear steepness $s = 0.025$ . Reproduced from [15] p. 20	6
2.8	Photographs illustrating the time evolution of spanwise cell structure. $Re = 6 \times 10^6 = 3$ .	U
2.0	Reproduced from [15] p. 29	7
2.9	Lock in phenomena of spring mounted cylinder oscillating in air. Reproduced from [36] p.	'
2.9	13	8
2 10	Mode competition in the near wake of an oscillating cylinder	9
	Image compression of a dog using truncated SVD at various ranks $r$ . Reproduced from	9
2.11		10
0.10	[47] p.10	13
2.12	Schematic of Welch's method with blocks for estimating SPOD modes. Reproduced from	1.4
	[40] p. 831	14
3.1	2D surface cylinder surface	18
3.2	Refined wake mesh	18
$\frac{3.2}{3.3}$	Outer domain mesh	18
3.4	Quasi-2D simulation mesh points used for data acquisition	19
$3.4 \\ 3.5$	3D simulation mesh points used for data acquisition	19
3.6	Smooth flow. Reynolds number: $2 \times 10^4$ . Reproduced from [63] p. 289	$\frac{19}{25}$
3.7	Flow with 11% turbulence intensity. Reynolds number: $2 \times 10^4$ . Reproduced from [63] p.	20
3.1	289	25
	209	20
4.1	First five POD modes of the velocity components $u, v$ , and $w$ for the quasi-2D simulation.	28
4.2	POD modes 6-10 of the velocity components $u, v$ , and $w$ for the quasi-2D simulation	29
4.3	Power spectral density (PSD) of the quasi-2D modal time series at 19 m s <sup>-1</sup>	30
4.4	Power spectral density (PSD) of the 3D stationary cylinder modal time series at 19 m s <sup>-1</sup>	31
4.5	First three POD modes of the velocity components $u$ , $v$ , and $w$ for the stationary cylinder	01
1.0	at $19 \text{ ms}^{-1}$	33
4.6	POD modes 4-6 of the velocity components $u$ , $v$ , and $w$ for the stationary cylinder at 19	55
1.0	$^{-1}$	34
4.7	Singular values and cumulative energy of quasi-2D POD modes at 19 m s <sup>-1</sup>	35
4.8	Turbulent kinetic over an average of 30 stochastic realisations	36
4.9	Singular values and cumulative energy of 3D flow case at slice height $Z/D = 1.6$ of	00
4.0	stationary cylinder	37
4.10	Stationary 3D simulation turbulent kinetic over an average of 30 stochastic realisations.	37
	Leading u-component POD spatial mode at two wind speeds	38
	PSDs of the temporal modes of the 11 and 19 m s <sup>-1</sup> datasets	38
	Modes 1-4 of POD basis from $15 \text{ m s}^{-1}$ case alongside Grassmann-interpolated basis	40
	Modes 5-8 of POD basis from 15 ms <sup>-1</sup> dataset alongside Grassmann-interpolated basis.	40
	u-component of the first mode of the full Grassmann interpolated space	41
	Effect of a 45° phase rotation on the first member of an oscillatory mode pair. The vortex	41
4.10	pattern is shifted in phase by a quarter cycle	42
	parrier is surried in phase by a quarter cycle	$\pm 2$

List of Figures

$4.18 \\ 4.19$	Modal assurance criterion (MAC) as function of planar rotation angle Average modal assurance criterion MAC of different mode pairs PSDs of the stretched $19~{\rm ms^{-1}}$ dataset and the temporal modes from the $15~{\rm ms^{-1}}$ dataset. TKE error of 20 modes cut-off original $15~{\rm ms^{-1}}$ flow and Grassmann mode interpolated	43 43 44
4.22 4.23 4.25 4.24 4.26 4.27 4.28	flow	45 45 46 47 48 49 52 53
5.1 5.2 5.3 5.4	2a/D = 0.2. Cartesian coordinates (physical plane)	56 59 59 60
5.5 5.6 5.7	$N_x=20,\ N_y=20,\ \eta_0=4.$	<ul><li>63</li><li>64</li><li>65</li><li>67</li></ul>
	First four 11 ms <sup>-1</sup> dataset POD modes of the velocity components $u$ , $v$ , and $w$ 11 ms <sup>-1</sup> dataset POD modes 5-10 of the velocity components $u$ , $v$ , and $w$	77 78
E.1 E.2	Correlation coefficient fitting use MSE and SPL curves of oscillating cylinder with $2a/D=0.1$ . Correlation coefficient fitting use MSE and SPL curves of stationary cylinder	82 83
F.1 F.2	RMSE for remaining spatial modes 5-10	84 85

## Nomenclature

#### List of Abbreviations

Abbreviation Definition			
CFD	Computational Fluid Dynamics		
CSD	Cross-Spectral Density		
DES			
DMD	Dynamical Mode Decomposition		
FFT	Fast Fourier Transform		
IFFT	Inverse Fast Fourier Transform		
LES	Large Eddy Simulation		
MAC	Modal Assurance Criterion		
MSE	Multiplicative Stretched Exponential (correlation-decay model)		
POD	Proper Orthogonal Decomposition		
PPOD	Permuted Proper Orthogonal Decomposition		
PSD	Power Spectral Density		
QR Orthogonal-upper-triangular matrix factorisation (thin QR de			
	position)		
RANS	Reynolds-Averaged Navier–Stokes		
RMSE Root Mean Square Error			
ROM	Reduced Order Model		
SBES	Stress-Blended Eddy Simulation		
SPL Stretched Power Law (correlation-decay model)			
SPOD	Spectral Proper Orthogonal Decomposition		
SROM	The state of the s		
St Strouhal number			
SVHT	Singular-Value Hard Threshold		
SVD	Singular Value Decomposition		
TKE	Turbulent Kinetic Energy		
WLSQ Weighted Least-Squares (fitting)			

## List of Latin Symbols

Symbol	Definition
$\overline{A}$	Data matrix whose columns are snapshot vectors of the flow field
$A^{(z_i)}$	Data matrix belonging to slice at height $z_i$
$A_{ m reconstruction}$	Reconstructed data matrix: $U_k \Sigma_k V_{\text{new},k}^{T}$
$A_{ m combined}$	Combined data matrix from five height slices (eq. 4.17)
$A_{ m realisation}$	Randomised realisation matrix, $U_k \Sigma_k V_{\text{new},k}^{T}$
$A_{\rm realisation, Grassmann}$	Realisation using Grassmann-interpolated basis (eq. 4.15)
B	Projection of $U_{19}^{(k)}$ onto tangent space at $U_{11}^{(k)}$ (eq. 4.9)
$B_n(\xi), B_m(\eta)$	One-dimensional basis functions in the $\xi$ - and $\eta$ -directions
β	Time-stretch factor for transplanting modes (eq. 4.14)
$\mathcal{B}_k$	Block-diagonal special-orthogonal set of in-plane rotation matrices
$b_j$	Coefficient related to initial conditions in DMD
$\tilde{C}$	Autocovariance matrix $C = A^{T} A$
C(k,x)	Pearson correlation of temporal coefficients (mode $k$ , separation $x$ )

List of Figures vii

$C_{mn}$	Correlation coefficient between heights $z_m$ and $z_n$
D	Characteristic diameter (e.g. of a cylinder or tower)
$D_r$	Diagonal weighting matrix with entries $(D_r)_{ii} = r_i$
	Normalised spectral-error metric between realisations $i$ and $j$
$E_{S_{-i,j}}$	Local percentage speed error at point $i$ (eq. 5.19)
$e_i$	Frequency (e.g. vortex-shedding frequency)
f	
$f_0$	Natural (unforced) vortex-shedding frequency of a stationary cylinder
£	der  Enternal faming fraguency applied to the cylinder motion
$f_e$	External forcing frequency applied to the cylinder motion
$f_n$	Shedding frequency for flow $n: St U_n/D_n$ Structural vibration (forcing) frequency of the cylinder
$f_{ m vib}$	`
$f_{\mathrm{ref}}$	Reference shedding frequency of a temporal mode
$f_{m{\star}}$	Target shedding frequency after frequency matching Fourier-transform operator
$\mathcal{F}^{-1}$	Inverse Fourier-transform operator
H(f)	Lower-triangular matrix in $S(f) = H(f)H^{H}(f)$
$I_{v}$	Turbulence intensity, $I_{\nu} = \sqrt{\tilde{u}^2}/\bar{u}$
$\mathbf{J}(x,y)$	Jacobian matrix of the Joukowski map (eq. 5.8)
k A . (E)	Mode cut-off Integrated Laguerre function (eqs. 5.6)
$egin{array}{l} \Lambda_k(\xi) \ L \end{array}$	Number of snapshots (time steps)
L (corr.)	Correlation length of span-wise vortex-shedding cells, $L =$
L (coll.)	$\int_0^\infty R(z) dz$
$L_c$	Vertical correlation length
$L_c$ $L_k(\xi)$	Laguerre polynomial of order $k$
M	Number of spatial points in analysis
M (overlap)	Mode-overlap matrix $M = (U_{11}^{(k)})^T U_{19}^{(k)}$
N(f)	Realisation of white noise at frequency $f$
$N_s$	Total number of spatial sample points
n	Index of retained modes or flow planes
$P(\mathbf{x})$	Poloidal scalar potential
$P_z$	Permutation matrix in MAC calculation
$\mathcal{P}_{k}^{\tilde{c}}$	Set of all $k \times k$ permutation matrices
q(x,t)	Generic flow quantity (e.g. velocity)
$r_i$	Radial coordinate of the <i>i</i> -th grid point
$r_k$	Weight factor $\sqrt{\Gamma(N_x+1)/\Gamma(k+1)}$ (eq. 5.15)
$\overset{\sim}{Re}$	Reynolds number, $Re = UD/v$
R	Cylinder radius used in scaling of $\zeta$
R(z)	Span-wise correlation coefficient of surface-pressure fluctuations
S	Shear-steepness parameter $s = D U_c^{-1} du/dz$
S(f)	Full cross-spectral density matrix
$S_t$	Strouhal number, $S_t = fD/U$
$\mathbf{S}_{ij}(f)$	Cross-spectral block between flows $i$ and $j$
$\mathbf{S}_{nn}(f)$	Auto-spectral density matrix for flow $n$
$\Sigma_{ m combined}$	Singular-value matrix of $A_{\text{combined}}$
T	Total number of time steps
$T(\mathbf{x})$	Toroidal scalar potential (stream-function)
$T_{N_x,N_y}(\xi,\eta)$	Truncated toroidal stream-function expansion (eq. 5.4)
u, v, w	Velocity components in $x, y, z$ directions
u', v', w'	Fluctuating velocity components
$u_{\mathrm{inf}}$	Free-stream velocity used for MAC sweeps
U	Free-stream velocity / left singular vectors from SVD (context-
	dependent)
$U_c$	Centre-line velocity of a shear profile
$U_{ m local}$	Local approach-flow velocity at the measurement height
$U_{15}$	Spatial mode matrix at 15 m s <sup>-1</sup> (direct POD)

List of Figures viii

$U_{15, \mathrm{Grassmann}}$	Spatial mode matrix interpolated via Grassmann geodesic
$ ilde{U}$	Left singular vectors from the SVD of $\tilde{A}$
$V^{(n)}(t)$	Modal time series for flow at height $n$
$V^{T}$	Transpose of right singular-vector matrix from SVD
$V_{ m combined}^{\sf T}$	Right-singular-vector matrix of $A_{combined}$
W	Normalised interpolation parameter on the Grassmann manifold
w  (map)	Complex coordinate $w = f(\zeta) = \xi + i\eta$
x	Dimensionless vertical separation, $x = \Delta z/D$
$x_{\beta_n}(t)$	Time-stretched signal $x(t/\beta_n)$
$\hat{\mathbf{u}}(\mathbf{k})$	Fourier transform of velocity field
$\mathbf{u}'(\mathbf{x})$	Fluctuating velocity field
$ ilde{A}$	Radially-weighted data matrix, $\tilde{A}_{ij} = \sqrt{r_i} A_{ij}$
$\mathbf{X}^{(n)}(f)$	Fourier coefficients of dominant modes of flow $n$
X, X'	Snapshot matrices in DMD
$X^\dagger$	Pseudoinverse of $X$
$\mathbf{Z}(f)$	Coloured Fourier coefficient vector, $Z(f) = H(f)N(f)$
$\eta_0$	Width parameter of Hermite basis (eq. 5.7)
$W_n$	Weighted column sum enforcing $v_{\zeta}(0, \eta) = 0$ (eq. 5.9)
$arepsilon_{ m rms}^{(m)}$	Normalised global RMSE of spatial mode $m$ (eq. 5.20)
$\mathbf{R}(arphi)$	$2 \times 2$ rotation matrix advancing phase by $\varphi$ (eq. 4.12)

## List of Greek Symbols

Symbol	Definition
$\beta_n$	Scaling factor: $\frac{U_{ m ref}/D_{ m ref}}{U_n/D_n}$
$\Delta z$	Vertical separation between two measurement heights
$\eta$	Imaginary part of the mapped coordinate $(w = \xi + i\eta)$
$\lambda_j$	DMD eigenvalue associated with $\phi_i$
ω	Vorticity: $\omega = \frac{\partial v}{\partial x} - \frac{\partial u}{\partial y}$
$\omega_j$	Angular frequency of DMD mode $\phi_i$
$\phi_j$	DMD spatial mode
ψ̈́	Stream function
$\sigma_i$	Singular value $i$ , energy content of POD mode $i$
$\Sigma$	Diagonal matrix of singular values in the SVD of $A$
Θ	Principal angles (vector or diagonal matrix) between two POD sub-spaces
arphi	Phase-rotation angle (eq. 4.12)
	Spatial POD mode i
Ψi ξ ζ	Real part of the mapped coordinate $(w = \xi + i\eta)$
ζ	Complex coordinate in the scaled plane, $\zeta = (x + iy)/R$

1

## Introduction

As global demand for electricity continues to rise, the expansion of energy supply is imperative [1]. Moreover, the greenhouse gas emissions associated with fossil fuel combustion have intensified interest in sustainable alternatives such as wind energy. The ongoing electrification of numerous industries is also accelerating the transition from fossil fuels to green electricity generation.

The shift towards offshore wind turbine deployment has been gathering pace [2], as the potential for harnessing stronger, more consistent winds becomes increasingly attractive. However, the harsh offshore environment imposes significant challenges, with fatigue emerging as a critical design parameter [3]. Notably, research indicates that extreme wind is the most common factor leading to wind turbine tower failure [4], further emphasising the need for robust design and maintenance strategies. Fatigue-induced failures necessitate the replacement of turbine components—a process that is particularly expensive in offshore settings [5]. For instance, severe storms present extreme fatigue conditions that can lead to substantial damage.

One promising control strategy during storms involves reorienting the turbine so that the blades are positioned behind the tower. This is achieved by rotating the blades through 90° and turning the turbine head by 180°, thereby reducing the risk of blade—tower collisions as the blades flex away from the structure. To mitigate damage to the blade bearings, the blades turn gradually, although this occasionally results in the blades operating within the tower's wake. This configuration is referred to as the down-wind idling situation.

The interaction between the blades and the tower wake introduces oscillations in the structure and may induce dynamic modes, complicating the assessment of fatigue loading. Accurately quantifying these effects necessitates precise wake models that capture the intricate flow dynamics around the tower.

Although advanced high-fidelity simulations—such as Large Eddy Simulations (LES) and Reynolds-Averaged Navier—Stokes (RANS) models—can resolve detailed flow features, their computational expense limits their application across a broad parameter range. Likewise, data-driven models that merely replicate high-fidelity simulations offer limited additional insight. Consequently, there is a growing demand for stochastic realisations of the wake flow field that both preserve the statistical characteristics of high-fidelity models and generate unique flow instances at a significantly reduced computational cost.

In light of these challenges, this project seeks to investigate data-based stochastic reduced order models (SROMs) capable of generating stochastic realisations of the wake flow field. The aim of the project is to develop robust tools for generating stochastic tower wake realisations, ultimately enhancing load estimation accuracy.

#### 1.1. Research Questions

The goal of this research is to develop stochastic realisations of cylinder wake flow for turbine load simulations. The research questions must align with this project goal. Derived from this objective the research questions are focussed on the suitability and effectiveness of reduced order models for wind

1.2. Thesis Outline

turbine tower wake modelling. Furthermore, it is desirable to know what insights can be drawn from the reduced order modes. In line with this, the following research questions are formulated:

- 1. What insights into wake dynamics can be obtained from low-order reconstructions of the quasi-2D flow field?
- 2. How do the energy distribution and dominant flow modes in 3D compare with those in quasi-2D simulations?
- 3. Can reconstruction of tower wake flow through wake modes be considered a suitable approach to generate stochastic tower wake realisations?
  - (a) How does the accuracy of stochastic realisations change with changing Reynolds numbers?
  - (b) What are the specific challenges and limitations of a ROM for wind turbine tower wakes at high Reynolds numbers?

#### 1.2. Thesis Outline

This thesis is structured as follows. Chapter 2 provides an extensive review of the literature in cylindrical vortex shedding and the methods of reduced order models. Chapter 3 outlines the data used throughout the thesis and provides the numerical methods that are employed for the building of the wake models. Chapter 4 presents the results of the implementation of the wake models alongside modifications made to the models based on the intermediary results. Chapter 5 presents divergence-free fitting of stream functions to spatial modes. Lastly, chapter 6 present the conclusions and recommendations from the study.

## Literature Review

This chapter provides an overview of the dynamics of cylindrical wake shedding and Reduced Order Models (ROMs). For cylindrical wake shedding the focus is on high Reynolds number flows that are relevant for wind turbines. The chapter starts with a review of key literature on vortex shedding from cylindrical structures, with a focus on high Reynolds numbers relevant for wind turbine towers. Next the chapter introduces Reduced Order Models (ROMs), beginning with Proper Orthogonal Decomposition (POD), followed by Spectral Proper Orthogonal Decomposition (SPOD), and concluding with Dynamical Mode Decomposition (DMD). Finally the literature of this chapter is synthesized considering the goals of obtaining a low computational cost cylindrical wake model.

#### 2.1. Cylinder Wakes

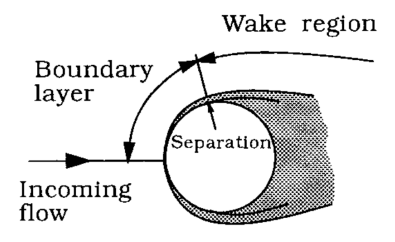
The canonical laminar wake behind a circular cylinder was first formalised through the von Kármán vortex street [6]. The fluid pressure on the surface of the cylinder fluctuates as vortices are shed alternately from either side of the cylinder. This repeated pattern of shed vortices are illustrated in figure 2.1. The alternating shedding causes oscillating lift and drag forces on the circular cylinder surface.

The mechanism which creates the shedding vortices can be explained by observing the boundary layer of the cylinder. The region around the cylinder contains two distinct regions, (i) in which the flow is attached and (ii) in which the flow is separated from the cylinder. Such separated flow is illustrated in figure 2.2. At the cylinder surface the flow velocity is zero and increases to the flow velocity at the outside of the boundary layer. Due to the friction in the boundary a 'roll-over' effect is seen and a vortex is shed from the cylinder. The phenomenon is illustrated in figure 2.3.



Figure 2.1: Von Kármán vortex street. Reproduced from [7]

2.1. Cylinder Wakes 4



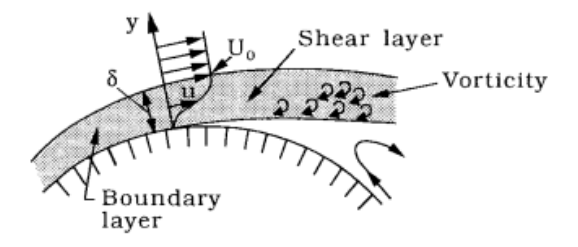


Figure 2.2: Boundary layer and wake around cylinder. Reproduced from [8] p. 3

**Figure 2.3:** Velocity and vorticity distribution in boundary layer. Reproduced from [8] p. 7

This effect was first described by Strouhal in 1878 [9] while investigating sound generated by wires experiencing vortex shedding. The non-dimensional Strouhal number  $S_t$  is named after him and is defined as in equation (2.1). Here f is the shedding frequency, D is the diameter of the cylinder and U is the free stream velocity.

$$S_t = \frac{fD}{U} \tag{2.1}$$

[10] summarizes the major regimes for flow across cylinders as a function of Reynolds number Re. These regimes range from fully attached flow at Re < 5 to a fully turbulent vortex street at  $Re > 3.5 \times 10^6$ . The Strouhal number can be seen as a function of Reynolds number in figure 2.4. In the subcritical range from  $Re = 500 - 10^5$  the Strouhal number is approximately constant at  $S_t \approx 0.2$ . In the range from  $Re = 1.1 \times 10^5 - 6.0 \times 10^6$  its value is heavily dependent on surface roughness.

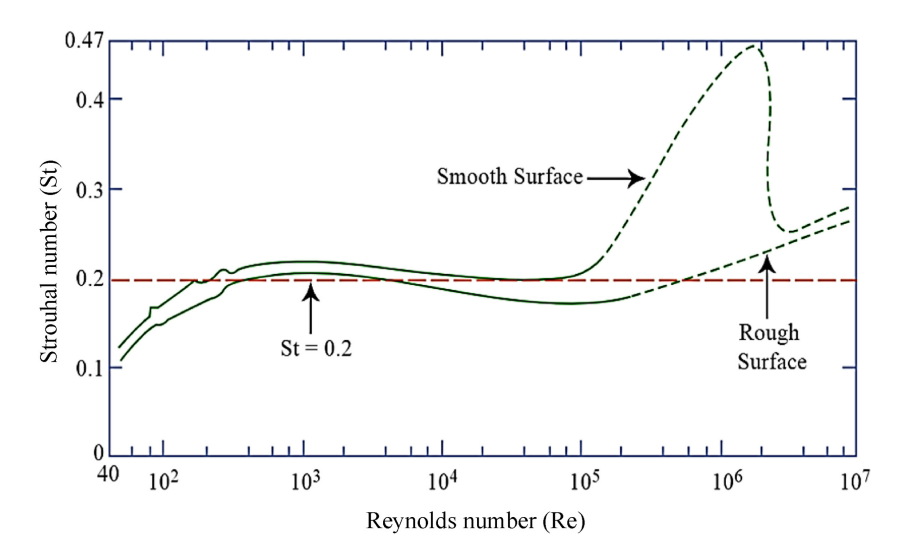


Figure 2.4: Strouhal number variation with Reynolds number for smooth and rough cylinder surfaces. Reproduced from [11].

At lower wind speeds the surface roughness can have a significant influence on the Strouhal numbers that occur on wind turbines. During a storm wind turbines will be in the transcritical vortex shedding regime.

#### 2.1.1. Transcritical Vortex Shedding

The transcritical regime is typically experienced by large wind turbine towers during storm conditions. Transcritical vortex shedding begins to occur at Reynolds numbers above  $5.9 \times 10^6$  [8]. At these high Reynolds numbers the Strouhal number no longer follows the predictable value of 0.2 seen in the subcritical regime. Wind tunnel experiments have measured vortex shedding characteristics up to  $18.7 \times 10^6$ , although these studies often involve compressible flow effects [12]. Notably, changes in Mach

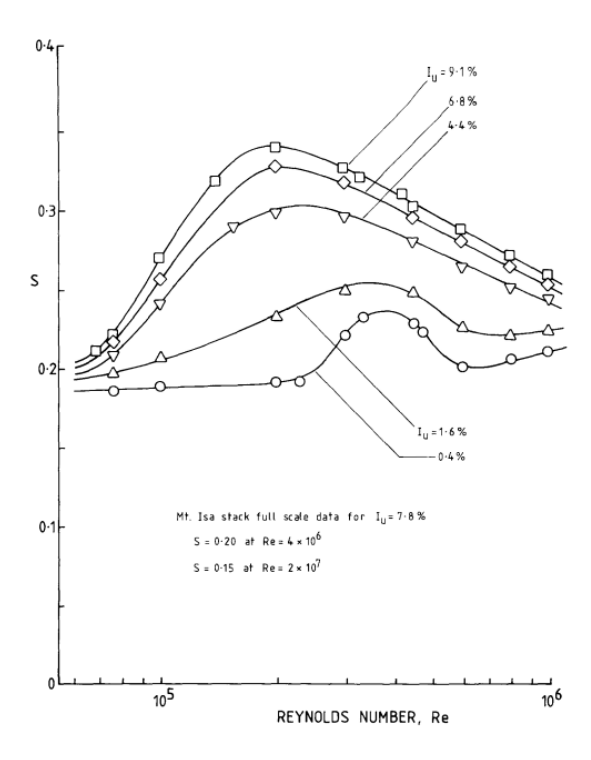


Figure 2.5: Effect of turbulence on the Strouhal number [14] p. 409

number at Reynolds numbers around  $2 \times 10^6$  can significantly impact the Strouhal number [12], below these Reynolds numbers the Mach number seems to have little effect. Different authors classify these high Reynolds number regimes differently; for example, [8] define upper transition at  $Re = 3.7 \times 10^6$ , transcritical onset at  $Re = 5.9 \times 10^6$ , and fully developed transcritical flow at  $Re = 7.1 \times 10^6$ . By contrast, [12] define three key regimes: wide-band random  $(1.1 \times 10^6 < Re < 3.5 \times 10^6)$ , narrow-band random  $(3.5 \times 10^6 < Re < 6.0 \times 10^6)$ , and quasi-periodic shedding  $(Re > 6.0 \times 10^6)$ . Despite differing nomenclature, these classifications describe the same fundamental flow phenomena. The main point of relevance for wind turbines is the broadening of the Strouhal peaks and the notable divergence from the predictable value of  $S_t \approx 0.2$ .

#### 2.1.2. Surface Roughness and Turbulence Intensity

Surface roughness is an important factor that contributes to vortex shedding in high Reynolds number regimes. It is well established that varying surface roughness significantly influences aerodynamic coefficients. [13] investigated the effect of surface roughness on the mean drag coefficient and Strouhal number. The Strouhal number at Reynolds numbers between  $1.1 \times 10^6$  and  $6.0 \times 10^6$  does not have a constant value and is strongly dependent on surface roughness.

The approaching wind flow also is an important factor influencing the flow around a cylinder. Namely the turbulence intensity and the shear in the spanwise direction of the cylinder. Turbulence intensity is defined as in equation (2.2). Here  $\sqrt{\tilde{u}^2}$  is the root-mean-square of the wind fluctuations and  $\bar{u}$  the mean wind velocity.

$$I_{\nu} = \frac{\sqrt{\tilde{u}^2}}{\bar{u}} \tag{2.2}$$

The effect of turbulence intensity is illustrated in figure 2.5. An increase of the turbulence intensity between  $10^5 < Re < 10^6$  increases the Strouhal number significantly compared to lower turbulence intensities.

Incoming shear flow on a cylinder is illustrated in figure 2.6. When shear is present in the spanwise direction of the cylinder vortex shedding takes place in spanwise cells [16]. In each cell the frequency is constant. In figure 2.7 it is seen that the shedding occurs in four cells, each with its own distinct

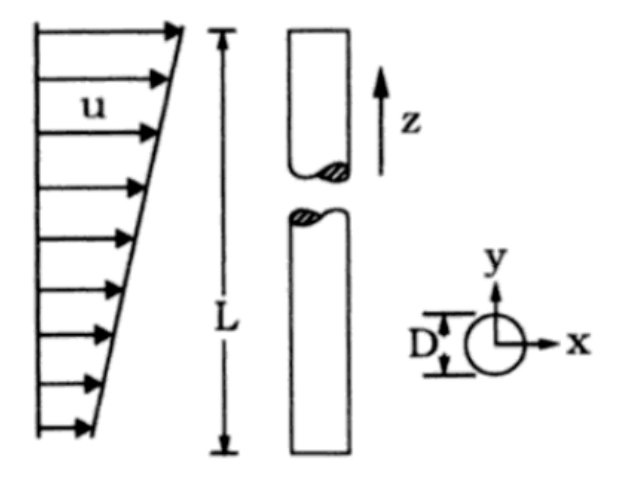


Figure 2.6: Spanwise shear on a cylinder [15] p. 19

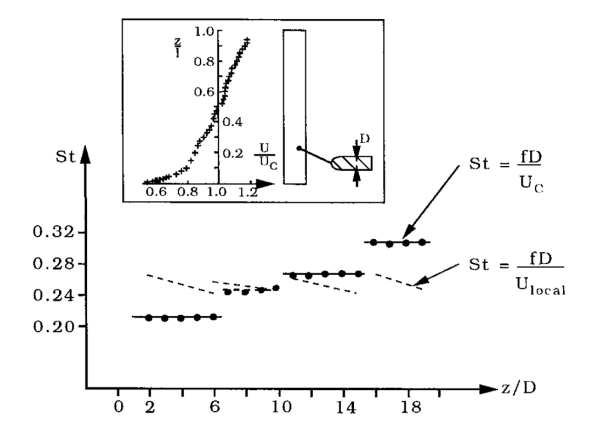


Figure 2.7: Effect of shear in the approach flow on vortex-shedding frequency. Circles: Strouhal number based on the centre-line velocity  $U_c$ . Dashed lines: Strouhal number based on the local velocity,  $U_{\text{local}}$ .  $Re = 2.8 \times 10^4$ . Shear steepness s = 0.025. Reproduced from [15] p. 20

frequency. When the Strouhal number is based on the local velocity (dashed lines in the figure), the data are grouped around the Strouhal number around 0.25.

The length of the cellular structures is correlated to the degree of the shear [15]. The trend is that the cell length decreases with increasing shear [16]. The parameter that defines this correlation is the shear steepness s which is defined in equation (2.3). Here D is the diameter of the cylinder,  $U_c$  the centre-line velocity and  $\frac{du}{dz}$  the change of local velocity over the height.

$$s = \frac{D}{U_c} \frac{du}{dz} \tag{2.3}$$

The spanwise cells structures are illustrated in figure 2.8. From the pictures it can be seen that the cells along the length span are out of phase. Consequently, spanwise variations in vortex phases reduce the overall aerodynamic forces compared to a scenario with fully coherent vortex shedding along the span. The average length of cells is referred to as the correlation length. The span-wise correlation coefficient R(z) is defined as in equation (2.4). Here  $\zeta$  is the span-wise reference position, z is the separation between two measurement points, p' is the fluctuating component of the relevant unsteady quantity (typically the surface pressure) and the over-bar denotes time-averaging.

2.1. Cylinder Wakes 7

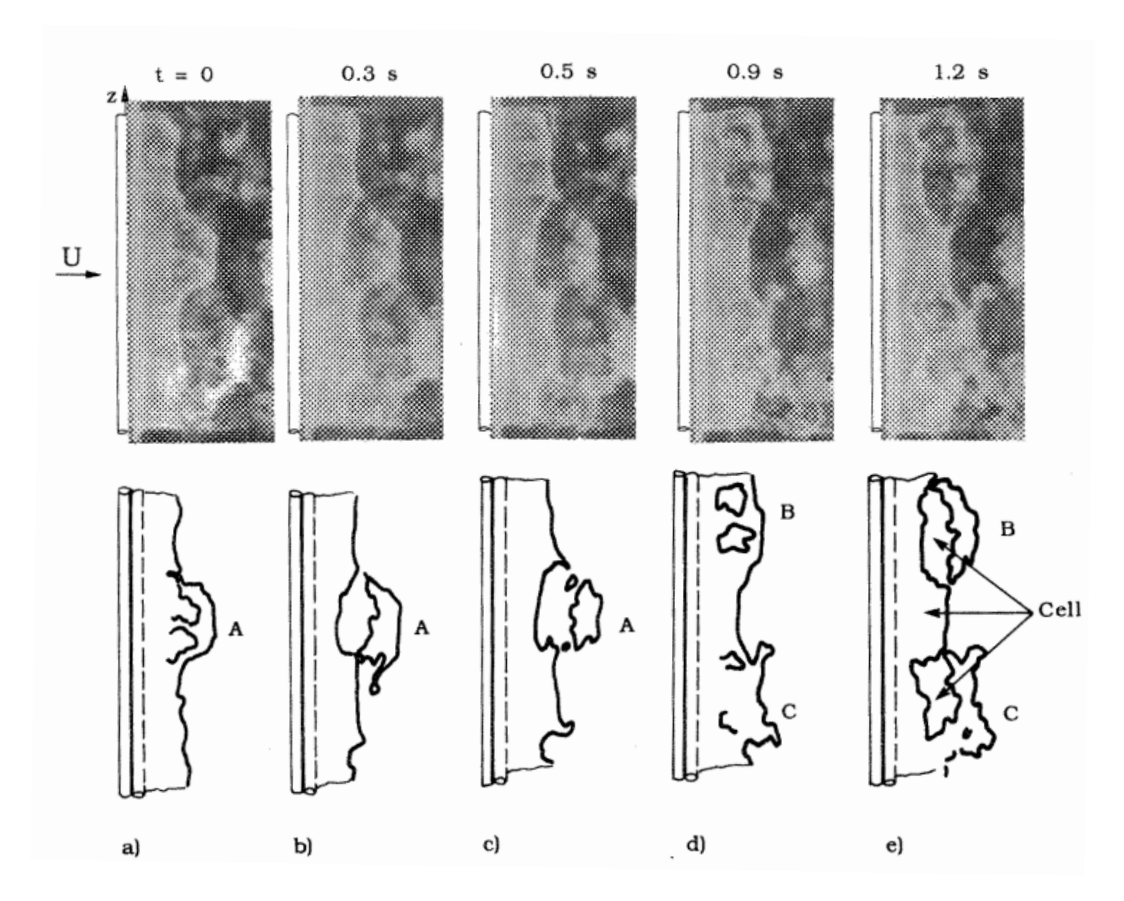


Figure 2.8: Photographs illustrating the time evolution of spanwise cell structure.  $Re = 6 \times 10^6 = 3$ . Reproduced from [15] p. 29

$$R(z) = \frac{\overline{p'(\zeta) \, p'(\zeta + z)}}{\sqrt{\overline{p'^2(\zeta) \, p'^2(\zeta + z)}}}$$
(2.4)

The correlation length L that characterises the average cell size is then obtained by integrating the correlation coefficient along the span as per equation (2.5).

$$L = \int_0^\infty R(z) \, \mathrm{d}z \tag{2.5}$$

The correlation of the aerodynamic forces has been demonstrated to follow an exponential decay for stationary cylinders [17], oscillating cylinders [18, 19] and oscillating cylinders near walls [20]. The correlation length increases with vibration amplitude and is further influenced by turbulence intensity. For smooth cylinders, the span-wise correlation length decreases with increasing Reynolds number [21]. Although the absolute Reynolds numbers in wind-tunnel tests are much lower than those of full-scale structures this trend is believed to continue for higher Reynolds numbers. To the author's knowledge the largest value for the correlation length reported in literature comes from a numerical study: a large-eddy simulation by [22], which estimated  $L/D \approx 1.1-1.3$  in the super-critical regime ( $Re = 4.1 \times 10^5-7.6 \times 10^5$ ).

Improved Delayed Detached Eddy Simulations (IDDES) have been performed at Reynolds numbers in the transcritical regime with  $Re = 8 \times 10^6$  [23, 24]. These simulations are however not performed for cylinders with sufficiently high aspect ratios to determine a correlation length. Neither paper quantifies the correlation and the Strouhal numbers in these simulations are not in line with measured Strouhal numbers at similar Reynold numbers.

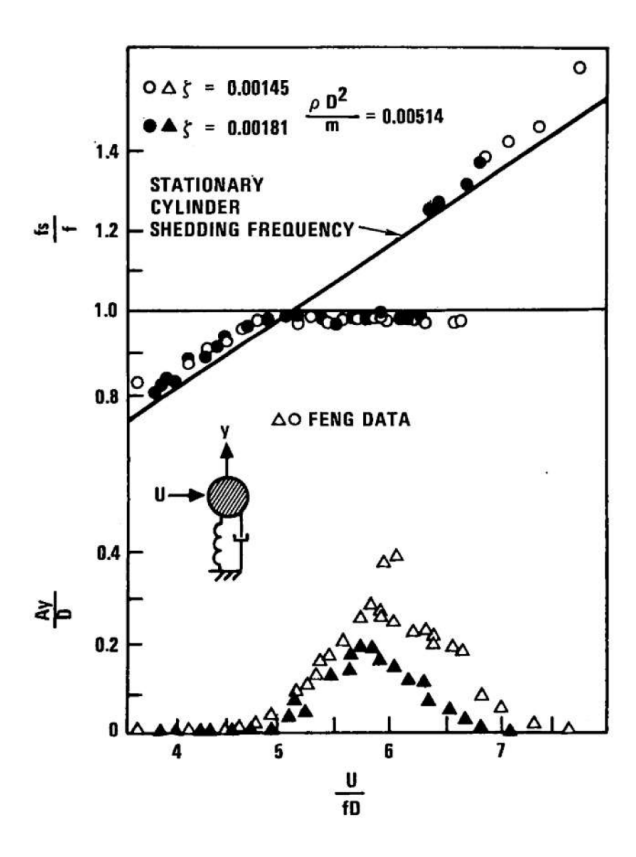


Figure 2.9: Lock in phenomena of spring mounted cylinder oscillating in air. Reproduced from [36] p. 13

#### 2.1.3. Influence of Cylinder Motion

Vortex shedding described by the relationship of equation (2.1) refers to stationary cylinders. Flexible structures such as turbine towers may vibrate continually altering the flow conditions. Consequently, the flow becomes more complex and the wake structure is modified.

According to [25], when the vibration frequency of the cylinder is close to or equal to the natural vortex shedding frequency, the interaction can have several significant effects on the wake structure:

- (i) Increase the strength of the vortices [26, 27],
- (ii) Increase the spanwise correlation of the wake [28, 18, 29],
- (iii) Dictate the vortex shedding frequency, leading to synchronisation with the vibration frequency of the cylinder (commonly referred to as "lock-in" or the "synchronisation effect") [30],
- (iv) Increase the mean drag force on the cylinder [30, 31],
- (v) Alter the phase, pattern, and sequence of vortices in the wake [32, 33, 34].

When the non-dimensional vibration frequency approaches the natural Strouhal shedding frequency, the wake may enter a narrow lock-in band. In this regime the shedding frequency no longer follows equation (2.1) but is dictated by the structural motion itself: vortex formation phases synchronise with the cylinder's oscillation, producing a single, coherent frequency in both the lift force and the displacement signal [35]. The lock in regime is usually defined as  $f_{\text{vib}}/f_s \approx 1$ , where  $f_{\text{vib}}$  is the oscillation frequency and  $f_0$  the vortex shedding frequency. In air the resulting vibrations occur very close to the natural frequency of the structure. This lock-in occurs over a range of velocities and this is referred to as the lock-in regime. An illustration of this is shown in figure 2.9. It may be seen that for  $\frac{U}{fD} \approx 5$  to  $\frac{U}{fD} \approx 6.5$  the ratio  $f_0/f = 1$ . Hence the vibration frequency matches shedding frequency in this velocity range.

Cylinders may further be oscillated in more than one direction. Dye-visualisation experiments by [34] show that the shape of the near wake depends strongly on how the cylinder is forced to move. Two

9

control parameters govern the outcome:

- (i) the forcing frequency, expressed as the ratio  $f_e/f_0$  to the natural shedding frequency, and
- (ii) the forcing direction, given by the angle  $\alpha$  between the motion vector and the free stream.

Depending on these two parameters the wake switches between one symmetric pattern (labelled S) and four anti-symmetric patterns (labelled A-I to A-IV). Pure cross-flow motion ( $\alpha=90^{\circ}$ ) locks the wake into the anti-symmetric A-I mode, while pure stream-wise motion ( $\alpha=0^{\circ}$ ) promotes competition between symmetric and anti-symmetric shedding until higher forcing frequencies ( $f_e/f_0 \gtrsim 3$ ) stabilise the symmetric mode. Mixed-direction forcing ( $0^{\circ} < \alpha < 90^{\circ}$ ) can cause rapid mode switching near  $f_e/f_0 \approx 1$ . Illustrations of these wake modes are shown in figure 2.10. Altering the oscillation direction or frequency can therefore change the wake pattern quite dramatically.



Figure 2.10: Visualisation of the preferred wake mode at five forcing frequencies  $(f_e/f_0 = 0.5, 1, 2, 3, 4)$  and four oscillation angles  $(\alpha = 0^{\circ}, 45^{\circ}, 60^{\circ}, 90^{\circ})$ . Reproduced from [34] p. 234.

#### 2.1.4. Full Turbine Towers and Diameter Scaling

To the author's knowledge, full-scale studies on towers are limited and all full-scale wind pressure measurement studies to determine coefficients have mostly been performed on rough surfaces. Real wind turbine towers are constructed from sections with decreasing diameter along their height, meaning local Reynolds numbers and Strouhal numbers vary significantly with elevation. These variations impact the vortex shedding dynamics and structural responses. [37] measured the effects of this on a full-scale wind turbine tower. For complete towers they distinguish between sectional (local) and global (whole structure) Strouhal numbers. The local spectral density of vortex shedding varies along the height due to changes in diameter and wind profiles.

Full-scale measurements have demonstrated that variations in atmospheric stability can cause significant

fluctuations in vortex shedding frequencies, with multiple Strouhal number peaks appearing in spectral analyses of lift coefficient data [38]. In stable atmospheric conditions, reduced turbulence leads to a more coherent vortex shedding pattern, resulting in a narrower frequency distribution. Conversely, unstable atmospheric conditions introduce higher turbulence intensities and increased wind shear, causing wider distributions in Strouhal numbers and amplifying vortex shedding variability along the structure's height. Additionally, wind shear modifies local Reynolds numbers along the tower, affecting synchronization of vortex shedding across different tower sections.

The correlation length increases with higher vibration amplitudes, meaning that sections of the cylinder experience vortex-induced forces more coherently when displacements are large [36]. In wind turbine towers, local variations in wind speed due to wind shear alter the synchronization of vortex shedding frequencies at different heights. Furthermore, the correlation length is highly dependent on atmospheric conditions, with stable conditions promoting more organized vortex shedding, whereas unstable conditions lead to a more stochastic shedding pattern.

Full-scale measurements have further shown that vortex shedding frequencies vary over short timescales, with multiple Strouhal peaks identified in lift coefficient spectra. These fluctuations are likely due to turbulence intensity, non-uniform atmospheric conditions, and structural response [37]. The presence of the rotor-nacelle assembly further alters vortex shedding characteristics, particularly when turbine blades are stationary versus rotating, highlighting the need to account for aerodynamic interactions with the blades in modelling vortex-induced vibrations in operational wind turbines.

Full scale turbine tower measurements are supported by wake-oscillator models, albeit at lower Reynolds numbers. [39] showed that even gentle tapering introduces a gradual shift in the local shedding frequency along the span, which fragments the Kármán street into shorter, mutually out-of-phase cells. The resulting loss of coherence in the fluctuating lift prevents the feedback mechanism required for classical lock-in, leading to markedly smaller vibration amplitudes compared with a uniform cylinder.

#### 2.2. Reduced Order Models

In this section, the focus is placed on Reduced Order Models (ROMs), a class of methods designed to simplify complex, high-dimensional systems. The section begins with a discussion of Proper Orthogonal Decomposition (POD), explaining how a flow field can be decomposed into a set of energetic modes that capture its dominant spatial structures. Building on this, Spectral Orthogonal Decomposition (SPOD) is introduced, which extends POD by incorporating time-dependent variations to separate different frequency components of the flow. Finally, Dynamical Mode Decomposition (DMD) is presented as a complementary technique that not only identifies coherent spatial patterns but also models their temporal evolution.

#### 2.2.1. Proper Orthogonal Decomposition

The large structures in a turbine simulated with advanced numerical methods can be reduced from time-resolved data. Proper orthogonal decomposition tries to find a set of modes or structures that capture the energy of the flow data. [40] mention the different formulations of POD including spectral proper orthogonal decomposition (SPOD) and space-only POD. Both methods have been applied for a variety of wake flows including turbulent jets [40], vertical axis wind turbines [41], cylinders [42] and wind farms [43].

The formulation transcribed and modified here is by [44]. They illustrate the POD method for an extrapolation finite difference scheme for the 2D parabolic equation.

In POD data at points in space at a specific moment in time are mapped and turned into a column vector. This data is typically referred to as realisations of a random process,  $\mathbf{q}$  [40, 45]. For applications in flow representation, this data is typically flow velocity or vorticity at points in space [46]. The column vectors are subsequently added next to each other to generate a matrix A as in equation (2.6). In equation (2.6), the snapshot matrix A is defined such that each column corresponds to a time snapshot and each row represents a spatial point. Each vector  $q = (u_0^j, u_1^j, \dots, u_m^j)^T$  contains all the realisations of the random process at a specific time snapshot j. For the application of wake flow, there are L snapshots or time steps taken and m data points in a 2D or 3D grid. Here  $L \ll m$ . This results in A being a tall, slender matrix.

$$A = \begin{bmatrix} u_1^1 & u_1^2 & \cdots & u_1^L \\ u_2^1 & u_2^2 & \cdots & u_2^L \\ \vdots & \vdots & \ddots & \vdots \\ u_m^1 & u_m^2 & \cdots & u_m^L \end{bmatrix}$$
(2.6)

Using singular value decomposition the matrix A can be represented as 3 matrices  $U, \Sigma$ , and  $V^T$  as in Equation 2.7. Here  $\Sigma_{l\times l} = \operatorname{diag}\{\sigma_1, \sigma_2, \cdots, \sigma_l\}$  is a diagonal matrix consisting singular values. The values of  $\sigma_k$  are ordered in decreasing order as  $\sigma_1 \geq \sigma_2 \geq \cdots \sigma_l \geq 0$ . The matrix  $U = (\varphi_1, \varphi_2, \cdots, \varphi_m)$  is an  $m \times m$  orthogonal matrix that consists of the eigenvectors of the  $AA^T$ , whereas the matrix  $V = (\phi_1, \phi_2, \cdots, \phi_L)$  is an  $L \times L$  orthogonal matrix consisting of the orthogonal eigenvectors of  $A^TA$ . The matrix O is a zero matrix.

In an SVD formulation, the matrices U and V are unitary. This means that  $U^TU=I,\ UU^T=I$  and  $V^TV=I,\ VV^T=I.$ 

$$A = U\Sigma V^{T} = U \begin{bmatrix} \Sigma_{l \times l} \\ O_{l \times (m-l)} \end{bmatrix} V^{T} = \hat{U}\Sigma_{l \times l}V^{T}$$
(2.7)

[47] describe the formulation of the *economy* SVD which is the right-hand side of Equation 2.7. This is the method of representing the matrix A with a smaller basis set  $\hat{U}$ . The matrix A is often too large to compute the SVD from directly. Therefore, the autocovariance matrix is calculated first as in Equation 2.8.

$$C = A^{T} A$$

$$= \left( U \begin{bmatrix} \Sigma_{l \times l} \\ O_{(m-l) \times l} \end{bmatrix} V^{T} \right)^{T} \left( U \begin{bmatrix} \Sigma_{l \times l} \\ O_{(m-l) \times l} \end{bmatrix} V^{T} \right) = \left( \hat{U} \Sigma_{l \times l} V^{T} \right)^{T} \left( \hat{U} \Sigma_{l \times l} V^{T} \right)$$

$$= V S V^{T}, \qquad (2.8)$$

Note that  $C \in \mathbb{R}^{(L \times L)}$  and  $S = \sum_{l \times l}^T \hat{U}^T \hat{U} \sum_{l \times l} = \sum_{l \times l}^2$ . Taking the SVD of the matrix C is much cheaper to compute as the matrix is much smaller than the A matrix when  $L \ll m$  [45].

The matrix  $\hat{U}$  may be computed when  $V^T$  is known as in Equation 2.9. This is practical as  $\Sigma_{l \times l}$  is square and invertible when  $\sigma_l > 0$ .

$$\hat{U} = AV\Sigma_{l \times l} \tag{2.9}$$

The SVD formulation of Equation 2.7 has a physical interpretation. The matrix U represents the modes inside the data. Although POD modes are mathematically optimal in terms of energy capture and orthogonal structure, their physical interpretation must be treated with care. The modes reflect dominant spatial variance but do not necessarily correspond to physically separable phenomena unless validated against flow features or symmetries. Typically, lower-order modes often represent large-scale, energy-dominant structures, while higher-order modes capture finer details or turbulent fluctuations.

The matrix  $\Sigma$  represents the variance or the energy of each of the modes. The singular values inside the diagonal of  $\Sigma$  represent the energy contribution of each of the modes. The singular values are sorted by size inside the matrix. This means that the first few singular in  $\Sigma$  correspond to the dominant modes. A low-rank reconstruction of the flow field involves taking only the most energy containing modes to reconstruct the data.

 $V^T$  represents the time development of the modes. The rows of  $V^T$  contain the time series coefficients of each of the modes. For each given mode there is a corresponding row of  $V^T$  that contains the unique time signal of that mode.

It is often seen that only the first few modes contain most of the energy. The modal eigenvectors in U can be reconstructed and plotted to display the spatial modes. This is possible because each element of the  $m \times 1$  vector  $\varphi_k$  in U corresponds to a point in the 2D or 3D grid of m points.

Low-rank approximations are also possible for single images. Rather than flattening the image, the pixel data is retained in its original two-dimensional form. For example, an image with a resolution of  $100 \times 200$  is represented as a data matrix of the same shape, where each entry corresponds to a pixel intensity. By applying singular value decomposition (SVD) to this matrix and retaining only the dominant singular values and corresponding singular vectors, one can perform a low-rank reconstruction of the image. This process effectively compresses the original image by capturing its most significant features, as illustrated in figure 2.11.

The eigenvectors in U are orthogonal,  $\varphi_i \cdot \varphi_k = \delta_{jk}$ . Let q(x,t) be the flow field. Then the flow field may be approximated with the k most energetic modes as in equation (2.10). Here  $a_j(t)$  are the temporal coefficients of the modes.

$$q(x,t) \approx \sum_{j=1}^{k} a_j(t)\varphi_j(x)$$
 (2.10)

This is called a low-rank reconstruction of the flow field. It means that the majority of the variance of the flow field is captured by just the first k modes. Often the mean is subtracted. [48] give their approximation as in equation (2.11). In this equation  $\bar{u}(x)$  is the temporal mean of the flow field, u'(x,t) the fluctuations around the mean and the values of  $a_j(t)$  describe the time evolution of the modes.  $a_j(t)$  represents the rows of  $\Sigma V^T$ . The value of  $a_j(t) = \varphi_j^T q(x,t)$ .

$$u(x,t) = \bar{u}(x) + u'(x,t) = \bar{u}(x) + \sum_{i=j}^{N} a_j(t)\varphi_j(x)$$
(2.11)

The subtraction of the mean is often not a neutral operation. Often the first mode of a signal corresponds to its mean. Furthermore, the POD modes must be orthogonal to this mean mode. In complex and transitional flows, the mean might not correspond to a natural mode of the system. In these cases, subtracting the mean can alter the energy distribution among the modes [49].

Another operation that is often applied in POD or other forms of ROM is the inclusion of a weighting scheme. This is especially the case for non-Cartesian coordinate systems. The inherent geometry of such coordinate systems may result in non-uniform contributions from different spatial regions, which can bias the energy content captured by the POD modes. This weighting is introduced by formulating a different covariance matrix as in equation (2.12). Here  $C_W$  is the weighted covariance matrix and A the data matrix.

$$C_W = A^T W A (2.12)$$

The coefficients within the W matrix typically represent the area or volume associated with each spatial discretisation point [50]. Consequently, points corresponding to larger regions contribute more significantly, ensuring that each spatial point is fairly weighted in the decomposition.

[45] describe necessary choices that need to be made concerning data that is used to apply POD to flowfields. Mainly the random variables,  $\mathbf{q}$ , independent variables x, the domain  $\Omega$ , and the means to obtain sufficient realisations of the process. Numerical simulation data may be too voluminous for a three-dimensional flow field. This can make the calculation impractical.

#### 2.2.2. Spectral Proper Orthogonal Decomposition

Spectral Proper Orthogonal Decomposition (SPOD) is a subset of POD. [45] describe that in SPOD, unlike standard POD, described in the previous section, the modes vary in both space and time. Standard POD, by its very construction, is independent of the order of different instances in time. The time-dependency of the flow has no impact on the definition of the POD modes [45].

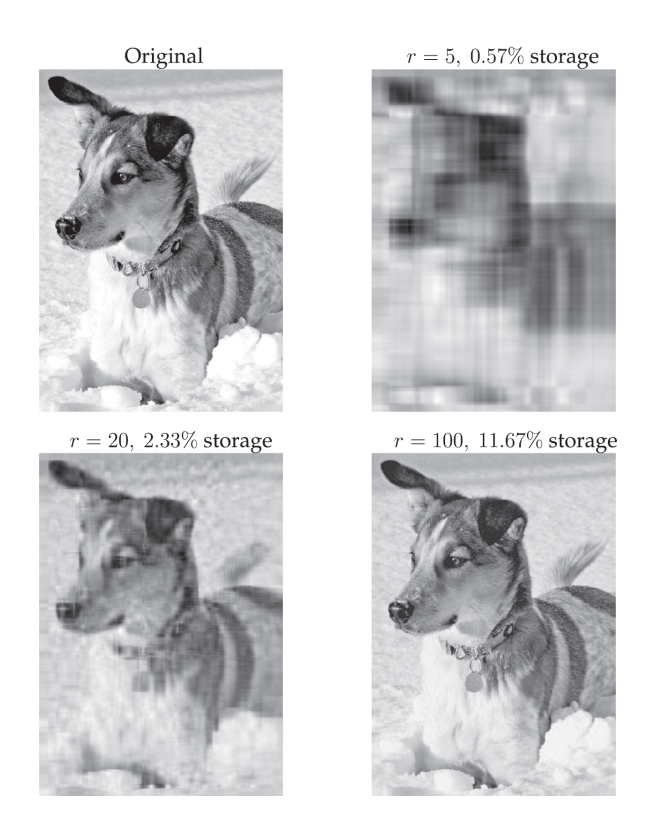


Figure 2.11: Image compression of a dog using truncated SVD at various ranks r. Reproduced from [47] p.10.

The method for calculating SPOD modes differs from standard POD. The procedure for computing SPOD here is transcribed from [40].

Similar to standard POD a snapshot matrix is generated for the mapped points into a column vector. One snapshot vector is generated for each time step. The snapshot matrix Q is then given according to equation (2.13). Where each vector  $q_k$  corresponds to the snapshot of the flow at a time step  $t_k$ .

$$Q = [q_1, q_2, \cdots, q_M] \tag{2.13}$$

The unique step in SPOD is to partition the snapshot data matrix into smaller, possibly overlapping blocks and then take each block's discrete Fourier transform (DFT).

Each block may be written as in equation (5.16).

$$Q^{n} = [q_{1}^{(n)}, q_{2}^{(n)}, \cdots, q_{N_{F}}^{(n)}]$$
(2.14)

In equation (5.16) the k-th entry in the n-th block is  $q_k^{(n)} = q_{k+(n-1)(N_f-N_0)}$ , where  $N_f$  is the number of snapshots in each block,  $N_0$  is the number of snapshots in each block,  $N_0$  amount of snapshots by which blocks overlap, note that this may be 0, and  $N_b$  is the number of blocks. The procedure of splitting the data matrix into blocks like this is Welch's method [51]. This is done because the spectral estimates obtained this way do not converge as the number of snapshots increases. The number of blocks determines the amount of resolved frequencies. Less blocks mean more frequencies can be resolved, but the uncertainty at each frequency increases [52]. A schematic of Welch's method may be seen in figure 2.12.

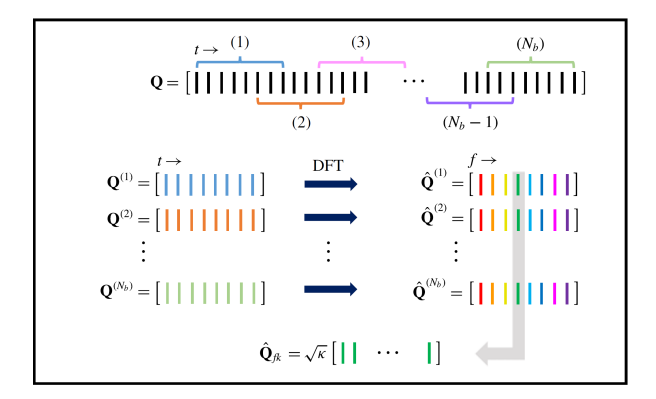


Figure 2.12: Schematic of Welch's method with blocks for estimating SPOD modes. Reproduced from [40] p. 831.

The DFT of each block is taken and the resulting matrix may be written as in equation (2.15).

$$\hat{Q}^n = [\hat{q}_1^{(n)}, \hat{q}_2^{(n)}, \cdots, \hat{q}_{N_F}^{(n)}]$$
(2.15)

In equation (2.15) each vector  $\hat{q}_k^{(n)}$  is defined as in equation (2.16). Here the  $w_j$  is term added. This is a scalar weight that can be added to reduce spectral leakage. This is because the data block may be non-periodic and the DFT algorithm assumes implicitly that the time series repeats itself [53]. [53] recommend a Kaiser-Bessel window as a first choice, but the choice depends on a compromise between the width of the resulting peak in the frequency domain and the spectral leakage into other frequencies. Note that the factor  $1/\sqrt{N_f}$  is added to make the transform unitary when  $w_j = 1$  for all j.

$$\hat{q}_k^{(n)} = \frac{1}{\sqrt{N_f}} \sum_{j=1}^{N_f} w_j q_j^{(n)} e^{-i2\pi(k-1)\frac{j-1}{N_f}}$$
(2.16)

[40] provide an algorithm for calculating the modes from the matrix  $\hat{Q}^n$ . The algorithm is not transcribed here for the sake of brevity. The main takeaway is that to find the modes in the data an eigenvalue problem must be solved for each frequency or frequency of interest. A similar matrix as the  $\hat{U}$  matrix from section 2.2.1 is found called  $\Psi_{f_k}$ . This is the eigenvector matrix that corresponds to the frequency  $f_k$ . The columns of this matrix are the eigenvectors that correspond to the modes inside the data. It should be noted that at most  $N_b$  non-zero eigenvalues can be obtained. Since an eigenvalue problem must be solved at many frequencies the SPOD algorithm is more expensive to run than traditional POD. Implementations of the algorithm mention the high memory usage [54].

[40] demonstrate mathematically that each POD mode can be made up of many SPOD modes. This highlights that POD modes represent flow phenomena at many different time scales while SPOD modes decouple the time scales from the phenomena.

#### 2.2.3. Dynamical Mode Decomposition

Dynamical mode decomposition (DMD) is based on POD. It is another method to dimensionally reduce a complex system. In contrast to POD, DMD provides decomposition that results in a set of modes and also a model of these modes evolve in time [47].

DMD is a best-fit linear algorithm that advances high-dimensional measurements forward in time [55]. DMD works well for experimental and measurement data similar to the applications for POD.

There are several DMD algorithms, this report focuses on the exact DMD algorithm by [55]. DMD consists of generating two snapshot matrices. Similar to POD these are long tall matrices where each column consists of a snapshot of the data of a particular system or random process in time. The snapshot pair matrices are usually denoted as X and X'. The data matrix X' is the data matrix X with a shift in one column such that  $t'_k = t_k + \Delta t$ . The respective matrices are shown in equation (2.17) and equation (2.18).

$$X = \begin{bmatrix} | & | & | & | \\ X(t_1) & X(t_2) & \cdots & X(t_m) \\ | & | & | & | \end{bmatrix}$$
 (2.17)

$$X' = \begin{bmatrix} | & | & | & | \\ X(t'_1) & X(t'_2) & \cdots & X(t'_m) \\ | & | & | & | \end{bmatrix}$$
 (2.18)

The DMD algorithm seeks to find the linear operator B that relates the matrices to each other as shown in equation (2.19).

$$X' \approx BX \tag{2.19}$$

The dynamical system resulting from this is then given according to equation (2.20).

$$x_{k+1} \approx Bx_k \tag{2.20}$$

Mathematically, B is defined as in equation (2.21). Here  $||\cdot||_F$  is the Frobenius norm and  $X^{\dagger}$  is the pseudo inverse of X.

$$B = \underset{x}{\operatorname{argmin}} ||X' - BX||_F = X'X^{\dagger}$$
(2.21)

Computing B is impractical as it is very expensive to compute the inverse. [47] describe the DMD algorithm to find the DMD modes through a singular values decomposition of X. This algorithm is not shown in this report for brevity.

DMD enables the reconstruction of system dynamics using data-driven spectral decomposition. The DMD modes  $\phi_j$  are the eigenvectors of B, and the system's time evolution can be described by the formulation in equation (2.22). Here  $\lambda_j$  are the DMD eigenvalues of the matrix B and  $\Phi$  the matrix of DMD modes.

$$x_k = \sum_{j=1}^r \phi_j \lambda_j^{k-1} b_j = \mathbf{\Phi} \mathbf{\Lambda}^{k-1} \mathbf{b}$$
 (2.22)

The vector  $\boldsymbol{b}$ , which represents the initial conditions of the system. It is computed as in equation (2.23)

$$\boldsymbol{b} = \boldsymbol{\Phi}^{\dagger} \boldsymbol{x}_1 \tag{2.23}$$

$$x(t) = \sum_{j=1}^{r} \phi_j e^{\omega_j t} b_j \tag{2.24}$$

One noteworthy property of DMD is that it is formally equivalent to discrete Fourier transform (DFT) for zero-mean data that is uniformly sampled in time [40]. The equivalence can be seen from equation (2.24). Here the data is expressed as a sum of complex exponentials and this is precisely what the DFT does. Each spatial mode  $\phi_j$  fluctuates at a single frequency  $\omega_j$  with a magnitude of  $b_j$ .

2.3. Synthesis 16

#### 2.3. Synthesis

Considering the aim outlined in the introduction—developing a computationally efficient wake model for wind turbine tower wakes at high Reynolds numbers—Proper Orthogonal Decomposition (POD) emerges as the most suitable choice among the reviewed Reduced Order Models (ROMs). At these high Reynolds numbers, the von Kármán vortex shedding frequency broadens considerably, resulting in a wide spectral peak. This broader frequency spectrum significantly reduces the applicability of Dynamical Mode Decomposition (DMD), which inherently relies on the identification and isolation of clear, distinct frequencies. Consequently, DMD is unsuitable in these contexts, given its limited capacity to handle flow structures characterised by frequency variability.

Spectral Proper Orthogonal Decomposition (SPOD), while beneficial for the clear interpretation of time-frequency-specific modes, introduces substantial computational challenges, particularly in memory usage. Given the project's emphasis on reducing computational cost while still capturing essential flow characteristics, these practical limitations notably hinder SPOD's application. Thus, POD remains the most effective ROM approach, offering a balance between capturing the dominant flow features and maintaining manageable computational demands.

A rigorously detailed wake model would, in theory, need to account for every mechanism identified in the literature review-including variations in Reynolds number, surface roughness, spanwise lock-in phenomena, and the influence of cylinder motion on the wake structures. The present study will restrict its scope to a height-dependent correlation model, which is intended to capture the primary spanwise coherence of the tower wake. Limitations arising from the exclusion of other mechanisms are discussed later in the thesis.

# Methodology

In this chapter, a methodology is presented for building a stochastic reduced-order model (SROM) of a tower wake flow. First, data acquisition of an Stress-Blended Eddy Simulation SBES simulation is described, capturing the turbulent flow data around the tower. Next, the Proper Orthogonal Decomposition (POD) is applied to extract the dominant wake modes. The selected modes are then combined with cross-spectral methods to generate stochastic time-series realisations, ensuring realistic phase relationships and spectral characteristics. Finally, a method is proposed for extending the two-dimensional representation into a fully three-dimensional flow field by introducing vertical coherence between multiple horizontal planes. Vertical correlation length and its dependence on turbulence intensity or structural vibration amplitude are discussed.

#### 3.1. SBES simulation and data acquisition

This study uses data that is acquired through a CFD simulation. This section explains the setup of this CFD simulation that is used for study. It explains the setup of the quasi-2D and 3D flow cases. Furthermore it explains the data that is stored from the simulations.

#### 3.1.1. Quasi-2D Mesh and Simulations

The CFD setup employs a Scale-Adaptive Simulation based on the Stress-Blended Eddy Simulation (SBES) approach to capture the turbulent flow around a tower structure. SBES utilises a hybrid formulation that combines the Reynolds-Averaged Navier–Stokes (RANS) method, specifically the k- $\omega$  SST model, with Large Eddy Simulation (LES). In this configuration the near-wall region is treated with the RANS model to avoid the high grid resolution requirements of classical wall-resolved LES.

The computational mesh is designed with distinct zones of refinement. On the 2D surface, the mesh consists of 600 points in the radial direction and features a cell size of 0.1 m in the spanwise direction. This surface is illustrated in figure 3.1. In the refined wake region, a first cell height of  $1 \times 10^{-5}$  m is specified, with a growth rate of 1.07 and a maximum cell height of 0.5 m, covering a region with a diameter of 70 m. The outer domain is constructed with a growth rate of 1.5, an overall diameter of 305 m, and a maximum cell size of 10 m, ensuring that the far-field flow is adequately captured. These meshes can be seen in figure 3.2 and figure 3.3 respectively.

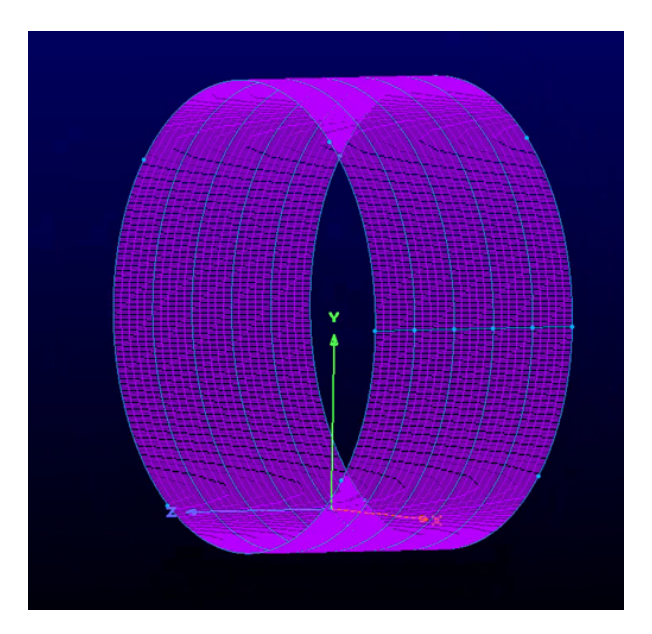


Figure 3.1: 2D surface cylinder surface

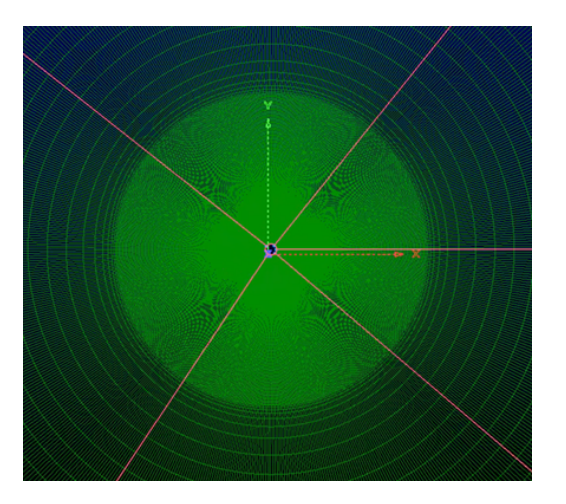


Figure 3.2: Refined wake mesh

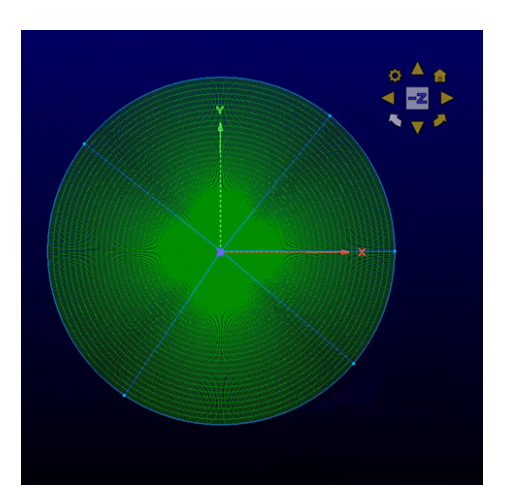


Figure 3.3: Outer domain mesh

The geometry of the simulation is based on an extruded cylinder representing the tower, with a diameter of 5 m. The height of the domain for the quasi-2D flow is half a diameter or 2.5 m. This simulation is referred to as a quasi-2D case because the height of the domain is significantly smaller than its other dimensions, meaning that variations in the vertical direction are minimal and the flow behaves almost two-dimensionally. Inflow conditions are defined by a uniform flow at three different wind speed of 11, 15 and 19 ms<sup>-1</sup>, with no shear imposed. The turbulence is modelled exclusively using the SBES approach implemented in CFX, and a fully turbulent flow is assumed throughout, given the transcritical nature of the regime. At the top and bottom boundaries of the cylinder, periodic conditions without penetration are applied, while a wall boundary condition is prescribed on the cylinder surface. The no-penetration boundary constraint sets the w-component of the velocity to zero at the top and bottom boundaries. All remaining boundaries are assigned an inlet condition.

The velocity components u, v, w are acquired in a uniform mesh with a time step of 0.05 s. The mesh is a 2D slice in the middle of the cylinder height. The mesh that is used to save the points is illustrated in figure 3.4. The mesh consists of 200 points in the x-direction and 80 in the y-direction. This means that the resolution of each of the mesh points is 0.25 m by 0.25 m. Data is saved for 2000 time steps. This is equivalent to 100 seconds of simulated time.

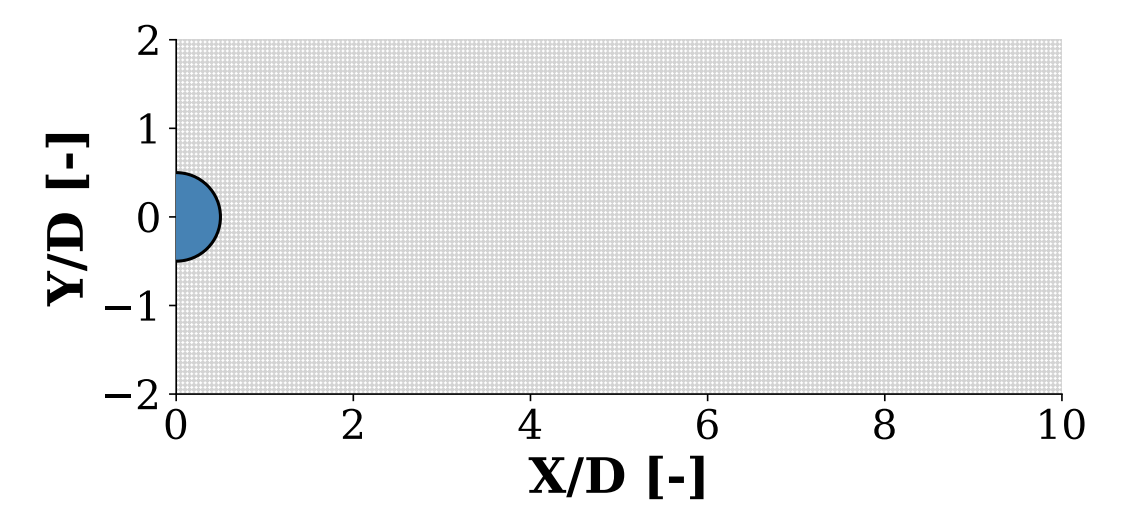


Figure 3.4: Quasi-2D simulation mesh points used for data acquisition

#### 3.1.2. Three-dimensional (3-D) Mesh and Simulations

To assess the influence of spanwise development, the quasi-2-D grid is extruded to a total height of four diameters  $(Z = 20\,\mathrm{m})$ . The resulting mesh therefore contains eight times as many control volumes as the quasi-2D case.

At a wind speed of 19 ms<sup>-1</sup> three 3-D simulations are performed:

- 1. **Fixed cylinder** the cylinder remains stationary.
- 2. Oscillating cylinder, low amplitude harmonic motion with amplitude  $A = 0.25 \,\mathrm{m}$  at a frequency  $f = 1 \,\mathrm{Hz}$ .
- 3. Oscillating cylinder, high amplitude identical frequency,  $A = 0.50 \,\mathrm{m}$ .

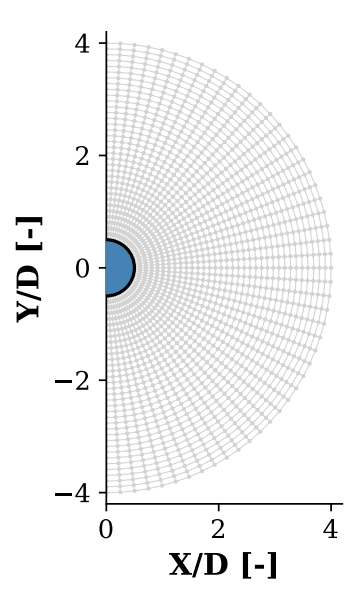


Figure 3.5: 3D simulation mesh points used for data acquisition

For the wake analysis, the velocity components (u, v, w) are stored on a polar grid as shown in figure 3.5. The grid spans to the right hand side of cylinder. The points are spaced from the surface of the cylinder to a radial distance of four diameters, using

- $N_r = 35$  radial nodes, uniformly spaced at  $\Delta r = 0.5$  m;
- $N_{\theta} = 50$  angular nodes, covering  $\theta = (-\frac{\pi}{2}, \frac{\pi}{2})$ .

Five horizontal slices are extracted at the non-dimensional heights z/D = 0.0, 0.1, 0.2, 0.8, and 1.6.

Temporal sampling differs between cases:

Case	Sampling rate	Time steps	Physical time
Fixed cylinder	$100\mathrm{Hz}$	9 000	90 s
Oscillating (0.25 m)	$100\mathrm{Hz}$	3000	$30\mathrm{s}$
Oscillating $(0.50 \text{ m})$	$100\mathrm{Hz}$	3000	$30\mathrm{s}$

All other boundary-condition settings match those described for the quasi-2-D simulation, therefore differences in the results arise solely from three-dimensional flow development.

#### 3.2. Quasi-2D Stochastic Reduced Order Modelling

This section describes the quasi-2D stochastic reduced order modelling (SROM) approach for tower wake flows. It begins with an explanation of the application of Proper Orthogonal Decomposition (POD) to isolate the dominant modes from the fluctuating velocity field. The method then uses spectral techniques to generate stochastic time series from these modal time series. In this process, the modal signals are transformed into the frequency domain, and spectral colouring is applied to impose the correct cross-spectral properties, ensuring that the reconstructed time series retain the essential dynamic characteristics of the flow.

Furthermore, the section outlines how the two-dimensional flow fields are extended to a full three-dimensional representation. This is achieved by introducing vertical correlations between multiple horizontal planes. The vertical correlation is modelled using cross-spectral block matrices and exponential decay functions.

#### 3.2.1. Proper Orthogonal Decomposition

This section focuses on the implementation of proper orthogonal decomposition (POD) for identifying the dominant modes in the flow. The method decomposes the flow into modes characterised by spatial variability, with the dominant modes representing the most energetic spatial structures.

The velocity field is expressed as the sum of the mean flow,  $\bar{V}$ , and the fluctuating flow, V'.

$$V(x, y, z, t) = \bar{V}(x, y, z) + V'(x, y, z, t)$$
(3.1)

POD is applied on the three fluctuating velocity components of V(x, y, z, t) namely u', v' and w'. The data matrix A as shown in equation (3.2) is constructed after the domain is chosen for the analysis.

$$A = \begin{bmatrix} u'^{1} & u'^{2} & \cdots & u'^{N} \\ u'^{1}_{2} & u'^{2}_{2} & \cdots & u'^{N}_{2} \\ \vdots & \vdots & \ddots & \vdots \\ u'^{1}_{M} & u'^{2}_{M} & \cdots & u'^{N}_{M} \\ v'^{1}_{1} & v'^{2}_{1} & \cdots & v'^{N}_{2} \\ \vdots & \vdots & \ddots & \vdots \\ v'^{1}_{M} & v'^{2}_{M} & \cdots & v'^{N}_{M} \\ v'^{1}_{1} & v'^{2}_{1} & \cdots & v'^{N}_{M} \\ v'^{1}_{1} & v'^{2}_{1} & \cdots & v'^{N}_{M} \\ w'^{1}_{1} & w'^{2}_{1} & \cdots & w'^{N}_{M} \\ w'^{1}_{1} & w'^{2}_{1} & \cdots & w'^{N}_{M} \\ w'^{1}_{2} & w'^{2}_{2} & \cdots & w'^{N}_{M} \\ \vdots & \vdots & \ddots & \vdots \\ w'^{M}_{M} & w'^{M}_{M} & \cdots & w'^{N}_{M} \end{bmatrix}$$

$$(3.2)$$

A data matrix A of the flow is constructed from the fluctuating velocity components V'. This means that the mean is subtracted from the flow. The points chosen lie in the domain described in ??. A singular value decomposition (SVD) is taken on the fluctuating velocity components as in equation (2.7). The resulting matrices U,  $\Sigma$  and  $V^{\mathsf{T}}$  are used further in the model.

Due to memory limitations, it is often advantageous to reduce the computational cost of the model. Consequently, the reconstructed flow is usually defined to contain 95% of the kinetic energy of the original flow. The energy content is computed from the singular values in the  $\Sigma$  matrix. The mode cut-off, k, is determined according to equation (3.3), where  $\Sigma_{ii}$  denotes the i-th singular value of  $\Sigma$ .

$$\frac{\sum_{i=1}^{k} \Sigma_{ii}}{\sum_{i=1}^{n} \Sigma_{ii}} \approx 0.95 \tag{3.3}$$

The dominant modes in the flow contain the majority of the energy. This cut-off significantly reduces the number of modes used in the flow reconstruction. Higher-order modes represent higher fluctuations in the data and these are excluded.

As an alternative cut-off strategy, this work will also present the optimal truncation method, specifically the optimal singular value hard threshold (optimal SVHT) [56]. Rather than prescribing a fixed energy percentage, optimal SVHT determines a data-dependent threshold derived from random-matrix theory. Modes whose singular values lie below this threshold are, with high probability, dominated by numerical noise and contribute negligibly to the physical signal. Hence, they are excluded, yielding a more compact reduced-order model.

#### 3.2.2. Stochastic Time Series Generation

In this section, the method for generating stochastic time series from modal time series is described. The method is based on classic Gaussian process spectral theory [57, 58]. These methods are applied to generate stochastic time series. This method has previously been implemented to generate stochastic time series for wind turbine wakes [43, 59].

The method involves the cross-spectral density (CSD) representation, which describes the frequency-dependent relationships between different time series components. For each frequency bin f, the CSD is given by a Hermitian matrix S(f), which captures the spectral energy distribution and coherence structure of the data. The matrix S(f) consists of power spectral densities along its diagonal and cross-power spectral densities in its off-diagonal elements. These cross-power terms encode phase relationships and statistical dependencies between different components of the time series at a given frequency.

Since the spectral properties vary across frequencies, the full representation of the CSD spans multiple frequency bins, effectively forming a three-dimensional array or a frequency-dependent set of matrices. This structure allows for frequency-specific processing, where the CSD is decomposed at each frequency independently. The decomposition follows according to equation (3.4).

$$S(f) = H(f)H^{H}(f) \tag{3.4}$$

In equation (3.4) H(f) is a matrix whose columns represent correlated spectral modes, and  $H^H(f)$  is its Hermitian transpose (complex conjugate transpose). Several decomposition methods can be used to compute H(f), including Cholesky decomposition and Jacobi methods, which are well suited for positive definite matrices. Previous implementations of this method have used the LDL decomposition [59] as it is more numerically stable due to rounding errors. This report utilizes the Cholesky decomposition.

To generate a stochastic time series, the method begins with the matrix  $V^{\mathsf{T}}$ , whose rows represent the different modal time series sorted by descending eigenvalues. The Fourier transform is applied along the time axis for each row, yielding a transformed matrix  $\widehat{V}^{\mathsf{T}}$ . The top m dominant modes are selected, and their Fourier-transformed components are used to construct the CSD matrix across different frequencies. Since the CSD matrix is computed at each frequency separately, the full spectral representation consists of a collection of such matrices across all frequency bins. The CSD matrix is constructed from a given set of Fourier-transformed modal time series  $X_i(f)$  and  $X_j(f)$ . The elements of the CSD matrix are defined in equation (3.5).

$$S_{ij}(f) = X_i(f)X_i^*(f)$$
(3.5)

In equation (3.5)  $X_j^*(f)$  is the complex conjugate of  $X_j(f)$ . The diagonal elements,  $S_{ii}(f)$ , represent the power spectral densities of each individual component, while the off-diagonal elements encode the phase relationships and coherence between different components of the system.

At each frequency, the CSD matrix is decomposed using the Cholesky decomposition. A realisation of white noise, N(f), is generated by sampling independent, uniformly distributed phases,  $\Phi$ , while preserving Gaussian amplitude distributions. The H(f) matrix acts as a spectral shaping operator, effectively imposing the correct cross-spectral properties onto the stochastic process. This ensures that the generated time series maintains the desired correlation structure. The first m dominant modes are then 'coloured' by applying a spectral transformation derived from the decomposed cross-spectral density (CSD) matrix. Note that these m dominant modes form only a subset of the k modes retained according to either the 95% energy criterion or the optimal SVHT cut-off, as discussed in section 3.2.1. Here, k denotes the total number of retained modes, while m (with m < k) represents the most energetically significant modes selected for spectral colouring.

For modes beyond the dominant modes m, their phase information is randomized while maintaining their amplitude spectrum. This step ensures that the spectral energy distribution remains consistent while removing structured phase relationships for higher-order modes. The final realisation of the modal time series,  $\tilde{\phi}(t)$ , is obtained by applying the inverse fast Fourier transform (IFFT) as in equation (3.6).

$$\tilde{\phi}(t) = \mathcal{F}^{-1} \left\{ \mathbf{H}(f) \mathbf{N}(f) \right\} = \mathcal{F}^{-1} \left\{ \mathbf{H}(f) e^{i\Phi} \right\}$$
(3.6)

This transformed time series  $\tilde{\phi}(t)$  represents the new modal time series with the desired statistical and spectral properties.

The remaining temporal modes without the spectral colouring, but with randomized phases are combined with temporal coloured modes to obtain a new  $V_{\text{new},k}^{\mathsf{T}}$  matrix as in equation (3.7).

$$V_{\mathrm{new},k}^{\mathsf{T}} = \text{Normalize}\Big(\mathcal{F}^{-1}\left\{\widehat{V}_m(f)\right\} \oplus \mathcal{F}^{-1}\left\{\widehat{V}_{k-m}(f)\right\}\Big). \tag{3.7}$$

In equation (3.7)  $\widehat{V}_m(f)$  is the matrix containing the dominant spectrally, coloured, temporal modes up to m and  $\widehat{V}_{k-m}(f)$  the remaining Fourier transformed temporal modes up to the cut-off k with randomized phases. The operator  $\oplus$  denotes the vertical concatenation of the dominant m and the remaining k-m modal components. The temporal modes obtained through POD are by construction orthonormal. The spectral method breaks the orthogonality and the normalization is broken slightly. In order to maintain the same energy in the reconstructed flow the time series are again normalized to have a norm of 1.

Reconstruction of the generated flow is then done according to equation (3.8). Here  $\bar{V}(x,y,z)$  the mean of the original flow,  $\Sigma_{ii}$  the singular values of the  $\Sigma$  matrix from the SVD and  $\tilde{\phi}_{i}(t)$  the time series.

$$V(x, y, z, t) \approx \bar{V}(x, y, z) + \sum_{i=1}^{k} \Sigma_{ii} \tilde{\phi}_{i}(t)$$
 (3.8)

In equation (3.9) the formulation of the reconstruction is again given, but in matrix notation. The subscripts k indicate the mode cut-off. The matrices have the shapes  $U_k \in \mathbb{R}^{3M \times k}$   $\Sigma_k \in \mathbb{R}^{k \times k}$  and  $V_{\text{new},k}^\mathsf{T} \in \mathbb{R}^{k \times T}$ . Here M is the total amount of points used in the analysis and T the total amount of time steps.

$$A_{\text{reconstruction}} = U_k \Sigma_k V_{\text{new},k}^{\mathsf{T}} \in \mathbb{R}^{3M \times T}$$
(3.9)

The reconstruction matrix  $A_{\text{reconstruction}}$  contains in each column the velocity components at each point. The columns of the reconstruction matrix describe the reconstructed flow time evolution at each point.

#### 3.3. Extending 2D Flow Fields to 3D Using Correlated Fields

In this section, the methodology for extending a set of 2D stochastic flow fields, each defined on a horizontal plane at different heights, into a fully 3D representation is described. Vertical correlations between these layers are introduced to ensure that velocity components u, v, and w remain physically consistent across different heights while maintaining realistic spatial coherence and phase relationships.

#### 3.3.1. Multi-Layer Flow Representation

For a multi-layer flow representation flows are desired at multiple height locations of the tower. Each height has a local wind speed  $U_n$ , diameter  $D_n$ , and spatial coordinate  $z_n$ . A previous implementation of the SROM model has implemented the interpolation of the cross spectral densities (CSD) of modes [59]. It is proposed that this may be possible for the modes of tower wakes. The premise relies on the spatial patterns remaining similar. The method is implemented by applying a frequency shift to the modes of the  $V_{\text{new},k}^{\mathsf{T}}$  matrix.

#### 3.3.1.1. Frequency Shift

Let there be N flows, each described by a modal time series as shown in equation (3.10). These time series are obtained from the POD of the simulation data and are initially identical.

$$V^{(n)}(t) \in \mathbb{R}^{3M \times T}, \quad n = 1, \dots, N,$$
 (3.10)

The shedding frequency  $f_n$  for a flow n is given by equation (3.11). Here St is the Strouhal number.

$$f_n = \operatorname{St} \cdot \frac{U_n}{D_n} \tag{3.11}$$

A reference flow (with  $U_{\text{ref}}$  and  $D_{\text{ref}}$ ) is chosen. This is the reference wind speed of the simulated flow case. A scaling factor for flow n as is defined as in equation (3.12).

$$\beta_n = \frac{U_{\text{ref}}/D_{\text{ref}}}{U_n/D_n} \tag{3.12}$$

To obtain a lower effective frequency for a slower flow the time axis is stretched by this factor  $\beta_n$ . Thus, if a spectral peak originally occurs at frequency  $f_0$ , after time stretching it appears at  $f_{\text{new}}$  as in equation (3.13).

$$f_{\text{new}} = \frac{f_0}{\beta_n} = f_0 \cdot \frac{U_n/D_n}{U_{\text{ref}}/D_{\text{ref}}}$$
(3.13)

For a given modal time series x(t) with Fourier transform X(f), the time-stretched signal is defined as in equation (3.14).

$$x_{\beta_n}(t) = x \left(\frac{t}{\beta_n}\right),\tag{3.14}$$

The Fourier transform of this signal is then given according to equation (3.15).

$$X_{\beta_n}(f) = \beta_n X(\beta_n f) \tag{3.15}$$

In this manner a spectral component at  $f_0$  is shifted as in equation (3.16).

$$f_{\text{new}} = \frac{f_0}{\beta_n} \tag{3.16}$$

#### 3.3.1.2. Block Cross-Spectral Matrix Construction

A cross-spectral block matrix is constructed for each flow. This matrix captures the correlations between modes inside each individual flow at each height and the correlations between flows at different heights.

For each flow n, the FFT of the dominant m modes is taken. This yields for a flow n the Fourier transformed matrix  $\widehat{V}_n(f)$  as in equation (3.17).

$$\widehat{V}_n(f) \in \mathbb{C}^m. \tag{3.17}$$

Considering N flows, where each flow n is represented by its vector of Fourier coefficients for the m dominant modes the vector of coefficients is given as in equation (3.18) at each frequency.

$$\mathbf{X}^{(n)}(f) = \begin{bmatrix} X_1^{(n)}(f) \\ X_2^{(n)}(f) \\ \vdots \\ X_m^{(n)}(f) \end{bmatrix} \in \mathbb{C}^m$$
(3.18)

For a single flow, let  $\mathbf{X}^{(n)}(f) \in \mathbb{C}^m$  denote the vector of Fourier coefficients corresponding to the m dominant modes of flow n at frequency f. The auto-spectral density matrix of flow n is then defined as in equation (3.19)

$$\mathbf{S}_{nn}(f) = \mathbf{X}^{(n)}(f)\mathbf{X}^{(n)*}(f) \tag{3.19}$$

Here the (i, j)th entry of  $\mathbf{S}_{nn}(f)$  is given by equation (3.20).

$$S_{ij}^{(n)}(f) = X_i^{(n)}(f)X_j^{(n)*}(f), \quad i, j = 1, \dots, m$$
 (3.20)

In the formulation of equation (3.20), the diagonal elements  $S_{ii}^{(n)}(f)$  represent the power spectral density (PSD) of the *i*th mode, while the off-diagonal elements capture the cross-spectral densities which is consistent with equation (3.5). The formulation of this matrix expands to the matrix shown in equation (3.21).

$$\mathbf{S}_{nn}(f) = \begin{pmatrix} X_1^{(n)}(f)X_1^{(n)*}(f) & X_1^{(n)}(f)X_2^{(n)*}(f) & \cdots & X_1^{(n)}(f)X_m^{(n)*}(f) \\ X_2^{(n)}(f)X_1^{(n)*}(f) & X_2^{(n)}(f)X_2^{(n)*}(f) & \cdots & X_2^{(n)}(f)X_m^{(n)*}(f) \\ \vdots & \vdots & \ddots & \vdots \\ X_m^{(n)}(f)X_1^{(n)*}(f) & X_m^{(n)}(f)X_2^{(n)*}(f) & \cdots & X_m^{(n)}(f)X_m^{(n)*}(f) \end{pmatrix}$$
(3.21)

Correlation is also defined between different flows. For two distinct flows i and j (with  $i \neq j$ ), the cross-spectral block is defined as in equation (3.22). Here  $\mathbf{X}^{(i)}$  is the vector of the coefficients of the dominant modes of flow i at frequency f and  $C_{ij}$  is a correlation coefficient between the flows i and j. The value of this coefficient is elaborated on in section 3.3.1.3.

$$\mathbf{S}_{ij}(f) = C_{ij} \left( \mathbf{X}^{(i)}(f) \mathbf{X}^{(j)*}(f) \right)$$
(3.22)

These blocks are assembled into the full block matrix as in equation (3.23). Here S(f) is the CSD representation that relates the frequency-dependent relationships of each of the flows at different heights, diameters and wind speeds.

$$\mathbf{S}(f) = \begin{pmatrix} \mathbf{S}_{11}(f) & \mathbf{S}_{12}(f) & \cdots & \mathbf{S}_{1N}(f) \\ \mathbf{S}_{21}(f) & \mathbf{S}_{22}(f) & \cdots & \mathbf{S}_{2N}(f) \\ \vdots & \vdots & \ddots & \vdots \\ \mathbf{S}_{N1}(f) & \mathbf{S}_{N2}(f) & \cdots & \mathbf{S}_{NN}(f) \end{pmatrix} \in \mathbb{C}^{Nm \times Nm}$$

$$(3.23)$$

Again as in section 3.2.2 the  $\mathbf{S}(f)$  matrix is decomposed as in equation (3.4) into a lower triangular matrix  $\mathbf{H}(f)$ . The lower triangular matrix is multiplied by a realisation of white noise  $\mathbf{N}(f)$ . This is the spectral colouring step. After the spectral colouring step, a coloured Fourier coefficient vector  $\mathbf{Z}(f)$  is obtained as in equation (3.24).

$$\mathbf{Z}(f) = \mathbf{H}(f)\mathbf{N}(f) \in \mathbb{C}^{Nm}$$
(3.24)

This vector is structured as shown in equation (3.25).

$$\mathbf{Z}(f) = \begin{pmatrix} \mathbf{Z}_1(f) \\ \mathbf{Z}_2(f) \\ \vdots \\ \mathbf{Z}_N(f) \end{pmatrix}, \quad \text{with } \mathbf{Z}_n(f) \in \mathbb{C}^m$$
 (3.25)

New modal time series are generated by applying the inverse fast Fourier transform IFFT as in equation (3.6) on each entry  $\mathbf{Z_n}(f)$ . This imposes the correct cross-spectral properties onto the stochastic processes for the dominant m modes. For the remaining modes their frequency spectra are multiplied by a random phase. These remaining modes are therefore assumed to not only be independent in their own height, but also between heights.

The proposed method here applies the shifting of the time series at different layers of the flow based on different flow velocities and diameters. The data of this study are limited to a uniform inflow and a uniform diameter tower. Therefore, the application of this method is not compared with flows with incoming shear or changing tower diameters.

#### 3.3.1.3. Derivation of the Correlation Coefficient

To enforce spatial coherence in the vertical direction, a correlation coefficient is introduced to describe the correlation of the entire 3D velocity field across different heights. The correlation function that is commonly used in turbulence studies is modeled using an exponential decay [60, 61, 62]. Correlation of forcing on cylinders is similarly fit using a exponential decay as in equation (3.26). [17] demonstrated this for drag and lift relationships on a stationary cylinder. In this equation  $C_{mn}$  is the correlation coefficient between velocity fields at heights  $z_m$  and  $z_n$ ,  $L_c$  is the vertical correlation length and  $|z_n - z_m|$  the absolute distance between the two layers.

$$C_{mn} = \exp\left(-\frac{|z_m - z_n|}{L_c}\right) \tag{3.26}$$

Studies on vortex-induced vibrations (VIV) have shown that the effective correlation length in flow forcing models is dependent on turbulence intensity and oscillation amplitude [36]. [18] performed experiments on moving cylinders to measure the correlation length along the cylinder at different oscillation amplitudes and turbulence intensities. Increased turbulence intensity decreases the correlation length while increased oscillation amplitude increases the correlation length. This is illustrated in figure 3.6 and figure 3.7. In the figures 2a is twice the vibration amplitude, D the cylinder diameter and r the distance along the cylinder.

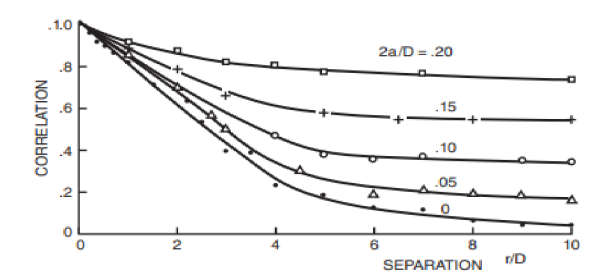


**Figure 3.6:** Smooth flow. Reynolds number:  $2 \times 10^4$ . Reproduced from [63] p. 289

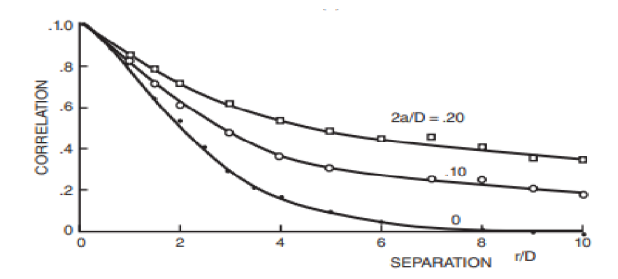


**Figure 3.7:** Flow with 11% turbulence intensity. Reynolds number:  $2 \times 10^4$ . Reproduced from [63] p. 289

A more general model considers the correlation length as a function of turbulence intensity  $I_{\nu}$  and vibration amplitude of the cylinder. As in equation (3.27) where  $I_{\nu}$  is the turbulence intensity and A/D the vibration amplitude. Here  $f(|z_m-z_n|,I_{\nu},A/D)$  represents an empirical fit, typically taking the form of an exponential decay similar to equation (3.26). This model captures how both increased turbulence intensity and vibration amplitude influence the spatial coherence of the forcing. The correlation curves presented in figure 3.6 and figure 3.7 are consistent with this formulation and are well-approximated by such exponential decay. An extension of correlation coefficient is given in section 3.3.1.3.

$$C_{mn} = f(|z_m - z_n|, I_{\nu}, A/D)$$
(3.27)

4

# Results

This chapter presents the results from the application of the SROM model on a variety of the datasets. The application of Proper Orthogonal Decomposition (POD) is present in section 4.1. Subsequently, section 4.2 presents the results of the stochastic reduced order model (SROM) on the datasets. Section 4.3 discusses the application of the frequency-shift hypothesis and the application of the Grassmann-manifold. Lastly, section 4.4 present empirical fitting of empirically observed correlations of global bases.

# 4.1. Proper Orthogonal Decomposition

This section serves to illustrate the spatial and temporal modes that are obtained through proper orthogonal decomposition (POD). In this section the POD modes for the cylinder wake of quasi-2D flow case are illustrated for a wind speed  $19~{\rm m\,s^{-1}}$ . In section 4.1.1 the 3D simulated case for a stationary cylinder is illustrated. The POD modes for the  $11~{\rm m\,s^{-1}}$  dataset are presented in appendix A.

The data consists of 2000 time steps of the flow field taken at 20 Hz. In order to remove transience from the modes the first 300 time steps of the flow are excluded. This allows for the translation of the first vortices through the entire domain. The mean of the data is subtracted and a direct singular value decomposition (SVD) is taken.

Figure 4.1 presents the first five spatial modes extracted from the quasi-two-dimensional wake. Modes 1-2 constitute the canonical antisymmetric sine/cosine pair that reconstructs the von Kármán vortex street and account for the bulk of the fluctuation energy. Modes 3-4—and likewise modes 6-7 shown in figure 4.2—still exhibit the staggered vortex pattern, albeit with markedly reduced amplitude in certain regions of the flow. Their eigenvalues differ by less than 3% and modes 6-7 further form a pair of comparable energy.

Further observations of the modes can be made, namely that the w-component of the velocity is not captured with much structure. This is expected as in a quasi-2D simulation the w-component compared with the u and v-components has a much lower amplitude. The w-component of the modes capture the expanding wake pattern, but do not contain a distinguishable von Kármán patterns that are present in the u and v-components.

Figure 4.3 displays the power-spectral density (PSD) of the modal time series. The simulated wake has a Reynolds number of  $Re \approx 6.3 \times 10^6$ . At this high Reynolds number, the peak Strouhal number obtained from the simulation is appreciably higher than the value of St  $\approx 0.24$  reported in the literature for circular cylinders [13, 37]. Consequently, the dominant flow structures identified by the modal analysis occur at frequencies that do not coincide with those observed experimentally, and the remaining POD modes are likewise shifted in frequency.

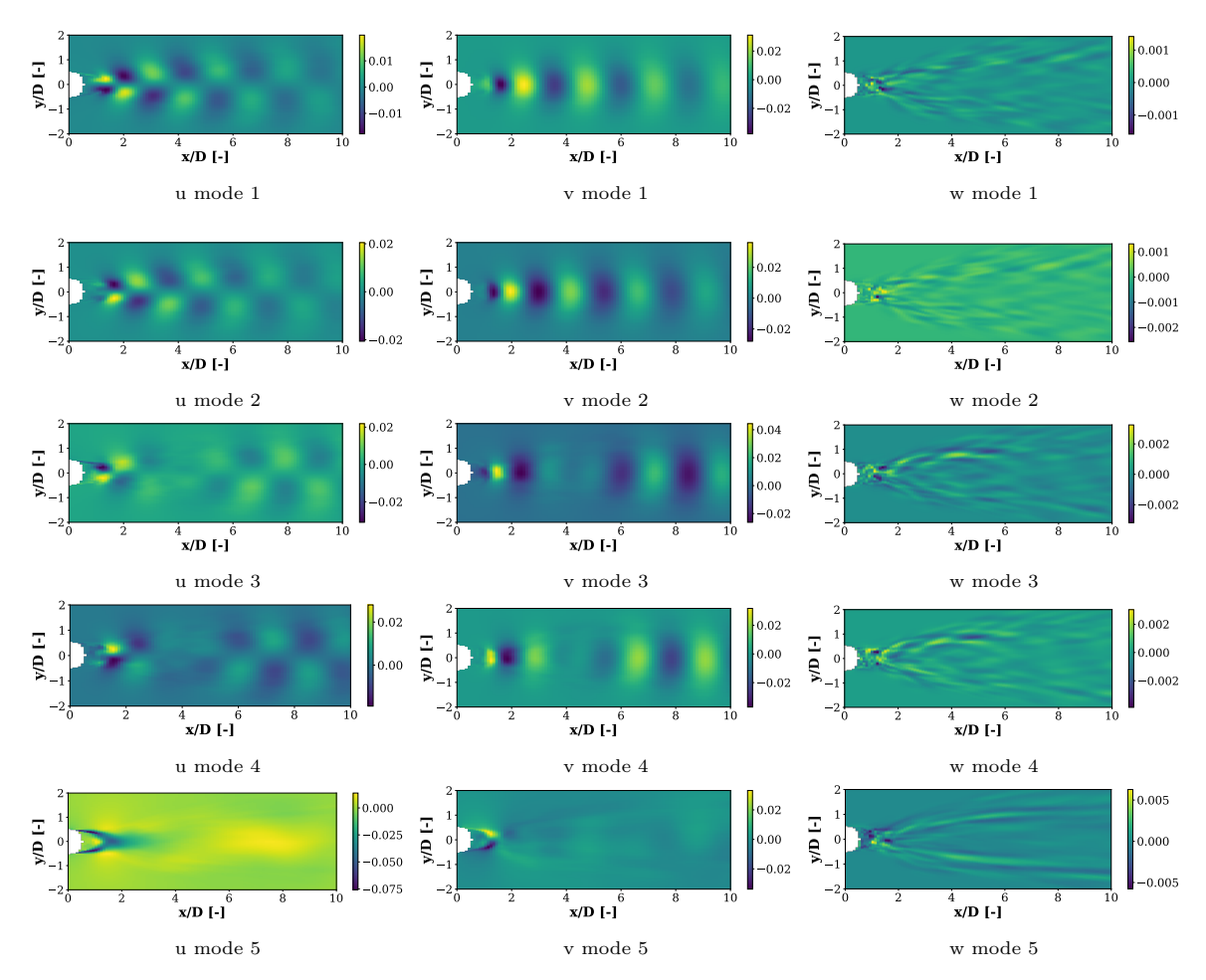


Figure 4.1: First five POD modes of the velocity components u, v, and w for the quasi-2D simulation.

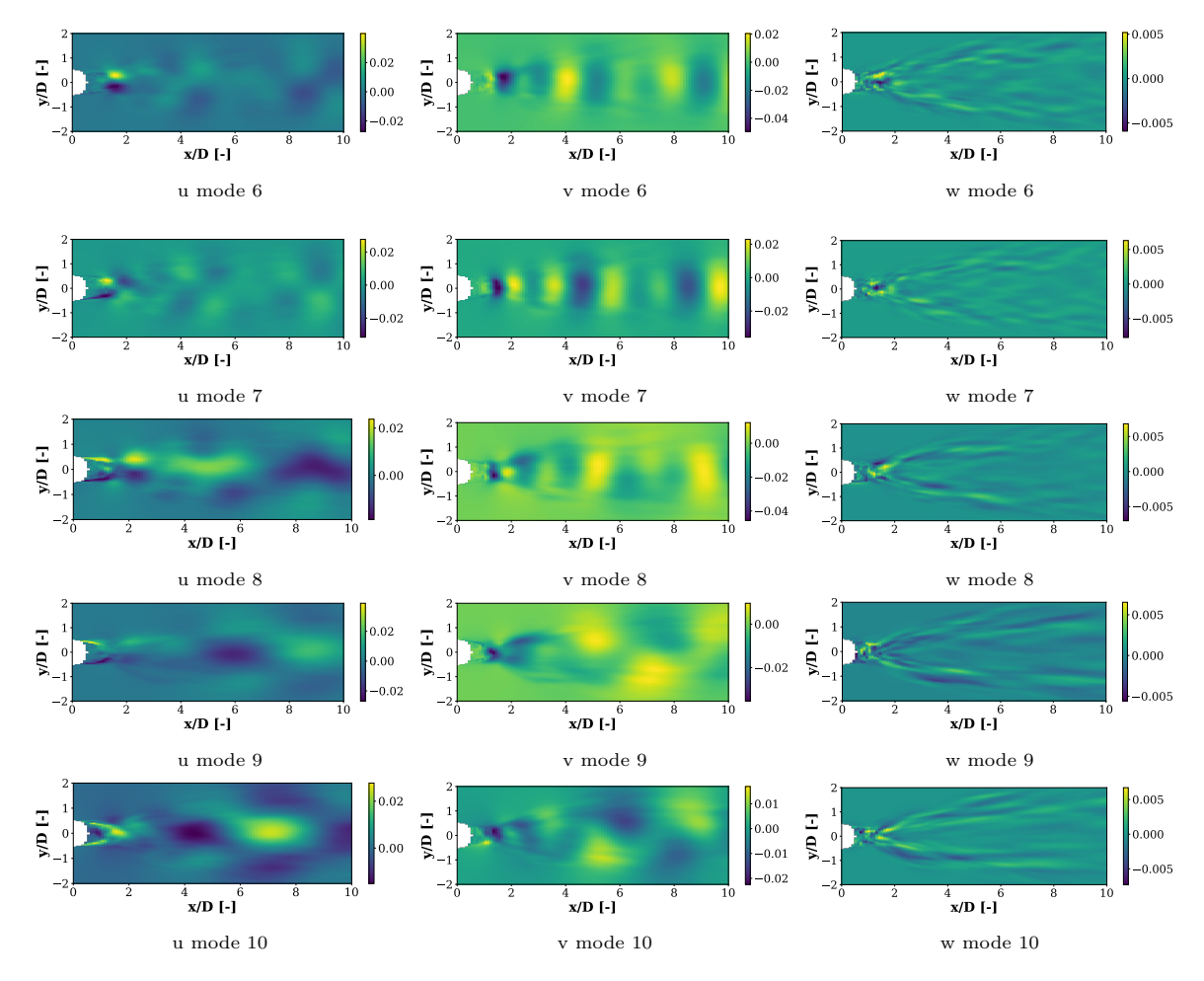


Figure 4.2: POD modes 6-10 of the velocity components u, v, and w for the quasi-2D simulation.

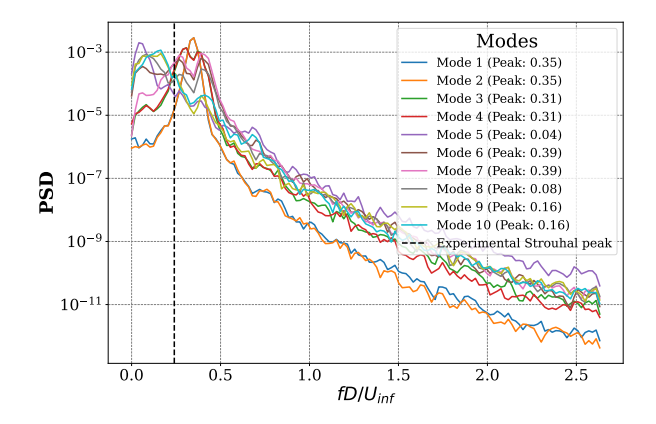


Figure 4.3: Power spectral density (PSD) of the quasi-2D modal time series at 19 m s<sup>-1</sup>

This discrepancy limits the quantitative accuracy of the present study in the spectral sense: while the spatial organisation of the von Kármán street is captured, its temporal signature is offset. Because the Detached-Eddy Simulation (DES) setup itself is not the focus of this thesis, a re-tuning of the numerical parameters lies outside the present scope. The modal decomposition nonetheless illustrates the structures. The frequency shift should be borne in mind during interpretation. Elevated Strouhal numbers are not unique to the current simulation; high-Reynolds-number DES studies of cylinders wakes report similar deviations [23, 24].

Mode 5 is similar in appearance to a slow-drift mode observed in [64, 65]. This mode encompasses the low-frequency perturbations in the near wake and reflects the slight, gradual changes in the shedding frequency. This is supported by the low frequency seen in the PSD at  $fD/U_{\rm inf}=0.04$ . Modes 8, 9 and 10 also exhibit predominantly low-frequency content. Multiple slow-drift modes have been noted previously [64]. Since these modes have a resemblance to the main slow-drift mode 5 these modes are also believed to be drift modes.

The duplication of the von Kármán street seen in the modes is not a higher harmonic: the power-spectral densities of the modal time series  $\phi_{3,4,6,7}(t)$  are very similar to the time series of the main mode pair  $\phi_{1,2}(t)$ . Instead, it is likely attributable to translation-induced rank inflation— an artefact that arises when space-only POD attempts to describe advecting structures [66]. Because each snapshot is analysed in a fixed spatial frame, even a slight downstream shift of a vortex core reduces snapshot-to-snapshot correlation; variance that would reside in a single mode pair is redistributed across several mode pairs.

[66] illustrate the mechanism with a synthetic wake comprising square vortices that translate along the streamwise axis. When the sampling interval is such that every vortex passes through many distinct x-locations, the POD rank inflates from two modes (perfectly periodic case) to a dozen or more; the variance lost from the leading pair re-appears in successive orthogonal pairs whose singular values differ by only a few per cent.

In a high-Reynolds-number cylinder wake the vortex street is only quasi-periodic: subtle cycle-to-cycle variations broaden the Strouhal peak. Consequently, a cluster of nearly equal singular values emerges, and the SVD spreads the vortex-street energy across several mode pairs, most prominently modes 3–4 and 6–7.

To remedy this duplication, [66] propose a co-moving decomposition known as permuted POD (PPOD). By permuting the data so that snapshots are indexed in the transverse direction while retaining the space—time coordinates along the advection path (s,t), PPOD aligns each vortex with itself; under this formulation the von Kármán street should condense into a single dominant mode—or, at most, one complex pair—thereby reducing the required number of modes of the reduced-order basis. Although PPOD is not explored in the present study, it offers a promising avenue for future work, particularly because it may reduce the amount of data required for converged modal reconstructions.

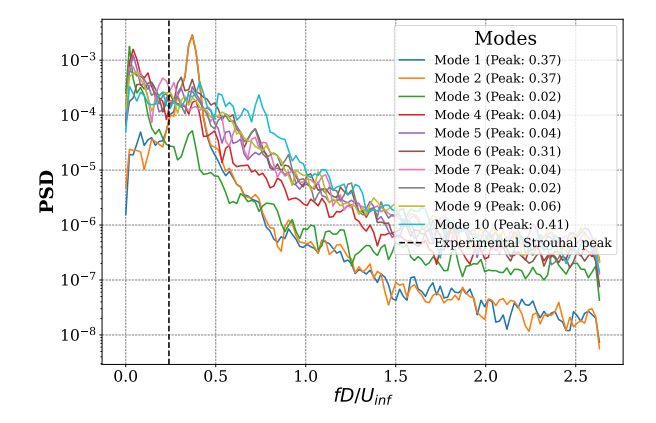


Figure 4.4: Power spectral density (PSD) of the 3D stationary cylinder modal time series at 19 m s<sup>-1</sup>

#### 4.1.1. 3D Stationary Cylinder

The 3D simulations contain data at multiple 2D slices at different heights along the cylinder inside a polar coordinate system. For a single slice, a weighted singular value decomposition is performed. The spacing in the radial direction and the angular direction are even. Therefore the weighted matrix  $\tilde{A}$  is defined element-wise as in equation (4.1). Here  $r_i$  is the radial coordinate corresponding to the *i*-th row of the matrix A.

$$\tilde{A}_{ij} = \sqrt{r_i} \cdot A_{ij} \tag{4.1}$$

This may equivalently be written in matrix notation as in equation (4.2). Here  $D_r$  is a diagonal matrix with entries  $(D_r)_{ii} = r_i$ .

$$\tilde{A} = D_r^{1/2} \cdot A \tag{4.2}$$

A direct SVD of the  $\tilde{A}$  is performed. The unweighted mode vectors U corresponding to the original (unweighted) matrix A are recovered through equation (4.3). Where  $\tilde{U}$  is mode vectors from the direct SVD of the  $\tilde{A}$  matrix.

$$U = D_r^{-1/2} \cdot \tilde{U} \tag{4.3}$$

A slice at height of Z/D=1.6 is chosen to be analysed as this is the slice that is nearest to the centre of the simulated domain. For best comparison with the quasi 2D simulation the stationary cylinder is chosen as it is not moving and has the most converged statistics due to the higher number of time steps. Every 5th time step is taken from the simulation. This means that the data entries in the data matrix are taken at 20 Hz. This results in the 3D case having an identical sampling frequency as the quasi-2D case. Again the mean of the data is subtracted. The first 1000 time steps, constituting the first 10 seconds of the data are excluded to remove the transience period of the simulation. The data matrix for the 3D case contains 1600 time snapshots while the quasi-2D data matrix contains 1700 time snapshots.

The 3D POD modes are illustrated in figure 4.5 and figure 4.6. The von Kármán street appears again clearly in the first mode pair. The PSD of the modes shown in figure 4.4 clarifies some of the differences seen between the quasi-2D modes and the 3D modes. The first difference is that the von Kármán street has a different peak at  $S_t = 0.37$  instead of  $S_t = 0.35$  seen in the quasi-2D case. This Strouhal number is again higher than reported in literature. The data covers 80 seconds of simulated time. At this Strouhal number that results in approximately 112 cycles. The likelyhood that the difference in  $S_t$  is attributable to the broadness of the Strouhal peak is therefore small. The Strouhal numbers are however similar and the difference is not significant.

The main drift mode for the 3D case appears as the third mode where it is seen as the fifth mode for the quasi-2D case. Furthermore, the first few modes for the 3D case appear to resemble more drift modes due to the low frequency content of their PSDs.

Mode 6 has a resemblance to the von Kármán street again. This is again likely attributable to the redistribution of variance across multiple modes as is proposed to be the reason for the resemblance seen in the quasi-2D case. In the quasi-2D case, the far field is included up to ten diameters downstream, while in the 3D case, only four diameters are considered. This reduced domain in the 3D setup is believed to delay the emergence of von Kármán-like structures to higher modes, whereas drift modes dominate earlier due to their association with the near wake region.

The w-component seen in the 3D modes has a greater relative magnitude as compared to the quasi-2D modes, although the difference remains modest. In the first mode pair the w-component is more discernable as an oscillatory von Kármán pattern than the quasi-2D case. The pattern is however still difficult to discern. Given that approximately 112 oscillatory cycles are captured, the dataset is assumed to be statistically converged. More data is not likely to improve the pattern. The w-component is difficult to capture and its presence is therefore concluded to not be significant despite the larger domain size of the 3D simulation.

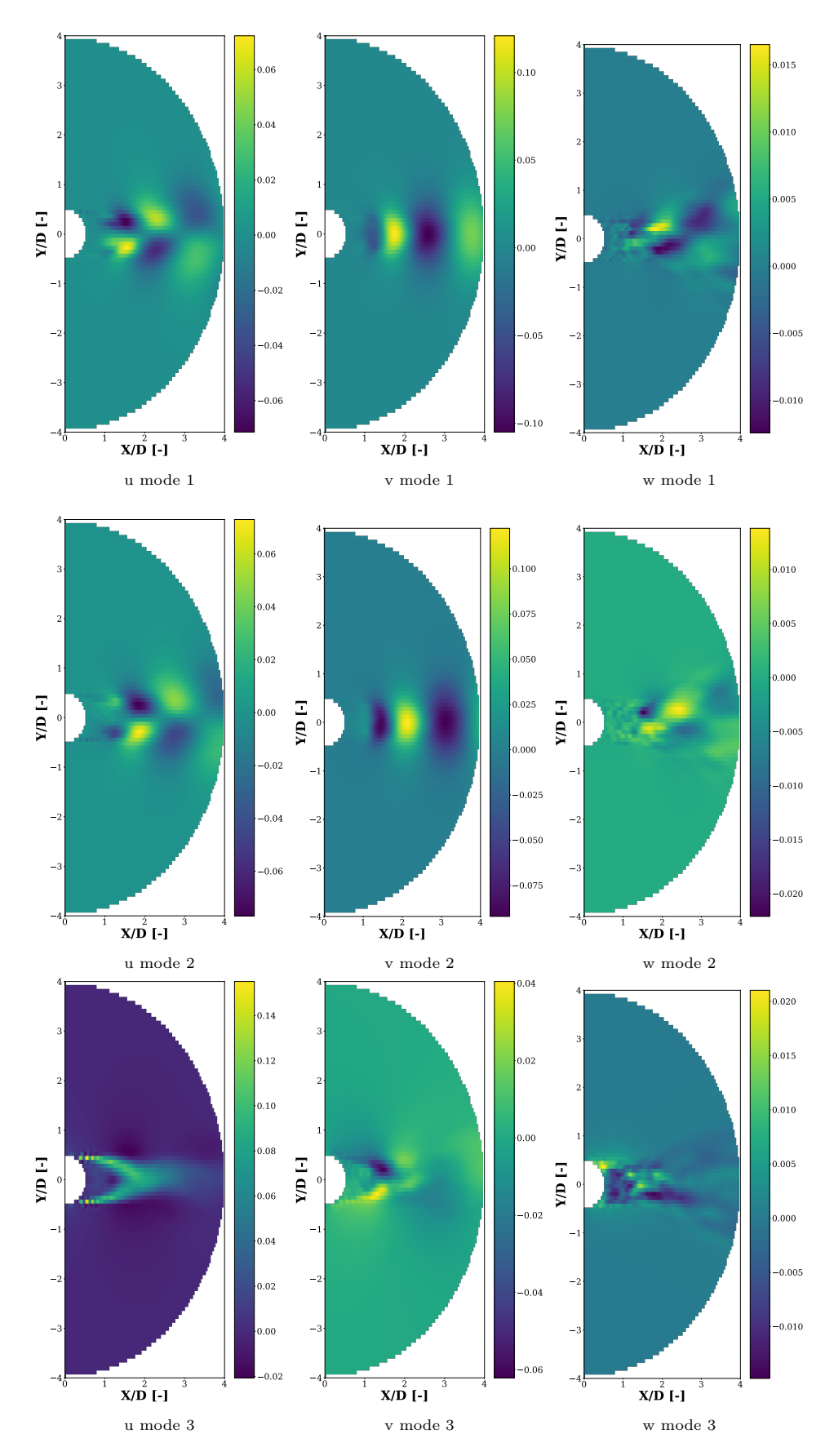


Figure 4.5: First three POD modes of the velocity components u, v, and w for the stationary cylinder at 19 ms<sup>-1</sup>

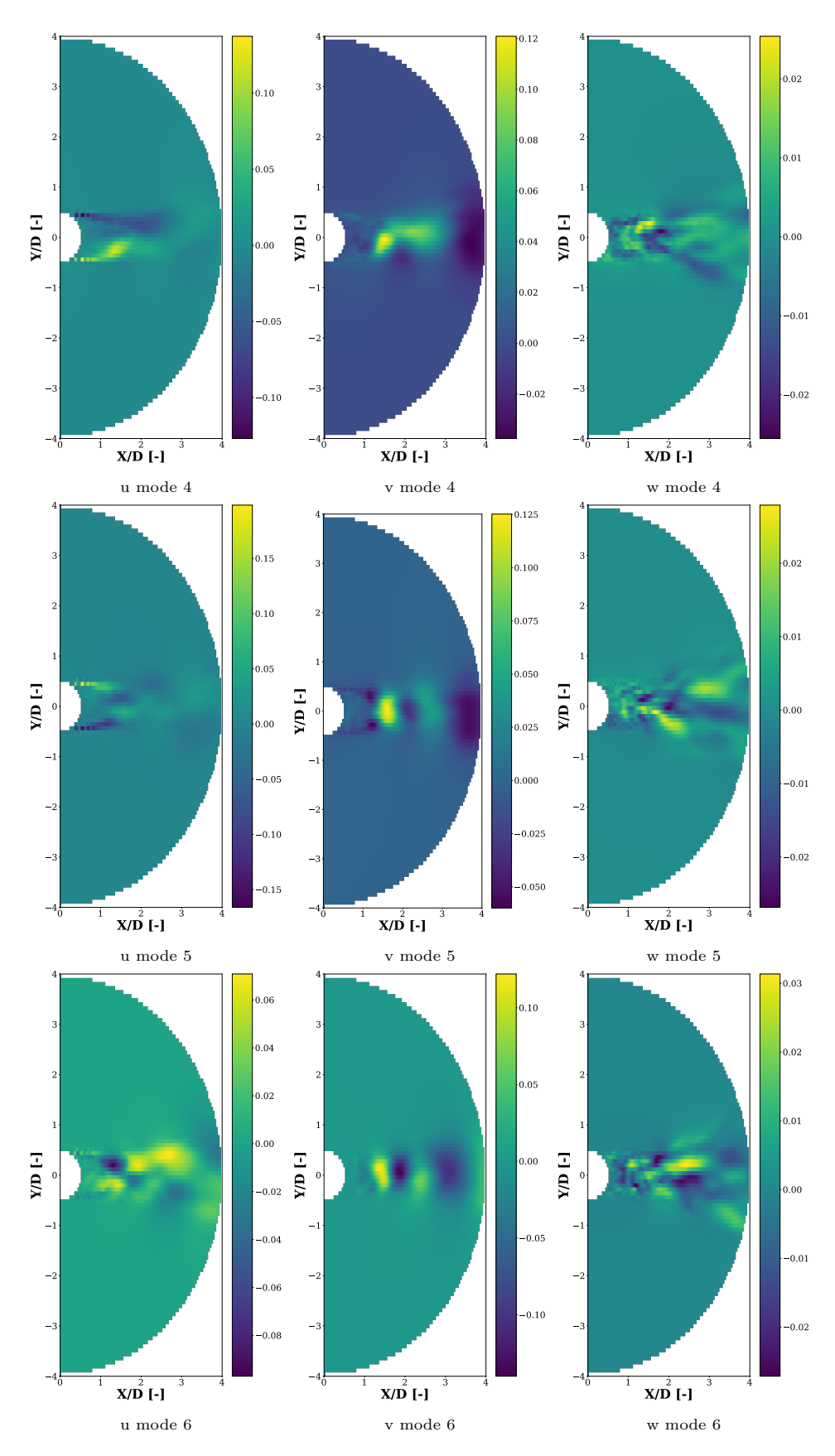


Figure 4.6: POD modes 4-6 of the velocity components u, v, and w for the stationary cylinder at 19 ms<sup>-1</sup>

# 4.2. Stochastic Reduced Order Model Results

This section presents the results of applying the stochastic reduced order model (SROM) to the quasi-2D cylinder simulation at  $19 \text{ m s}^{-1}$  and the 3D stationary cylinder. The focus is on comparing the stochastic realisations with the original simulation and assessing the effectiveness of the dimensionality reduction.

#### 4.2.1. Implementation of Stochastic Time Series Generation

The quasi-two-dimensional dataset at 19 ms<sup>-1</sup> is subjected to a direct singular value decomposition (SVD) to obtain the spatial modes in the matrix U, the singular values in  $\Sigma$ , and the temporal coefficients in  $V^{\mathsf{T}}$ . The spatial modes are shown in figure 4.1 and figure 4.2.

Figure 4.7 plots the singular values against the mode index, alongside markers for the 95 % energy cut-off and the optimal singular value hard threshold (SVHT). Both criteria reveal that a substantial number of modes must be retained to meet their respective thresholds. The 95 % energy criterion reduces the data volume by approximately 88 %, while the SVHT cut-off retains only around 45 % of the modes. Beyond the SVHT threshold, the remaining modes predominantly capture numerical noise and contribute little to the physical fidelity of the reconstruction. At lower Reynolds numbers far fewer modes are required to capture a significant amount of energy [64, 67, 68].

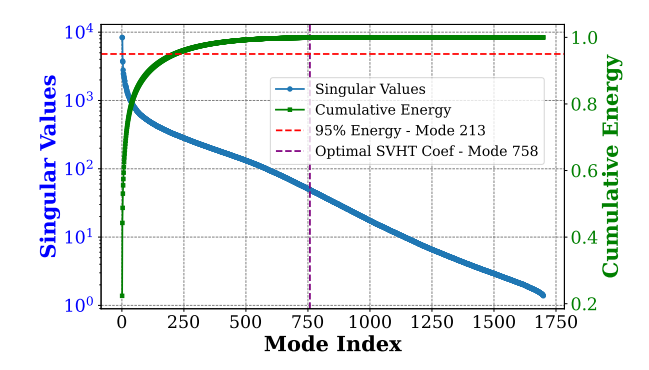


Figure 4.7: Singular values and cumulative energy of quasi-2D POD modes at 19 m s<sup>-1</sup>.

A cross-spectral block matrix is constructed as per equation (3.5) from the temporal matrix. New time series for the temporal modes are generated and spectral colouring is applied. The new temporal modes are given as per equation (3.7). A stochastic realisation of the flow is made is through the matrix multiplication as per equation (4.4).

Section 4.1 illustrates that the von Kármán street is spread out across many modes. A substantial number of dominant modes is therefore required to effectively capture this pattern. It is furthermore desirable to lower the likelihood that extreme values appear in the flow. Extreme values may occur when individual modes constructively combine and result in extreme flow velocities. The dominant m modes cut-off is chosen to be a total of 30 modes. This corresponds to approximately 80% of the energy in the flow. This is believed to be a fair trade-off between capturing the street effectively and keeping a reasonable amount of energy for stochastic realisations.

$$A_{\text{realisation}} = U_k \Sigma_k V_{\text{new } k}^{\mathsf{T}} \tag{4.4}$$

Individual realisations of the flow may differ from the original due to the randomised phases of the modes. This renders direct comparison between single realisations impractical. A previous implementation of the SROM [69] introduced the spectral error, defined in equation (4.5), to compare stochastic realisations. In this approach, the power spectrum of a velocity component at a fixed spatial point is compared to that of other realisations and to the original flow. This metric is, owing to Parseval's theorem [70], formally equivalent to comparing signal variances. A proof of this is given in appendix B.

$$E_{S_{-i,j}} \equiv \frac{\int \left(\hat{S}_i - \hat{S}_j\right) df}{\int \hat{S}_j df} \tag{4.5}$$

Since the focus here lies on ensemble statistics rather than pointwise variance, an alternative metric based on turbulent kinetic energy (TKE), averaged over multiple realisations, is adopted. The error metric that is adopted is shown in equation (4.7). Here  $\text{TKE}_{\text{error}}(x)$  is the error at a position x in the flow,  $\text{TKE}_{\text{generated}}(x)$  is the TKE of the generated flow field and  $\text{TKE}_{\text{original}}(x)$  is the TKE of the original flow. The flow field is inhomogeneous in nature. Therefore the TKE is calculated for each individual point. TKE is calculated as per equation (4.6).

$$TKE = \frac{u'^2 + v'^2 + w'^2}{2}$$
 (4.6)

$$TKE_{error}(x) = \frac{|TKE_{original}(x) - TKE_{generated}(x)|}{TKE_{original}(x)}$$
(4.7)

In figure 4.8a and figure 4.8b the  $TKE_{error}$  for the 95% energy cut-off and  $TKE_{error}$  for the SVHT cut-off can be seen. The energy cut-off criterion illustrates that the region near the cylinder is difficult to capture with the POD modes. This is a region of separated flow with strong turbulence due to the vortex shedding from the shear layers bounding the wake. The turbulent structures are badly captured by the low grid resolution and the low sampling frequency. Many modes are required to capture this region. For the purposes of a downwind idling situation this region is likely not important. Small turbulent structures do not have a significant influence on the blade motion and the blade will likely not be in this region when the blades are bent away from the structure.

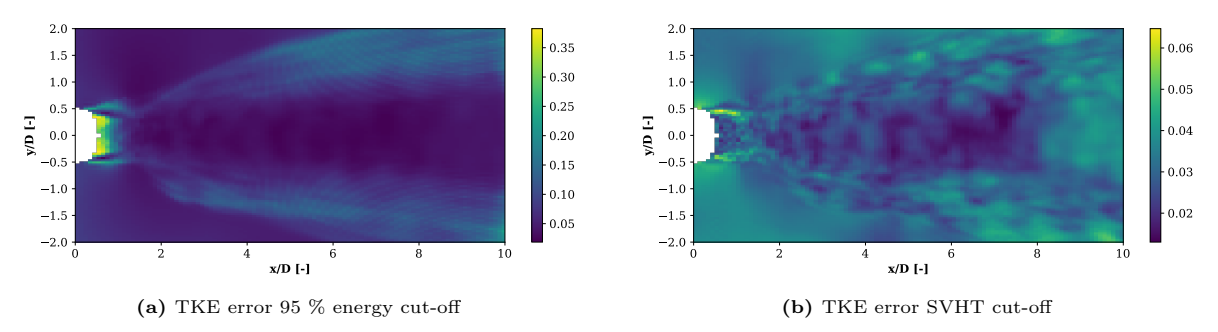


Figure 4.8: Turbulent kinetic over an average of 30 stochastic realisations.

Despite the SVHT cut-off capturing 99.9% of the energy in the flow in terms of the singular values the error metric in the remains in the order of a few percent. Despite the graph illustrating an averaging over 30 realisations the distribution of the error is noticeably less smooth than the 95 % energy cut-off. This illustrates that error metric fluctuates noticeably between realisations.

#### 4.2.2. 3D Simulation

As described in section 4.1.1 a weighted SVD is taken for the stationary cylinder at a slice height of Z/D=1.6. In figure 4.9 the singular values of the  $\Sigma$  matrix are plotted against the mode index. Notably the 95 % energy cut-off is significantly higher than the quasi-2D case at 383 modes. The optimal SVHT cut-off is also significantly closer to the energy cut-off. The SVHT cut-off is at approximately 98 % of the energy of the flow.

Stochastic realisations are generated with a dominant mode m cut-off chosen at 42 modes. This corresponds to approximately 60% of the energy in the flow. This cut-off contains more modes than the cut-off for the quasi-2D case, but is taken at a lower cumulative energy. Despite the lower energy cut-off less extreme values are observed. This is believed to be a result of the energy being more evenly spread

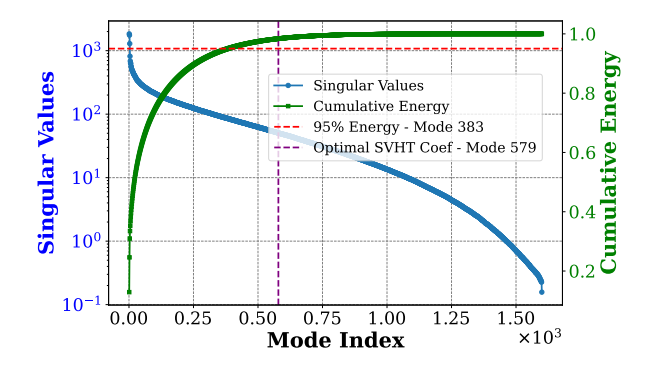


Figure 4.9: Singular values and cumulative energy of 3D flow case at slice height Z/D = 1.6 of stationary cylinder.

over the modes. The chance that many modes constructively combine and produce an extreme value is then lower. Very high localized values are simply a feature of the model and not necessarily wrong so long as their frequency matches real world events. Extreme events are seen in turbulence studies [71]. Quantifying the frequency of these events to better estimate a cut-off value is not further explored in this thesis.

In section 4.2.2 the  $TKE_{error}$  from equation (4.7) is plotted for both the 95 % energy and the SVHT cut-off. The errors are similar to the errors from the quasi-2D case in that the wake directly near the cylinder is difficult to capture and more modes are required. The wake further behind the cylinder can be captured with low errors. This is likely again due to low grid resolution and low sampling frequency. The SVHT cut-off only modestly lowers the error near the cylinder from around 40% to 25%.

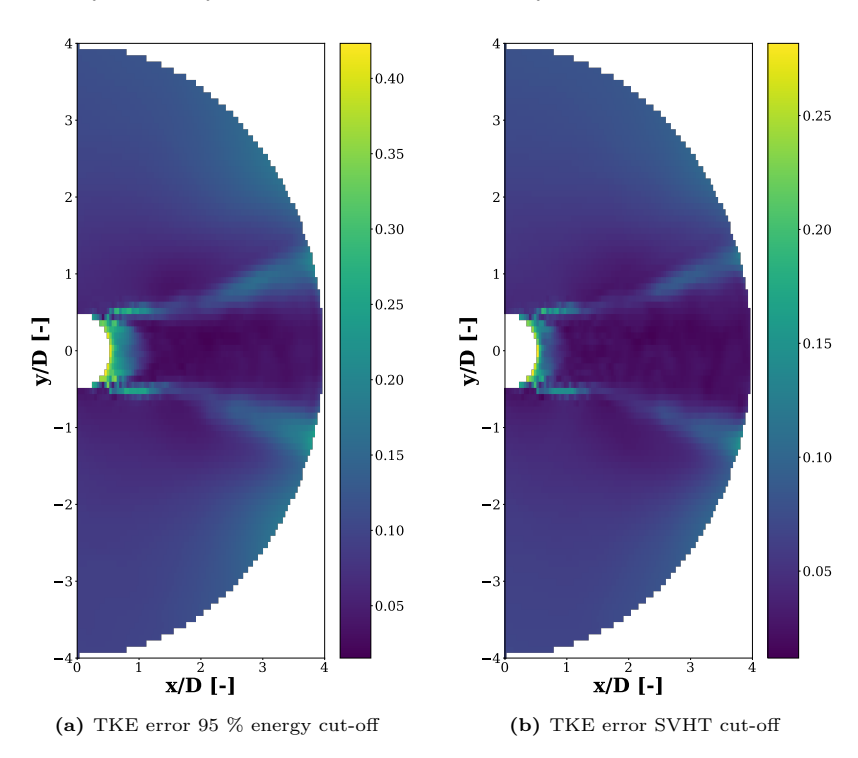


Figure 4.10: Stationary 3D simulation turbulent kinetic over an average of 30 stochastic realisations.

# 4.3. Verification of the frequency–shift hypothesis

The frequency–shift procedure described in section 3.3.1.1 assumes that the POD spatial modes are independent of Reynolds number, because only the temporal coefficients are rescaled. If the spatial structures change notably with Re, the entire premise is undermined.

#### 4.3.1. Direct Comparison of the Leading Modes

Figure 4.11 juxtaposes the first spatial mode computed from the 19 m s<sup>-1</sup> ( $Re_{19} \approx 6.3 \cdot 10^6$ ) dataset with its counterpart from the 11 m s<sup>-1</sup> case ( $Re_{11} \approx 3.7 \cdot 10^6$ ). Both datasets share an identical grid and number of time steps.

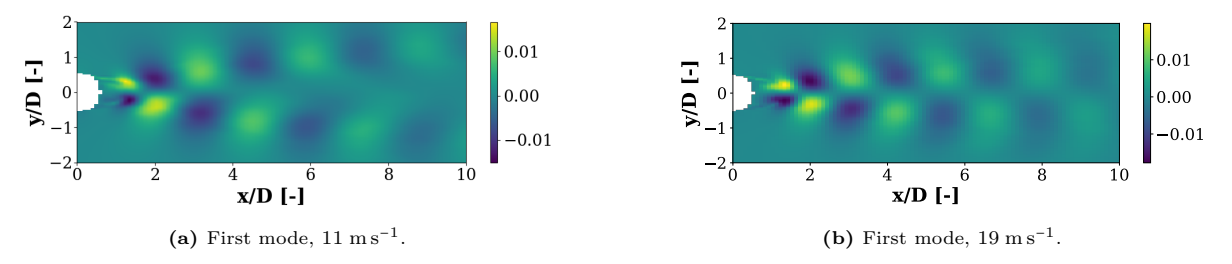


Figure 4.11: Leading u-component POD spatial mode at two wind speeds.

Even a cursory inspection reveals that the spatial patterns are not identical: eight shed vortices are visible at the higher velocity, but only seven at the lower one. The wavelengths of the vortices therefore appear to change between the Reynolds numbers. This discrepancy directly violates the requirement that the POD spatial modes can be applied as a global basis across multiple Reynolds numbers within these high Reynolds number regimes.

This difference in POD mode shape at these wind speeds likely stems from the difference in measured Strouhal number. The PSDs of the modes from both datasets may be seen in figure 4.12. It may be seen that the Strouhal number for the 19 m s<sup>-1</sup> case is approximately  $S_{t,19} = 0.35$  while the 11 m s<sup>-1</sup> it is approximately  $S_{t,11} = 0.32$ . The fraction of the Strouhal numbers is similar to the observed difference in visible vortexes with  $\frac{S_{t,11}}{S_{t,19}} \approx 7/8$ .

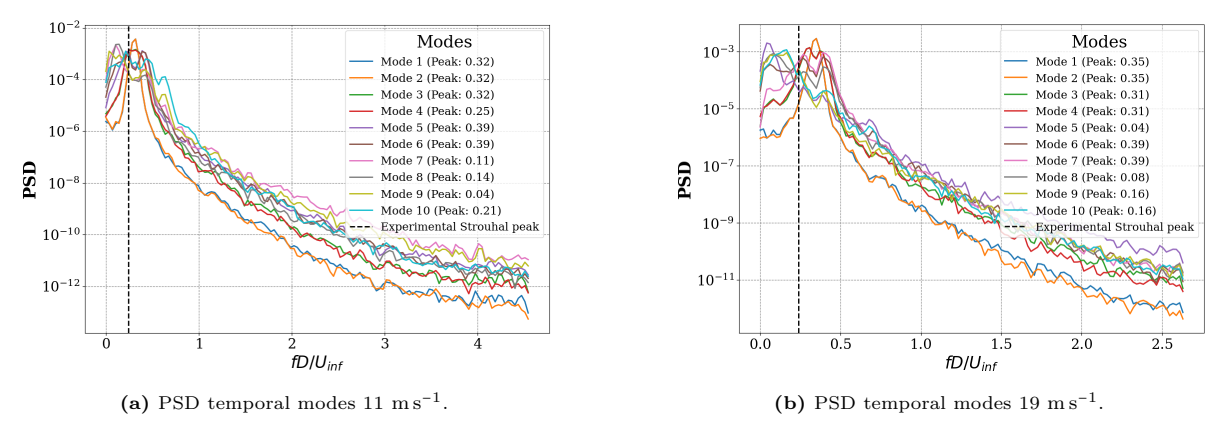


Figure 4.12: PSDs of the temporal modes of the 11 and 19 m s<sup>-1</sup> datasets.

Another observed difference in the mode shapes is the broadening of the pattern in the y-direction from the  $19~\rm m\,s^{-1}$  case to the  $11~\rm m\,s^{-1}$  case. These differences illustrate that the frequency-shift procedure cannot be applied, because both the Strouhal number and the spatial POD basis vary with Reynolds number. An alternative method to find the spatial modes alongside a modification of the frequency shift are required.

#### 4.3.2. Remedy via Grassmann-manifold Basis Interpolation

A more promising strategy is to adapt the spatial basis along with the Reynolds number. The subspace at an intermediate velocity  $15~{\rm m\,s^{-1}}$  may be obtained from two known bases at wind speeds  $11~{\rm m\,s^{-1}}$  and  $19~{\rm m\,s^{-1}}$  through the Grassmann-geodesic interpolation of [72]. This section serves to describe this method.

The Grassmann manifold  $\mathcal{G}(r,n)$  is the set of all r-dimensional linear subspaces of  $\mathbb{R}^n$ . Every orthonormal matrix  $U \in \mathbb{R}^{n \times r}$  whose columns span such a subspace represents a point on  $\mathcal{G}(r,n)$ . Because different matrices may span the same subspace (they differ by a right-hand rotation), the Grassmann manifold is curved: moving from one subspace to another cannot, in general, be described by simple vector addition.

Given two POD bases  $U_{11}^{(k)}$  and  $U_{19}^{(k)}$ , truncated to their first k energy-dominant modes, are interpreted as points on  $\mathcal{G}(k,n)$ . The shortest path between two points on a manifold is a geodesic. By travelling half-way along the geodesic that connects  $U_{11}^{(k)}$  to  $U_{19}^{(k)}$  a third point whose span is expected to approximate the flow at the mid-range speed of 15 m s<sup>-1</sup> is obtained.

Let  $U_{11}^{(k)}, U_{19}^{(k)} \in \mathbb{R}^{n \times k}$  be the truncated mode matrices at 11 and 19 m s<sup>-1</sup>, respectively. Denote the target velocity by  $s_* = 15 \text{ m s}^{-1}$  and define the normalised parameter w as in equation (4.8).

$$w = \frac{s_* - 11}{19 - 11} = 0.5\tag{4.8}$$

The algorithm for obtaining the basis  $U_{15}$  at a wind speed of 15 m s<sup>-1</sup> consists of two steps:

1. Log map. Compute the projection of  $U_{19}^{(k)}$  onto the tangent space at  $U_{11}^{(k)}$  as in equation (4.9).

$$M = (U_{11}^{(k)})^{\mathsf{T}} U_{19}^{(k)}, \quad B = (U_{19}^{(k)} - U_{11}^{(k)} M) M^{-1}$$
(4.9)

The thin SVD  $B = U\Sigma V^{\mathsf{T}}$  yields the principal angles  $\Theta = \arctan \Sigma$ .

2. **Geodesic step.** Move the fraction w along the geodesic per equation (4.10)

$$U_*^{(k)} = U_{11}^{(k)} V \cos(w\Theta) + U \sin(w\Theta) V^{\mathsf{T}}$$
(4.10)

[72] do not specify a specific amount of modes to utilize. It is however seen that including the weakly converged higher order modes can worsen the geodesic fit. This is illustrated in the subsequent section.

#### 4.3.3. Application of Grassmann-Manifold Basis

The *u*-component modes from the quasi-two-dimensional simulation at 15 m s<sup>-1</sup> are compared with modes obtained by Grassmann-manifold interpolation. A cut-off of k = 20 is adopted throughout. The reference POD modes and their Grassmann counterparts are shown side-by-side in figures 4.13 and 4.14.

The Grassmann-interpolated basis reproduces the first POD pair well. The amount of vortices matches and the interpolated basis captures the expanding wake pattern. Those two features are the main differences observed in the comparison of the  $19~{\rm m\,s^{-1}}$  and  $11~{\rm m\,s^{-1}}$  cases.

Disparities do arise at the higher orders. Modes 3 and 4 exhibit a noticeable phase shift in the near wake, while modes 7 and 8 appear closer to the negative counterpart of the POD mode. This behaviour is not an error but a consequence of the interpolation acting on the span of each basis: the resulting set remains orthonormal, yet individual modes are free to rotate within that subspace and need not share the phase of the reference POD modes.

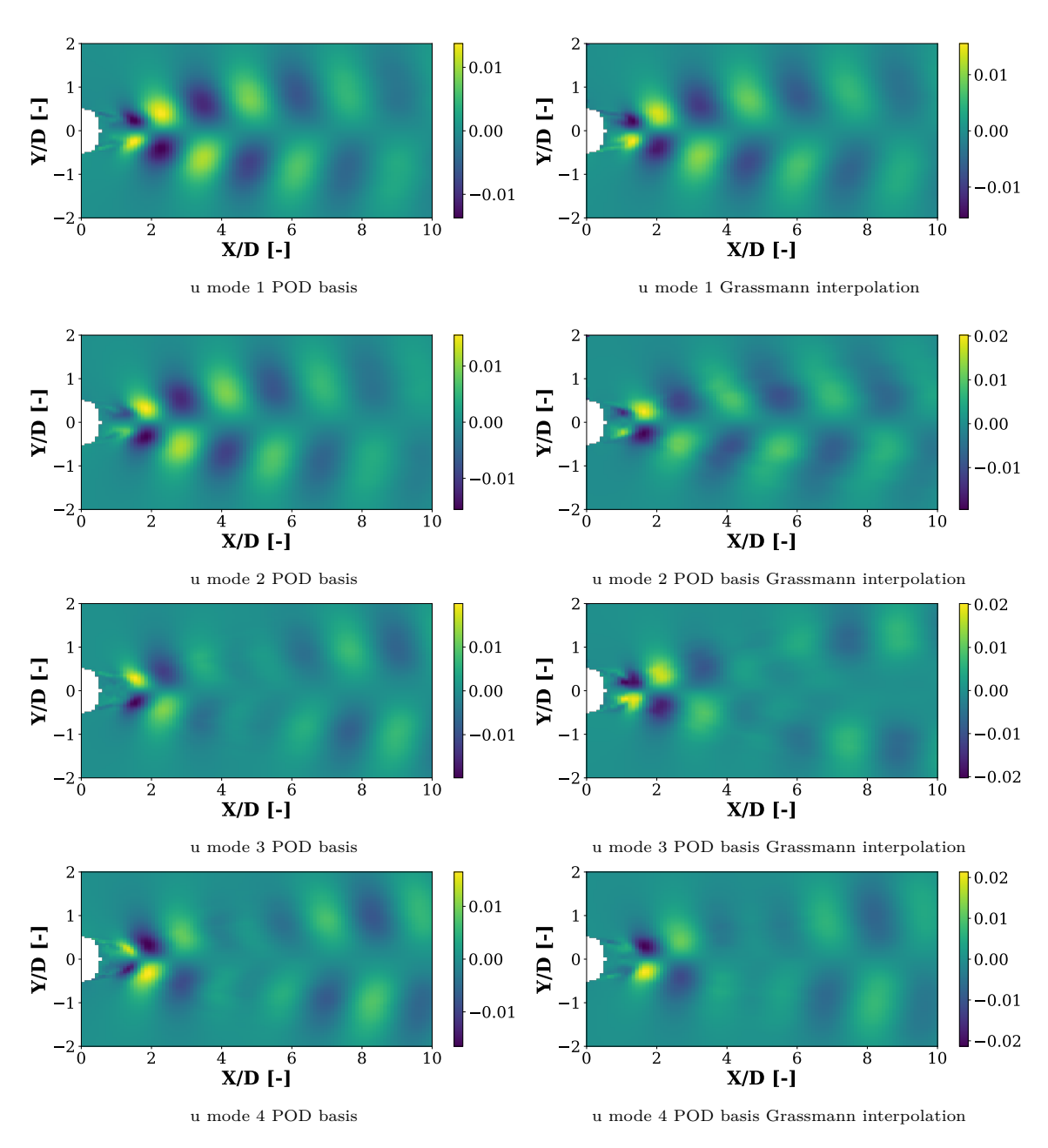


Figure 4.13: Modes 1-4 of POD basis from  $15~\mathrm{m\,s^{-1}}$  case alongside Grassmann-interpolated basis

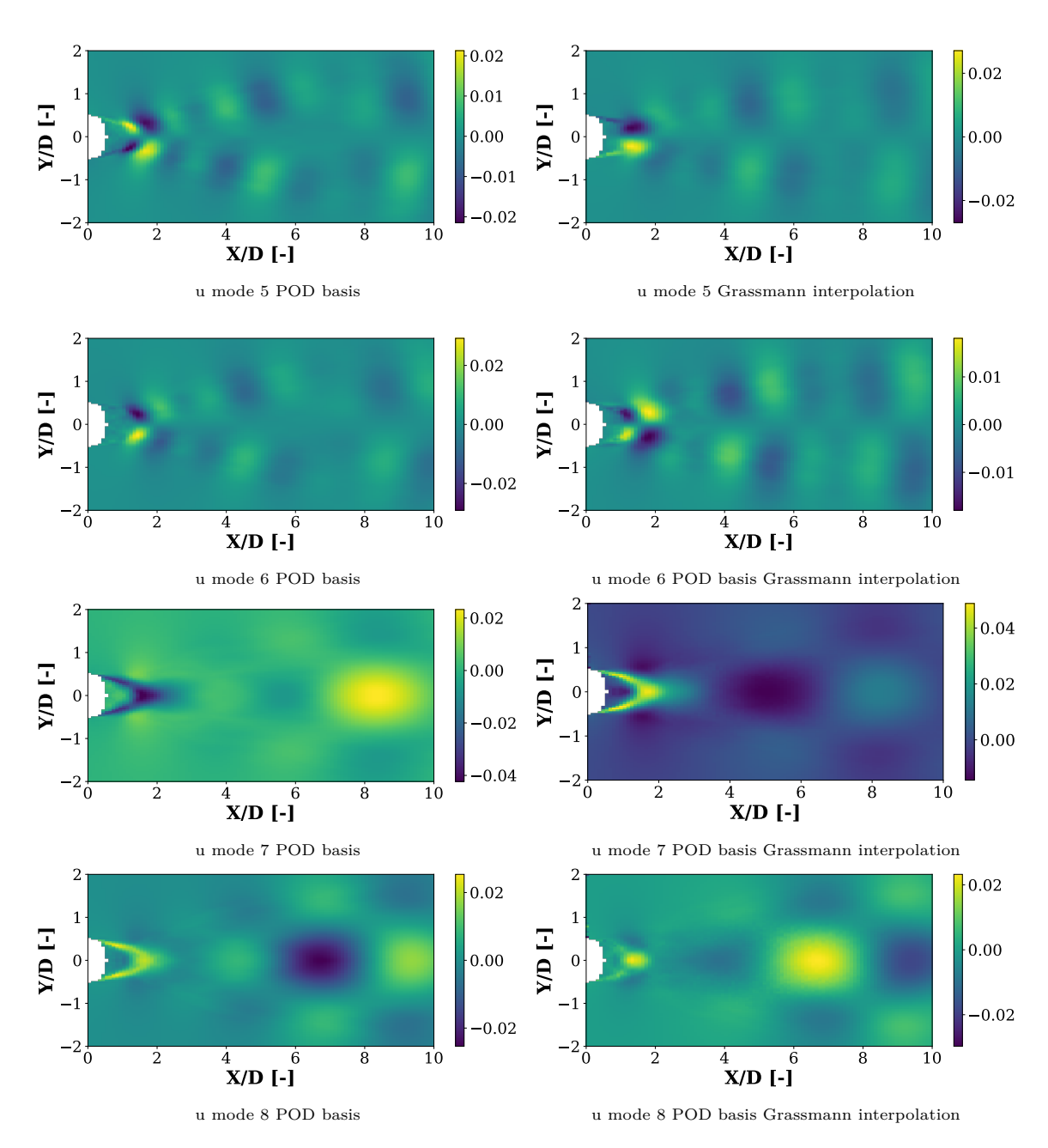


Figure 4.14: Modes 5-8 of POD basis from  $15~\mathrm{m\,s^{-1}}$  dataset alongside Grassmann-interpolated basis.

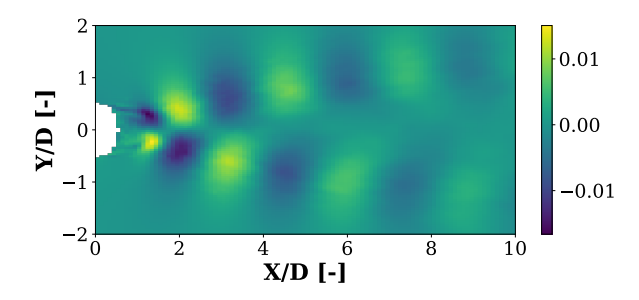


Figure 4.15: u-component of the first mode of the full Grassmann interpolated space.

The geodesic step may be applied for the complete bases.  $U_{11}^{(k)}$  and  $U_{19}^{(k)}$  are then taken with k being the rank of the bases matrices. When k is taken to be the rank of the bases matrices, the interpolated first u-mode is less smooth, as shown in figure 4.15, whereas the truncated choice shown in figures 4.13 and 4.14 this first mode is more smooth. An investigation to determine where the quality of the modes deteriorates is not further explored in this thesis.

In order to assess how representative the interpolated modes are of the POD basis of the  $15~\mathrm{m\,s^{-1}}$  dataset the Modal-Assurance Criterion (MAC) [73] is adopted. The formulation of the MAC is shown in equation (4.11).

$$MAC_{ii} = \left| \left( U_{15}^{\mathsf{T}} U_{15, Grassmann} \right)_{ii} \right| \tag{4.11}$$

Here  $U_{15}$  is the spatial mode matrix of the 15 m s<sup>-1</sup> dataset,  $U_{15,Grassmann}$  the mode matrix obtained through the Grassmann-interpolation method. A MAC value of 1 indicates identical modes; values below about 0.8 mark noticeable deviations.

The modes that are found by applying the geodesic step are not necessarily in phase with the POD modes. This is because the Grassmann interpolation preserves the span and mode pairs may be rotated. Considering the first two orthonormal spatial modes of the Grassmann interpolated method in figure 4.13  $u_{\text{grass},1}$  and  $u_{\text{grass},2}$ . A phase advance of  $\varphi$  radians is realised by the planar rotation as per equation (4.12).

$$\begin{pmatrix} u_{\text{grass},1} & u_{\text{grass},2} \end{pmatrix} = \begin{pmatrix} u_{\text{grass},1} & u_{\text{grass},2} \end{pmatrix} \mathbf{R}^{\mathsf{T}}(\varphi), \quad \mathbf{R}(\varphi) = \begin{pmatrix} \cos \varphi & -\sin \varphi \\ \sin \varphi & \cos \varphi \end{pmatrix}. \tag{4.12}$$

Because  $\mathbf{R}(\varphi)$  is orthogonal, the rotated pair  $u_{\mathrm{grass},1}, u'_{\mathrm{grass},2}$  remains orthonormal and spans the same two-dimensional subspace as the original modes; only the phase reference has changed. Such a rotation is an equally valid solution on the Grassmann manifold. An illustration of this is given in figure 4.16. Here the first grassmann mode  $u_{\mathrm{grass},1}$  is rotated 45 degrees.

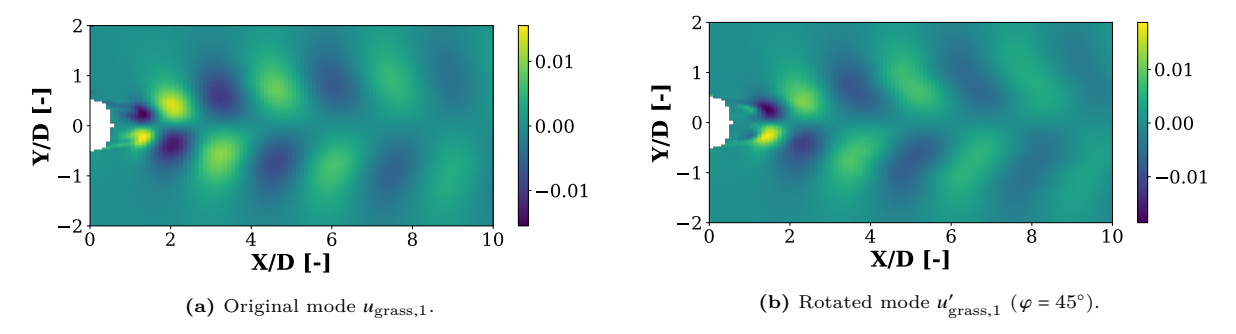


Figure 4.16: Effect of a 45° phase rotation on the first member of an oscillatory mode pair. The vortex pattern is shifted in phase by a quarter cycle.

In figure 4.17 the first three mode pairs are rotated in each of the planes that they span. The MAC is calculated for each angle. It may be seen that their exists an optimal angle that maximizes the MAC for these modes that is not necessarily at 0 degrees.

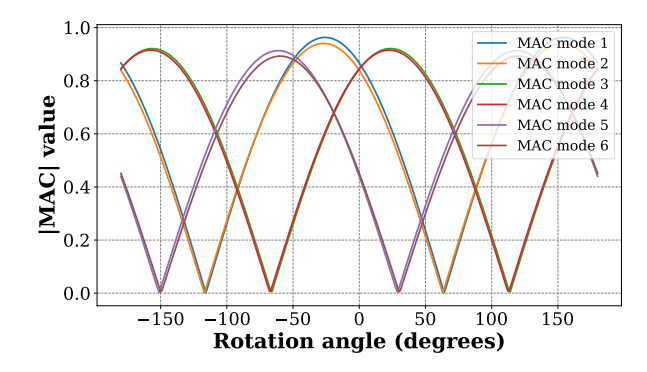


Figure 4.17: Modal assurance criterion (MAC) as function of planar rotation angle.

The geodesic step is performed at a range of wind speeds between 11 and 19 m s<sup>-1</sup>. The mode pairs are rotated to their respective optimum angles to maximize the MAC of each mode pair. This calculation is performed for only the first mode pair, the first two mode pairs and the first three mode pairs. In figure 4.18 the average value of the MAC is illustrated for the range of wind speeds. It may be seen that the first mode pair can attain 99 % alignment with the first POD mode pair. The optimum is better than that of either side of the geodesic, but not in the centre at 15 m s<sup>-1</sup>. The unrotated mode pairs perform worse and their curves have the same shape as the optimum curves.

The third mode pair, despite being optimally rotated, performs noticeably worse than the first and second mode pairs. The average value of the MAC drops and the optimum wind speed lies at around 12  $\rm m\,s^{-1}$  instead of residing around 14  $\rm m\,s^{-1}$ . The performance of the Grassmann-manifold interpolation diminishes for higher order modes quickly. The alignment of the first mode pair is significantly higher than that of the POD modes from the 11  $\rm m\,s^{-1}$  and 19  $\rm m\,s^{-1}$  datasets. Therefore the method effectively works to predict the first mode pair.

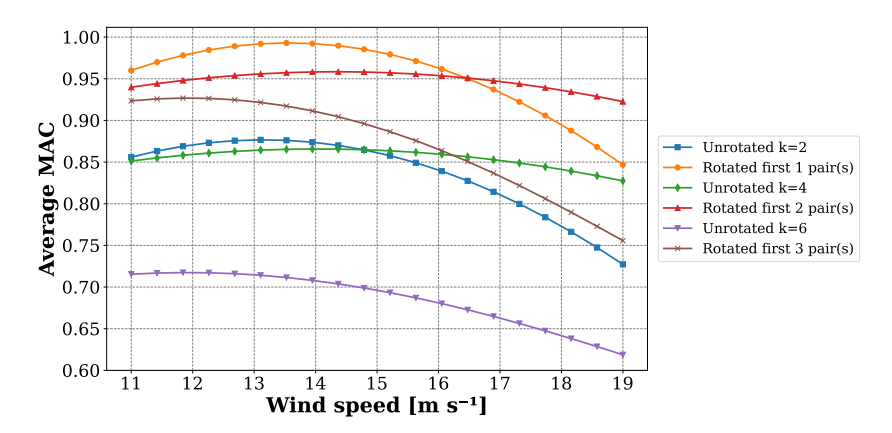


Figure 4.18: Average modal assurance criterion MAC of different mode pairs.

#### 4.3.4. Strouhal-Consistent Temporal Stretching

The vortex–shedding frequency of a circular cylinder is governed by the Strouhal relation of equation (4.13), where  $U_{\text{inf}}$  is the free stream velocity and D is the cylinder diameter.

$$f = S_t \frac{U_{\text{inf}}}{D} \tag{4.13}$$

Section 4.3.1 illustrates that the wake topology changes because St(Re) rises from  $St_{11} \approx 0.32$  at 11 m s<sup>-1</sup> to  $St_{19} \approx 0.35$  at 19 m s<sup>-1</sup>. The correct frequency shift must therefore match the actual shedding frequencies, not merely the ratio U/D as is proposed in section 3.3.1.1.

Let a reference temporal mode  $\phi_{\rm ref}(t)$  possess a spectral peak at  $f_{\rm ref} = {\rm St}_{\rm ref} U_{\rm ref}/D_{\rm ref}$ . To transplant that mode to a target operating point  $(U_{\star}, D_{\star}, {\rm St}_{\star})$  the time axis is stretched by the factor of equation (4.14).

$$\beta = \frac{f_{\text{ref}}}{f_{\star}} = \frac{\text{St}_{\text{ref}} U_{\text{ref}} D_{\star}}{\text{St}_{\star} U_{\star} D_{\text{ref}}}$$
(4.14)

The factor  $\beta$  is applied to every time series obtained from the 19 m s<sup>-1</sup> dataset. Since time series are stretched uniformly the phase relationships between the modes remain. The observed Strouhal number at 15 m s<sup>-1</sup> is  $S_t = 0.34$ ; all time series are therefore stretched to match this frequency.

In figure 4.19a the PSD of the temporally stretched time series may be seen. Time stretching behaves as a low-pass filter, hence the drop in PSD at high frequencies. The temporal components of the first few modes relate to the lower frequency component of the flow and are therefore not significantly influenced by the application of this method. In figure 4.19b the PSD of the modes from  $15~{\rm m\,s^{-1}}$  may be seen. The PSDs of the first few modes align well with the modes of temporally stretched dataset. The remaining modes do not have matching PSDs, but are relatively close with peaks at approximately the same values. Modes are also observed to be reordered for the  $11~{\rm m\,s^{-1}}$  and  $19~{\rm m\,s^{-1}}$  datasets. Namely that POD mode 5 aligns with Grassmann mode 7 in spectral content.

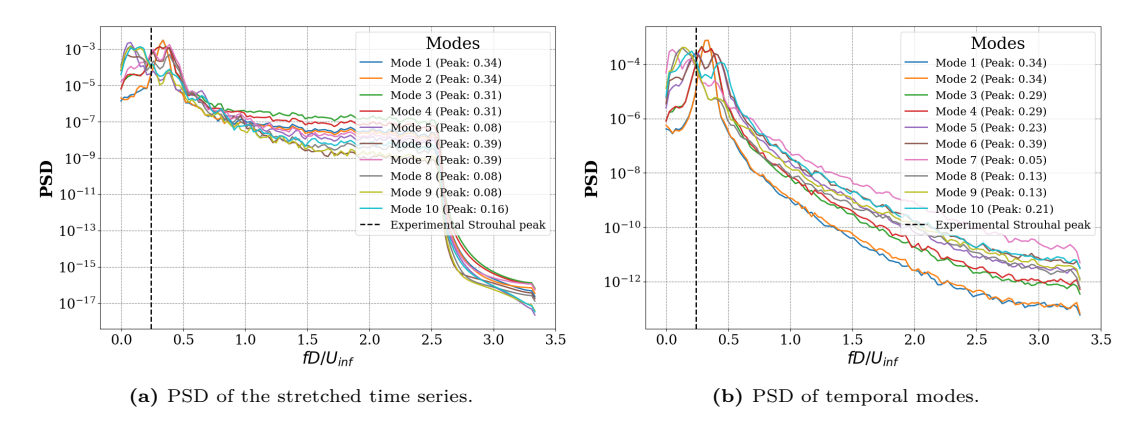


Figure 4.19: PSDs of the stretched  $19~\mathrm{m\,s^{-1}}$  dataset and the temporal modes from the  $15~\mathrm{m\,s^{-1}}$  dataset.

New realisations of the flow are made with stochastic realisations of the new time series by applying equation (3.7). The geodesic step is applied at a wind speed  $U_{\rm inf} = 15~{\rm m\,s^{-1}}$  for the first  $k = 20~{\rm modes}$ . The resulting basis  $U_{15,{\rm Grassmann}}^{(20)}$  is tested with the new temporal modes.

A realisation of the flow is made as per equation (4.15). Here  $A_{\text{realisation,Grassmann}}$  is the data matrix of the flow realisation,  $\Sigma_{15,k}$  the first k singular values from the SVD of the 15 m s<sup>-1</sup> dataset and  $V_{\text{stretch},k}^{\mathsf{T}}$  the first k temporally stretched modes from the 19 m s<sup>-1</sup> flow case.

$$A_{\text{realisation,Grassmann}} = U_{15,\text{Grassmann}}^{(20)} \Sigma_{15,k} V_{\text{stretch},k}^{\mathsf{T}}$$

$$\tag{4.15}$$

The singular values  $\Sigma_{15,k}$  cannot be known without the 15 m s<sup>-1</sup> flow. The singular values should lie somewhere between the singular values of  $\Sigma_{11,k}$  and  $\Sigma_{19,k}$  corresponding to 11 m s<sup>-1</sup> and 19 m s<sup>-1</sup> cases

respectively. By utilizing the singular values of the  $15~{\rm m\,s^{-1}}$  dataset the comparison to the flow generated with the Grassmann modes is easier. The uncertainty from introducing this additional parameter is then reduced.

In order to assess how well  $A_{\text{realisation,Grassmann}}$  compares with the flow from the 15 m s<sup>-1</sup> dataset the first flows consisting of the first k = 20 modes from both flows are compared. The TKE<sub>error</sub>(x) of equation (4.7) is calculated for the 15 m s<sup>-1</sup> dataset using the first k = 20 modes. This error is then the error that is obtained from performing a cut-off at 20 modes.

In figure 4.20a the error metric is illustrated. Similarly to the  $11~{\rm m\,s^{-1}}$  and  $19~{\rm m\,s^{-1}}$  flow cases the main error of the flow realisation comes from the near wake behind the cylinder.

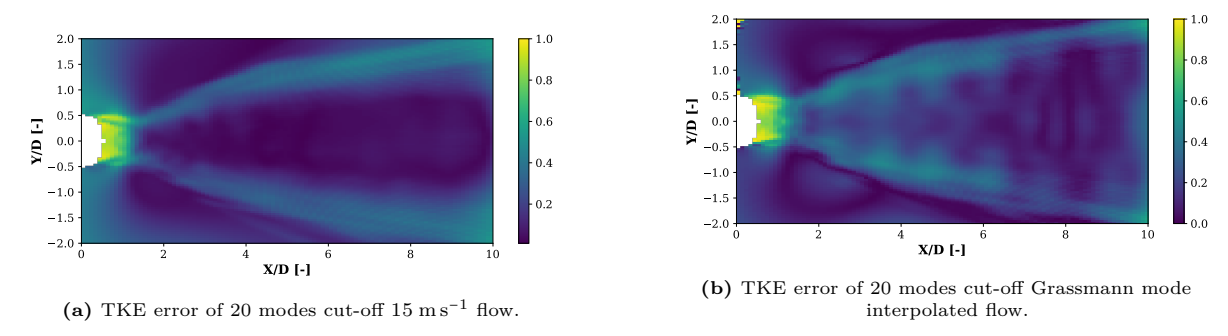


Figure 4.20: TKE error of 20 modes cut-off original 15 m s<sup>-1</sup> flow and Grassmann mode interpolated flow.

A total of 30 realisations of  $A_{\rm realisation, Grassmann}$  are made. The average  ${\rm TKE_{error}}(x)$  of these realisations are shown in figure 4.20b. The errors are higher than the errors seen in figure 4.20a. Again the near wake region is difficult to capture. The difference to the rest of the domain is less significant and the errors are overall higher, but similar in location. Some errors are seen near the border at (X/D,Y/D)=(0,2.0), likely introduced by numerical noise in the interpolation.

In figure 4.21 the absolute of TKE between figure 4.20a and figure 4.20b is shown. Differences of around 30 % are seen at significant locations inside the flow.

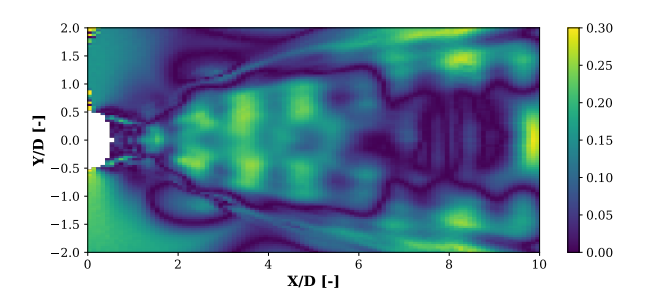


Figure 4.21: Absolute TKE error difference of POD flow and Grassmann flow.

The PSD assigned to a mode need not match its expected spatial pattern. This means that the associated singular value and time series of the modes are not assigned correctly. Hence, the modes at these different Reynolds numbers are reordered differently with respect to their singular values. The corresponding energy contribution is different and the assignment of time series from one simulation cannot be applied without manually verifying that the modes and time series are correctly matched.

The modes may also simply not be similar enough. The MAC values indicate that the modes are similar for the first few modes, but the resemblance quickly diminishes for later modes. The PSDs of figure 4.19 show that the main peak for the first mode pair can be matched by applying the frequency shift. The frequency shift seems to be applicable for higher modes likewise, but small differences do emerge in the location of the peaks and the shape of the PSDs. Figure 4.18 indicates that the interpolated modes perform better when the geodesic step is taken at a slightly lower wind speed. The order of PSDs of the

modes from the  $11~\rm m\,s^{-1}$  dataset are more in line with the PSDs of the temporal modes of the  $15~\rm m\,s^{-1}$  dataset. By applying the frequency shift from the modes of  $11~\rm m\,s^{-1}$  dataset the method may perform better.

The modes that are found by applying the geodesic step are not necessarily in phase with the POD modes. This is because the Grassmann interpolation preserves the span only and mode pairs may be rotated. The time series of the SROM model requires that spatial modes are in a certain phase with respect to each other to be applicable. Despite the PSDs looking similar through the stretching of the time series the phase alignment of the dominant spatial modes with the time series is not clearly enforced.

This becomes evident when comparing the cross-spectral density (CSD) of the velocity signals from a stochastic realisation and comparing them to the velocity signals from the dataset. One realisation of the flow is made from the first six POD modes and the original time series that correspond to these six modes as per equation (4.16). Here  $A_{\text{original}}^{(6)}$  is the realisation of the flow with only 6 modes.  $U_{15}^{(6)}$  the first six columns of the  $U_{15}$  matrix,  $\Sigma_{15}$  the singular values of the 15 m s<sup>-1</sup> dataset and  $V_{15}^{\mathsf{T}}$  the time series of the modes from the 15 m s<sup>-1</sup> dataset.

$$A_{\text{original}}^{(6)} = U_{15}^{(6)} \Sigma_{15} V_{15}^{\mathsf{T}} \tag{4.16}$$

A stochastic realisation is made utilizing the first six Grassmann modes alongside the stretched time series from the  $19~{\rm m\,s^{-1}}$  dataset. For this realisation the CSD of the time series of the modes are calculated as per equation (3.7). All six modes are then correlated and therefore no random phase is introduced.

For both the Grassmann-based and POD-based realisations, the CSD of the u-velocity component is computed at two locations, (x, y) = (12, 1) and (x, y) = (20, 1), and the results are compared. In figure 4.22a the PSD at the locations in the flow is illustrated. The PSDs agree reasonably well. In figure 4.22b the phases at each frequency are seen and the deviations are significant. The high-frequency deviations are not relevant as the first few modes used in these realisations do not carry much energy in these frequencies. The lower-frequencies deviate in phase and this illustrates the phase differences that the Grassmann modes and stretched time series have with respect to the POD modes from the 15 m s<sup>-1</sup> dataset. The phase difference between the original and the generated flow at the spectral peak of  $S_t = 0.34$  is around 18 degrees. When the generated flow is representative of the original flow this difference should be close to zero.

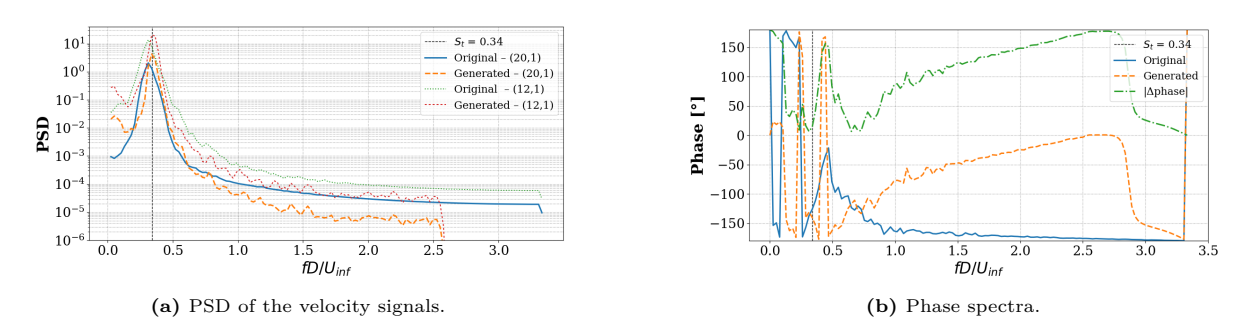
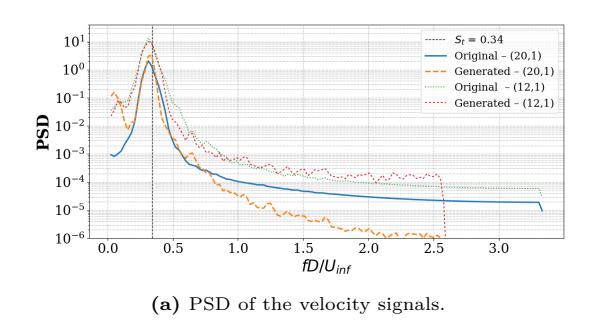


Figure 4.22: CSD comparison of six-mode POD and Grassmann mode realisations.

In figure 4.23 the CSD is again calculated for the first 6 modes. In this realisation the modes are rotated in phase such that MAC alignment is highest. The PSD of the modes are better aligned. The phase differences also improve slightly, but the misalignment remains. The phase difference at the spectral of 0.34 at peak occurs at 14 degrees.



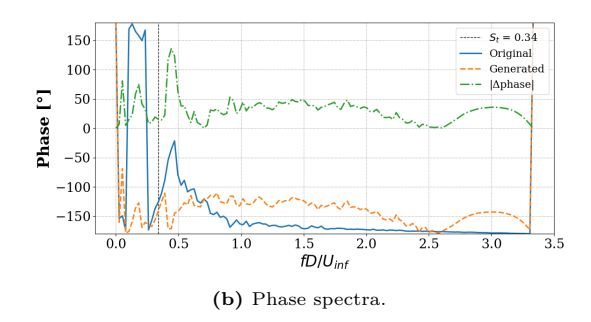


Figure 4.23: Improved CSD agreement after phase-optimised rotation of the Grassmann basis.

The calculation is again performed for only the first mode pair, the phase offset at the principal peak is around 1 degree. For a POD mode pair the phase difference should be near zero. The difference is acceptable and is believed to be a result of the time stretching adding numerical noise.

Despite optimally rotating the Grassmann modes, phase differences remain in the reconstructed flow. This is demonstrated with only the first three mode pairs. Additional modes are expected to worsen the misalignment. For a single mode pair the mode shape, PSD and phases of at the spectral peak can be matched with the Grassmann interpolation method and time stretching.

The first mode pair is seen to match up to 99% with the POD modes after phase alignment at the optimal geodesic step. The first mode pair is demonstrated to contain relatively little energy at these high Reynolds numbers. A reconstruction of the flow with only this mode pair will then result in relatively low velocity magnitudes. The singular values of this first mode pair may be increased to attain sufficiently high velocity magnitudes. Such a pared-down model may suffice for engineering purposes, but it remains deterministic and therefore cannot capture stochastic variability.

#### 4.4. Verification and Fit of Correlation Coefficient

The correlation coefficient as defined in section 3.3.1.3 defines the correlation of modes across different heights in the 3D correlated flow model. This section serves to find whether the curves shown in figure 3.6 and figure 3.7 are applicable as values for the correlation coefficient for the 3D model.

A global basis is formed from the two-dimensional flow slices along the heights of the cylinder. The basis is constructed by first concatenating the data series of the slices as by equation (4.17). Here  $A^{(z_i)}$  are the data matrices at heights  $z_1, z_2 \cdots z_5$ , M is the number of points in each slice and T the number of time steps.

$$A_{\text{combined}} = \left(A^{(z_1)}, \dots, A^{(z_5)}\right) \in \mathbb{R}^{M \times 5T} \tag{4.17}$$

The SVD of the combined matrix  $A_{\text{combined}}$  is taken as by equation (4.18). This gives the orthonormal spatial modes  $U_{\text{combined}} = [\mathbf{u}_1, \mathbf{u}_2, \dots]$ .

$$A_{\text{combined}} = U_{\text{combined}} \Sigma_{\text{combined}} V_{\text{combined}}^{\mathsf{T}}$$
 (4.18)

The choice to use a global basis is made to have an identical mode shape for each slice height. Using a global basis furthermore allows for the concatenation of more data that should allow for slightly more converged statistics. The first two global modes,  $\mathbf{u}_1$  and  $\mathbf{u}_2$ , can be seen in figure 4.24. These first modes correspond to the von Kármán street. This is the structure in the fluid that is associated with the oscillatory forcing on the cylinders.

The singular values global modes are plotted in figure 4.25. The energy thresholds illustrate that more modes are required to cover the data compared with the number of modes for an individual slice. Global modes are less efficient than individual slices [69] and therefore this is expected. The fraction of modes needed to attain the thresholds are at approximately 10% for the energy cut-off and 42% for the optimal SVHT cut-off while these are at 24% and 36% for the single slice.

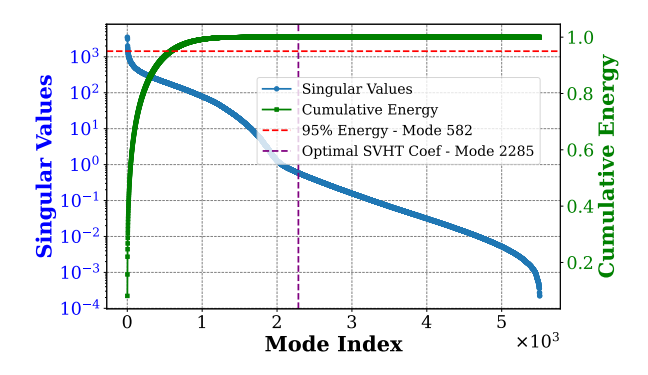


Figure 4.25: Singular values of global stationary cylinder basis.

#### 4.4.1. Verification of the Global POD Basis

In order to verify that the global modes extracted from the concatenated snapshot matrix are representative of the modes obtained from independent spanwise locations the Modal-Assurance Criterion (MAC) [73] in equation (4.19) is applied. Here  $U_{\text{combined}}$  is the global spatial mode matrix,  $U_{\text{slice},z}$  the spatial mode matrix of a slice at height z and  $P_z$  is a permutation matrix. The permutation matrix is chosen such that the sum of the diagonal entries of  $U_{\text{combined}}^{\mathsf{T}}U_{\text{slice},z}$  is maximized. This is done because some of the modes in the slices are observed to have been reordered compared to the global modes. A value of 1 indicates identical modes; values below about 0.8 mark noticeable deviations.

$$MAC_{ii}(z) = \left| \left( U_{\text{combined}}^{\mathsf{T}} U_{\text{slice},z} P_z \right)_{ii} \right|$$
(4.19)

The permutation matrix is chosen such that the sum of the diagonal entries of  $U_{\text{combined}}^{\mathsf{T}} U_{\text{slice},z}$  are maximized. It is formulated in equation (4.20). Here  $\mathcal{P}_k$  is the set of all  $k \times k$  permutation matrices.

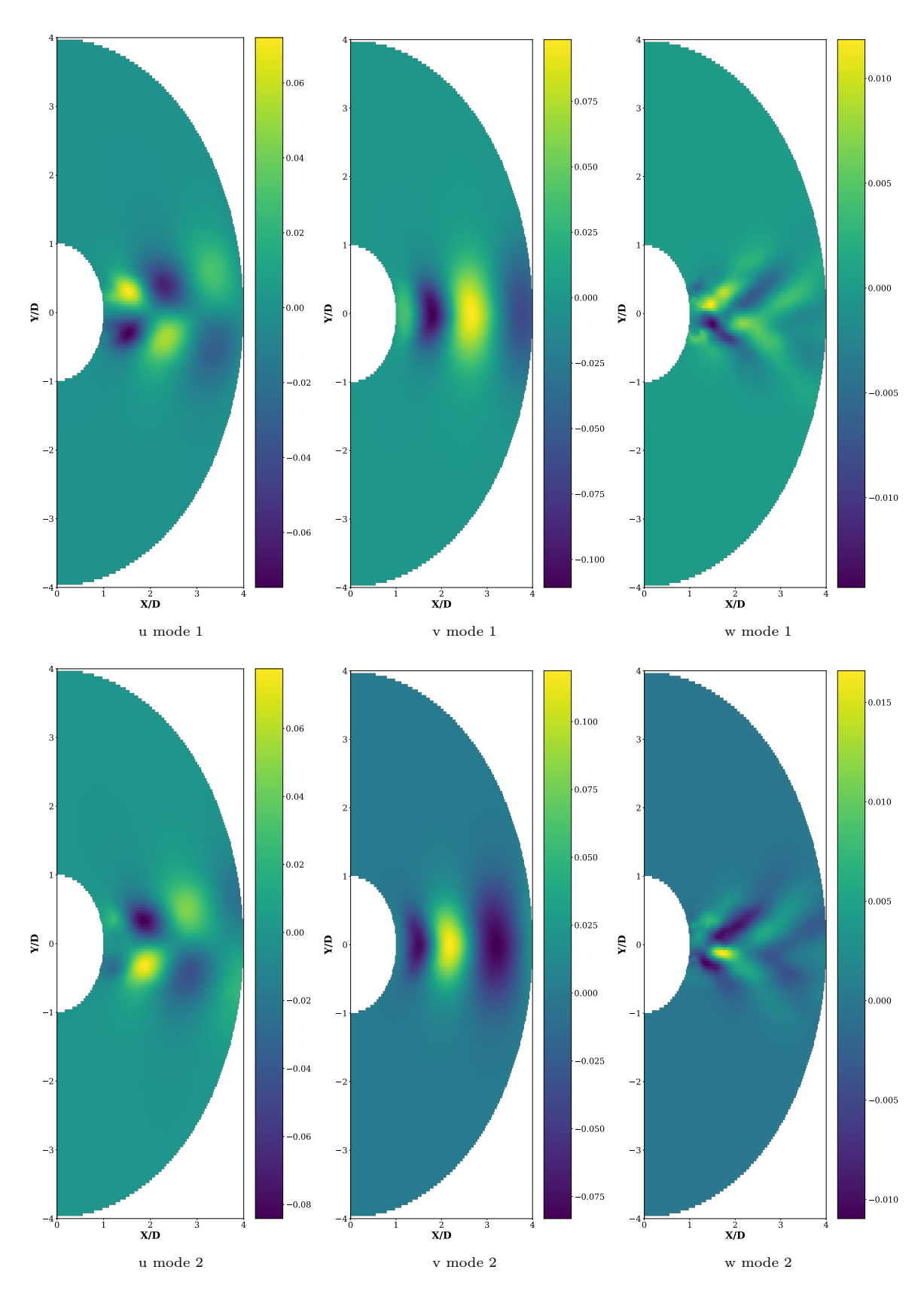


Figure 4.24: First two global POD modes of stationary cylinder. Illustrating the velocity components u, v, and w

$$P_{z} = \underset{P \in \mathcal{P}_{k}}{\operatorname{arg max}} \sum_{i=1}^{k} \left| \left( U_{\text{combined}}^{\mathsf{T}} U_{\text{slice,z}} P \right)_{ii} \right|$$
 (4.20)

This is done because the order of the modes of  $U_{\text{combined}}$  are not necessarily in the same order as the  $U_{\text{slice},z}$  modes. By applying the permutation matrix the modes are better matched.

Note that the MAC values quoted below are computed from the modes without performing the  $2 \times 2$  in-plane rotation that maximises pairwise overlap as is performed in section 4.3.4. Consequently, they represent a lower bound on the true similarity of the modes; a rotation could raise them. Because the spanwise-correlation analysis in section 4.4.2 depends on the leading mode pair, which already exceeds 0.9 across most slices, this is accepted as a conservative estimate here. A method for finding the highest MAC pairings that considers both rotation and the permutation matrix is illustrated in appendix C. Rotation-invariant sub-space metrics, such as the Grassmann geodesic distance [74] or the Asimov distance based on principal angles [75] exist. These metrics are however not further explored in this work.

Tables 4.1–4.3 list the diagonal MAC values for the three datasets considered: (a) a stationary cylinder, (b) an oscillating cylinder with 2a/D = 0.1, and (c) 2a/D = 0.2. All datasets are at a wind speed of 19 m s<sup>-1</sup>. The first two modes are well captured in every case, while the agreement deteriorates for higher modes, especially close to the no-penetration boundary at  $z/D \le 0.2$ . Figure 4.26 illustrates the first two modes at z = 0. Compared with the global modes shown earlier in figure 4.24 the difference becomes evident as the slice does not exhibit the von Kármán street in the first two modes.

**Table 4.1:** Diagonal entries of the  $MAC_{ii}$  for different slice heights, stationary cylinder.

Diagonal entry \ Slice	z/D = 0	z/D = 0.1	z/D = 0.2	z/D = 0.8	z/D = 1.6
$I_{11}$	0.70	0.77	0.97	0.91	0.96
$I_{22}$	0.68	0.83	0.95	0.91	0.96
$I_{33}$	0.94	0.68	0.96	0.72	0.81
$I_{44}$	0.68	0.90	0.91	0.70	0.81
$I_{55}$	0.54	0.70	0.83	0.61	0.33

Table 4.2: Diagonal entries of the MAC $_{ii}$  for different slice heights, oscillating cylinder with 2a/D = 0.1

Diagonal entry \ Slice	z/D = 0	z/D = 0.1	z/D = 0.2	z/D = 0.8	z/D = 1.6
$I_{11}$	0.94	0.97	0.98	0.96	0.95
$I_{22}$	0.88	0.96	0.97	0.94	0.92
$I_{33}$	0.39	0.91	0.90	0.89	0.88
$I_{44}$	0.85	0.85	0.83	0.89	0.63
$I_{55}$	0.53	0.87	0.89	0.79	0.75

**Table 4.3:** Diagonal entries of the MAC<sub>ii</sub> for different slice heights, oscillating cylinder with 2a/D = 0.2

Diagonal entry \ Slice	z/D = 0	z/D = 0.1	z/D = 0.2	z/D = 0.8	z/D = 1.6
$I_{11}$	0.96	0.99	0.98	0.98	0.99
$I_{22}$	0.91	0.98	0.97	0.96	0.97
$I_{33}$	0.44	0.92	0.75	0.66	0.77
$I_{44}$	0.45	0.86	0.69	0.70	0.88
$I_{55}$	0.71	0.75	0.64	0.51	0.74

The CFD simulation imposes a no penetration boundary condition with a  $w \equiv 0$  at the cylinder base (z/D=0). This results in purely two dimensional flow in this slice of the flow. Consequently, the lowest slices exhibit essentially two-dimensional flow and possess little energy in the w-component, which in turn reduces their overlap with the globally dominant, three-dimensional von Kármán street. This is illustrated in figure 4.26, where the first two slice modes clearly differ from the global counterparts shown in figure 4.24. Therefore the global basis performs worse at these slice heights.

Oscillating-cylinder cases show systematically larger MAC values for the primary modes. Here the imposed motion increases the standard deviation of the u- and v-fluctuations, strengthening the von Kármán street and thus enhancing the correlation with the global basis. The MAC may also be higher due to the imposed motion enforcing the phase of the mode pairs.

A global basis may be constructed solely from the upper slices (z/D=0.8 and 1.6) to remove the wall-induced mismatch. However, such a basis produces noticeably poorer reconstructions for the lower slices, which would compromise the spanwise correlation analysis presented in the next section. The trade-off is therefore accepted and revisited.

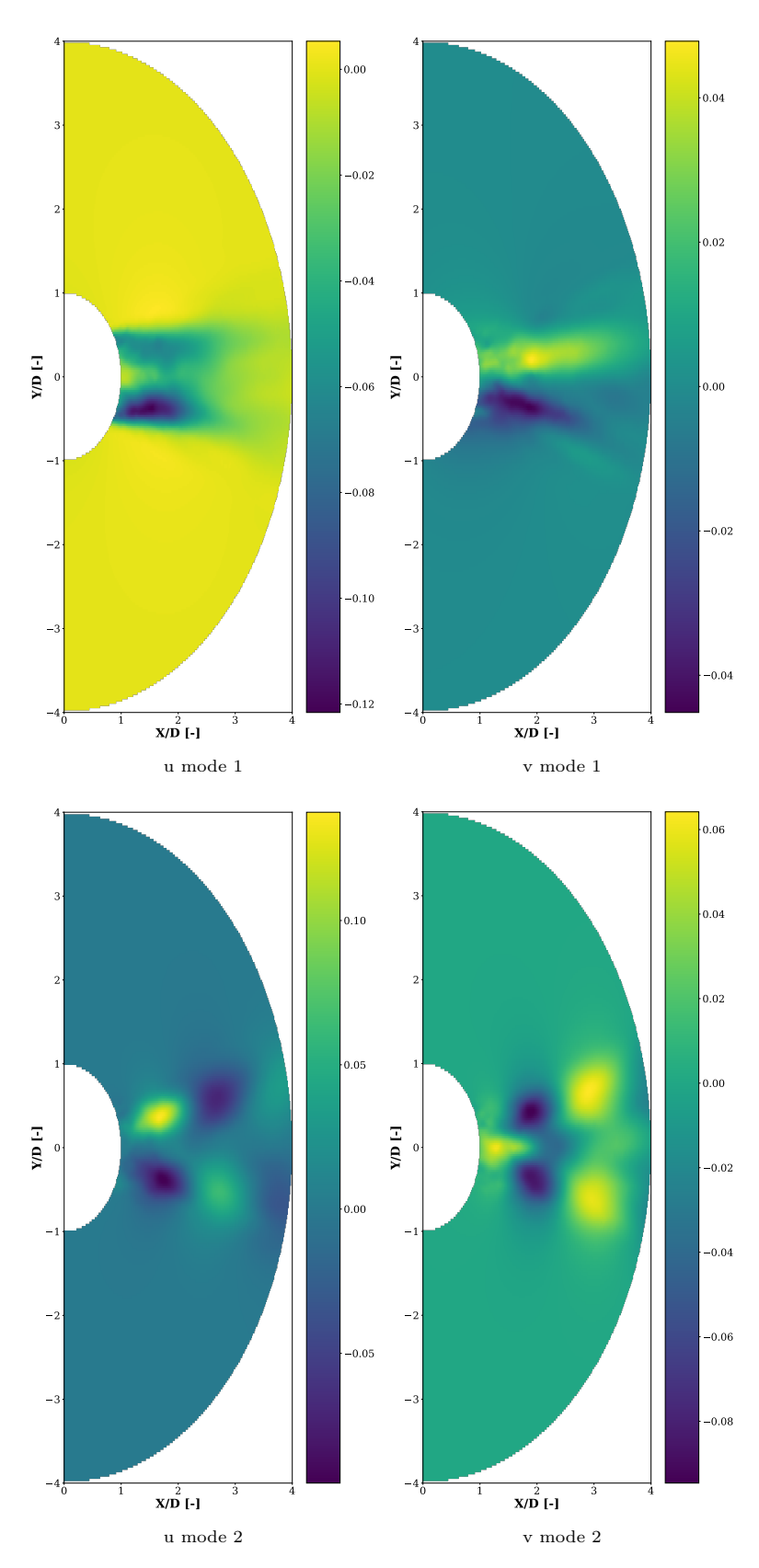


Figure 4.26: First two POD modes for slice at height z=0, stationary cylinder.

#### 4.4.2. Correlation of Modal Time Series

The global modes are projected onto the individual slices as in equation (4.21). Here the time series for mode i at a height z are denoted as  $\phi_{i,z}(t)$  and  $\mathbf{a}^{(z)}(t)$  is the t-th column of  $A^{(z)}$ . This results in time series for the global modes.

$$\phi_{i,z}(t) = \mathbf{u}_i^\mathsf{T} \mathbf{a}^{(z)}(t), \qquad t = 1, \dots, T$$
(4.21)

Given two heights  $z_1$  and  $z_2$ , the Pearson correlation of mode i is calculated as by equation (4.22). Here  $\bar{\phi}_{i,z} = T^{-1} \sum_{t=1}^{T} \phi_{i,z}(t)$  denotes the time-average of the modal coefficient  $\phi_{i,z}(t)$ .

$$r_{i}(z_{1}, z_{2}) = \frac{\sum_{t=1}^{T} (\phi_{i, z_{1}}(t) - \bar{\phi}_{i, z_{1}}) (\phi_{i, z_{2}}(t) - \bar{\phi}_{i, z_{2}})}{\sqrt{\sum_{t=1}^{T} (\phi_{i, z_{1}}(t) - \bar{\phi}_{i, z_{1}})^{2}} \sqrt{\sum_{t=1}^{T} (\phi_{i, z_{2}}(t) - \bar{\phi}_{i, z_{2}})^{2}}}$$

$$(4.22)$$

The curve  $r_i(z_1, z_2)$  as a function of mode number i quantifies how rapidly spatial coherence decays with modal rank and height separation  $\Delta z = |z_2 - z_1|$ . The resulting curves are illustrated in figure 4.27 for three different values of  $\Delta z/D$ . Inside figure 4.27a the correlations for the stationary cylinder are illustrated while figure 4.27b and figure 4.27c illustrate the correlations coefficients of the oscillating cylinders. All graphs are at a wind speed of 19 m s<sup>-1</sup>. The 3D cylinder simulations consist of a stationary cylinder and two cylinders that oscillate with an amplitude 2a/D = 0.1 and 2a/D = 0.2 where a = 0.25 m and a = 0.50 m respectively.

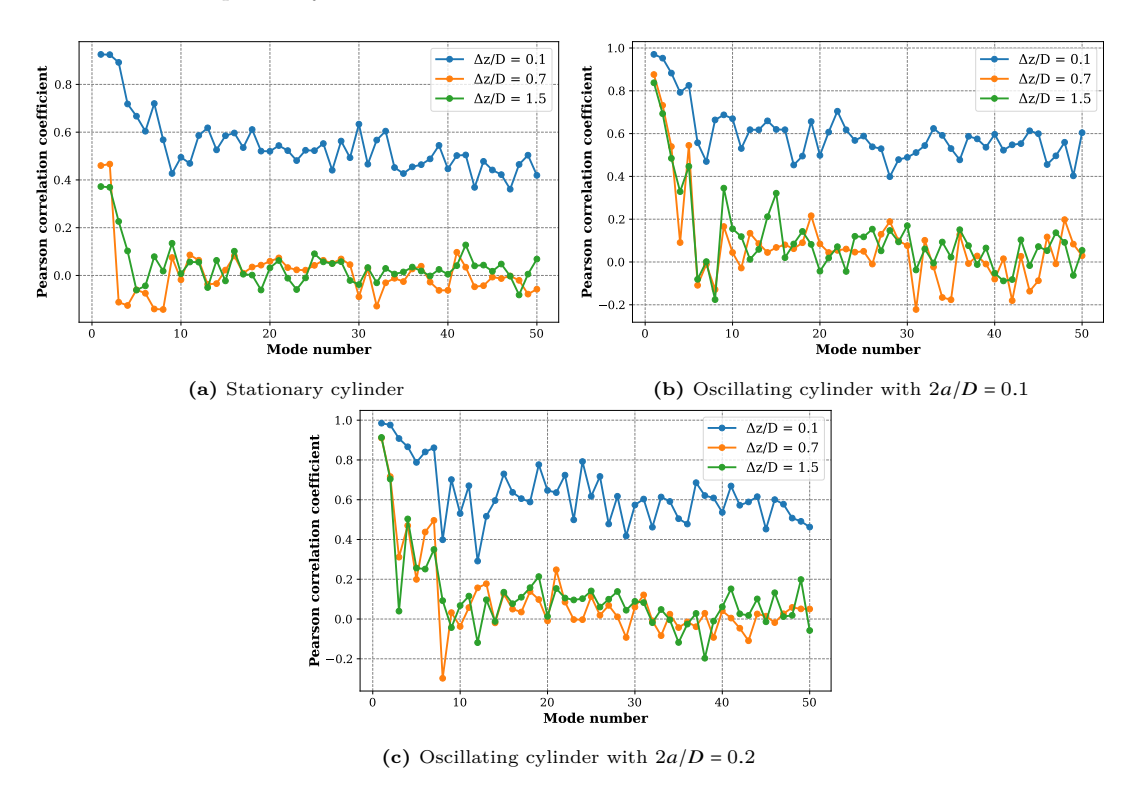


Figure 4.27: Correlation coefficient of global POD modes for stationary and oscillating cylinders at 19 m s<sup>-1</sup>.

From figure 4.27 it becomes evident that the first few modes carry the largest correlation across heights while the remaining modes rapidly become decorrelated. Furthermore the oscillating cylinder has a higher correlation coefficient for the first few modes across heights. This is in line with the literature on correlation of forcing on cylinders [17]. High correlations on the forcing on cylinders are similarly seen

in DES literature at a slightly higher Reynolds number of  $8 \times 10^6$  for a cylinder with an aspect ratio of 2 [23].

The graphs also illustrate that the statistics of the flow is not fully converged. This is clear from the distributions not decaying smoothly and the often negative values for the correlation that have no physical meaning as it would suggest that structures at a different heights have anti-phase behaviour.

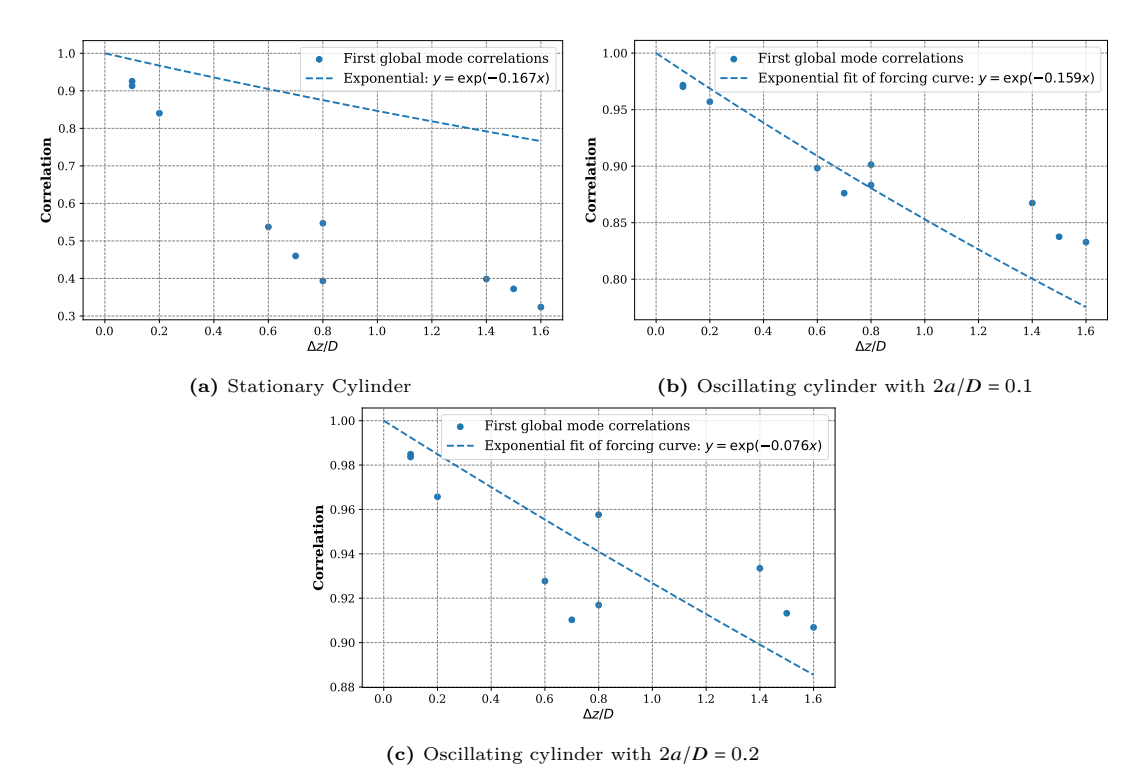


Figure 4.28: Correlation coefficient of first mode alongside exponential fit of forcing correlation curve of stationary and oscillating cylinders at  $19~{\rm m\,s^{-1}}$ .

In figure 4.28a, the correlation coefficient of the first mode—calculated from equation (4.22)—is shown alongside an exponential decay with a correlation length of L/D = 1.2. For the oscillating cylinders, shown in figure 4.28b and figure 4.28c, the correlation coefficients are plotted alongside fitted curves derived from the forcing correlations in figure 3.6. The first mode corresponds to the von Kármán street and is therefore the spatial structure that is associated with the oscillatory forcing on the cylinder.

It is observed that the correlation coefficients for the oscillating cases align reasonably well with the exponential fits, whereas the stationary case shows a lower correlation. This discrepancy is attributed to two main factors. First, it is possible that the general trend of decreasing correlation length with increasing Reynolds number persists, and that the CFD simulation accurately captures this behaviour. Second, the reduced correlation may result from the global basis performing worse on the dataset.

This second point is well illustrated by the two points at  $\Delta z/D = 0.8$ . These points correspond to the correlation of the slice pair at heights z = 0, z = 0.8 and the slice pair z = 0.8 and z = 1.6. The correlation between slice z = 0 and z = 0.8 is lower than that of the other pair. The no-penetration boundary constraint at z = 0 makes the flow in this slice less similar to the flow of z = 0.8 than the flow at z = 1.6, thereby the correlation of the modal time series is reduced.

The data range is also limited due to the limitations of the 3D cylinder CFD simulations. Simulations of longer cylinders are desired to confirm if the correlation follows along longer length scales as is suggested from experiments. Longer cylinder simulation with slices taken further away from the boundary constraints will result in a global basis that aligns better with individual slices. The subsequent correlations of the time series can then be investigated better.

#### 4.4.3. Fitting of Modal Correlation Coefficient

The correlation coefficients of the cylinders illustrated in figure 4.27 are fitted as a function of length scale and mode index.

Given the Pearson correlation coefficient  $C(k, \Delta z)$  between the temporal coefficients of mode k at two vertical positions whose separation is  $\Delta z$ , two functional forms that satisfy the normalisation condition of equation (4.23) are investigated. Namely, the multiplicative stretched exponential (MSE) as per equation (4.24) and stretched power law (SPL) as per equation (4.25). Here  $x = \Delta z/D$  is the dimensionless separation, with D = 5 m the reference diameter of the cylinder.

$$C(k,0) = 1 \qquad \forall k \in \mathbb{N} \tag{4.23}$$

$$C_{\text{MSE}}(k, x) = \exp[-a k^{\beta} x^{\alpha}]$$
(4.24)

$$C_{\text{SPL}}(k,x) = \left(1 + a k^{\beta} x^{\alpha}\right)^{-p} \tag{4.25}$$

The parameters a>0,  $\alpha>0$ ,  $\beta>0$ , p>0 (SPL only) control, respectively, the overall decay amplitude, the spatial–decay exponent, the mode-number exponent, and—only for the SPL model—the tail heaviness.

### 4.4.4. Fitting Procedure

For every admissible pair of mode number k and dimensionless separation  $x = \Delta z/D$  the Pearson correlation C(k,x) is calculated. Non–positive values are discarded before the regression.

The model parameters  $\theta = (a, \alpha, \beta)$  for the MSE equation (4.24) and  $\theta = (a, \alpha, \beta, p)$  for the SPL equation (4.25) are obtained with the scipy.optimize.curve\_fit [76] routine, which performs a non-linear least-squares minimisation of the residual sum as in equation (4.26). Here  $C_i$  are the Pearson correlation coefficients that are being fit. The fit is subject to the positivity constraints  $a, \alpha, \beta, p > 0$ .

$$S(\boldsymbol{\theta}) = \sum_{i=1}^{M} \left[ C_i - C_{\text{model}}(k_i, x_i; \boldsymbol{\theta}) \right]^2$$
 (4.26)

The results of the fitting for the oscillating cylinder with 2a/D = 0.2 can be seen in figure 4.29. It may be seen that the fits perform increasingly well with increasing of the  $\Delta z$ , as both models tend to underestimate the correlations at smaller separations, particularly for the majority of modes shown in figure 4.29a. Overall, the SPL model provides a marginally better fit at low mode numbers. This is especially desirable, as the lower modes contain the majority of the flow energy and should therefore be prioritised in the fitting. The corresponding model parameters are listed in table 4.4

The fittings of the oscillating cylinder with 2a/D = 0.1 and the stationary cylinder alongside their fitting parameters may be seen in appendix E.

Table 4.4: Optimised parameters for the two-variable decay models.

Model	а	α	β	p
MSE	0.461	0.507	0.494	-
$\operatorname{SPL}$	0.536	1.58	2.28	0.366

**Mode-dependent coherence.** The proposed 3D model as proposed in section 3.3 through the analysis in this section warrants the modification that the correlation coefficient is not simply a single coefficient dependent on vertical distance, but also on the mode number k. The correlation between two distinct slices of the flow i and j (with  $i \neq j$ ) is expanded from the definition earlier shown in equation (3.22).

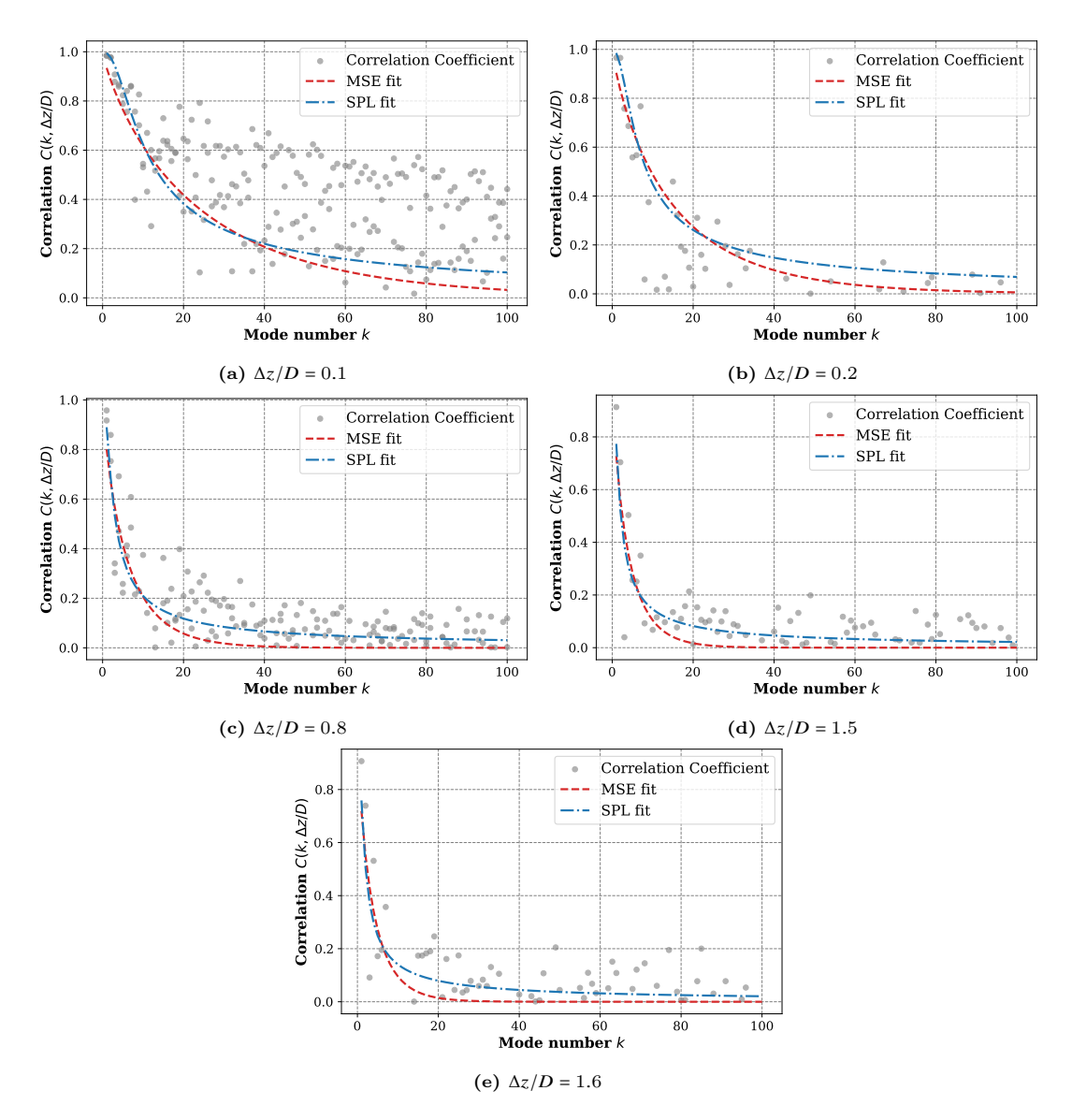


Figure 4.29: Correlation coefficient fitting using MSE and SPL curves of oscillating cylinder with 2a/D = 0.2.

The modified cross spectral block is formulated in equation (4.27). This modification simply lowers the coherence to the empirically observed value.

$$S_{ij}^{(k)}(f) = C(k, \Delta z_{ij}) X_k^{(i)}(f) X_k^{(j)*}(f), \qquad i \neq j$$
(4.27)

In equation (4.27)  $C(k, \Delta z) \in [0, 1]$  is the empirical coherence surface fitted using an SPL or MSE curve with the SPL being the preferred fit for its better performance for low order modes.

The fittings presented here in this section are empirical fits of the observed data from the CFD simulations. In principle any modal correlation can be enforced by chosen functions for  $C(k, \Delta z)$ . These correlations may then be chosen from measured data, or tuned depending on the conditions. Expansions may include more than just oscillation amplitude. Considerations can be made for turbulence intensity and wind shear. Their influence has been illustrated to reduce correlation along span [16, 18].

# Stream Function and Toroidal-poloidal Decomposition Modal Fitting

This chapter describes a method to fit POD spatial modes with a divergence-free, no-slip stream-function basis. First, in section 5.1, the von Kármán vortex street is shown to be essentially two-dimensional, so only the toroidal (in-plane) potential is retained. Next, in section 5.2, a Joukowski transform maps the exterior of the cylinder to a simple plane where the cylinder wall becomes a straight line. In that transformed domain, integrated Laguerre functions (downstream) and Gaussian–Hermite functions (cross-stream) are chosen in section 5.2.1 so that  $\psi = 0$  and  $\partial_{\xi}\psi = 0$  on the wall, enforcing no-slip automatically. A weighted constraint is introduced in section 5.2.1.1 to remove one coefficient per Hermite column and eliminate normal velocity. Finally, the fitted coefficients are mapped back to physical space via the Jacobian, producing divergence-free, no-slip modes for use in a stochastic reduced-order model. The resulting fitting errors are then analyzed in section 5.3.

# 5.1. Quasi-2D Modal Fitting Using Toroidal Stream Function Basis

Any solenoidal vector field  $\mathbf{V}(x,y,z) = (u,v,w)^{\mathsf{T}}$  can be decomposed uniquely into a toroidal part and a poloidal part [77]. The decomposition can be seen in equation (5.1). Here T and P are scalar potentials and  $\hat{\mathbf{e}}_z$  is a chosen symmetry axis. Both components are divergence-free by construction:  $\nabla \cdot \nabla \times (\cdot) = 0 = \nabla \cdot \nabla \times \nabla (\cdot)$ .

$$V(x, y, z) = \underbrace{\nabla \times (T(x) \,\hat{\mathbf{e}}_z)}_{\text{toroidal} = \mathbf{u}^t} + \underbrace{\nabla \times \nabla (P(x) \,\hat{\mathbf{e}}_z)}_{\text{poloidal} = \mathbf{u}^P}$$
(5.1)

In this study, flow data are confined to two-dimensional measurement planes around cylinders at high Reynolds number. Such flows are dominated by the von Kármán vortex street, a coherent, periodic array of spanwise vortices shed alternately from either side of the cylinder. Experimental and numerical investigations [78, 79] have shown that these structures are predominantly planar, with in-plane velocities (u, v) carrying the bulk of the kinetic energy and possessing high spatial coherence. In comparison, the vertical velocity w and the associated streamwise vortices carry a far smaller energy fraction [80].

Proper orthogonal decomposition (POD) of the measured velocity snapshots as shown in section 4.1 confirms that the dominant energetic structures correspond to the classical von Kármán vortex street. The first few modes exhibit the familiar alternating circulation cells and capture the vast majority of the kinetic energy contained in the horizontal velocity components. By contrast, the associated w-components contribute only a small fraction of the total energy and display markedly weaker spatial coherence. Their amplitudes are an order of magnitude lower and their patterns lack the well-organised vortical cores visible in the leading in-plane modes.

This strong scale separation between the large, energetic in-plane vortices and the smaller, less organised out-of-plane structures motivates a simplification: in the measurement plane only the toroidal scalar potential T is approximated, thereby neglecting the vertical velocity component w altogether. The vertical coherence of the von Kármán street is sufficiently long that this quasi-2D model remains accurate for reconstructing the dominant dynamics [78, 80]. This can also be concluded from the correlation of the forcing on the cylinder as is illustrated in section 3.3.1.3.

The velocity field is then given by the planar curl as per equation (5.2).

$$V(x, y, z) = \nabla \times (T(x, y) \hat{\boldsymbol{e}}_z) = \left(\frac{\partial T}{\partial y}, -\frac{\partial T}{\partial x}, 0\right)^{\mathsf{T}}$$
 (5.2)

The vertical component w in equation (5.2) vanishes, ensuring that the model captures purely in-plane, divergence-free motion. This toroidal formulation is equivalent to a stream function. Any remaining energy is formally contained in the poloidal field  $\boldsymbol{u}^P$ . Consequently, the following work will focus on recovering the dominant von Kármán street and other large-energy in-plane features by performing a fitting to the earlier found POD modes. This proposed model can later be augmented with P once volumetric data become available.

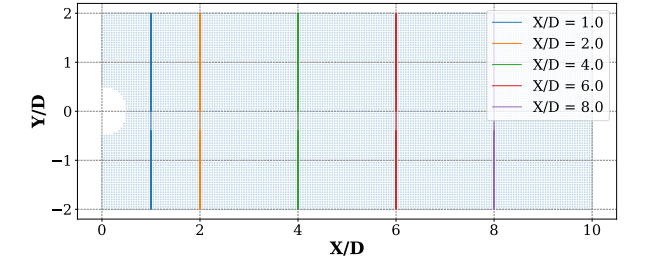
# 5.2. Basis Choices and the Joukowski Transform

Proper orthogonal decomposition (POD) is purely a data-based method. The resulting spatial modes and the reduced order model obtained from the method do not necessarily fulfil physical constraints such as mass-conservation and the no-slip condition on the cylinder wall. Choosing physically informed basis can reintroduce some of the desired physics.

The POD analysis from section 4.1 demonstrates that the coherent structures decay smoothly in the downstream far field. The rectangular domain contains the cylinder. Representing such a domain directly in Cartesian coordinates is inconvenient: the presence of the solid body leaves an annular hole that must be excluded from every quadrature rule and from every global basis expansion. A classical remedy is to map the punctured plane onto a simply-connected domain with a conformal transformation. For a circular cylinder the canonical choice is the Joukowski map [81]. The formulation may be seen in equation (5.3) where the scaling R = 2.5 m matches the cylinder radius in the simulation.

$$w = f(\zeta) = \zeta - \frac{1}{\zeta}, \qquad \zeta = \frac{x + iy}{R}$$
 (5.3)

Under f the whole exterior of the cylinder  $(|\zeta| > 1)$  is sent to the full  $(\xi, \eta) = (\Re w, \Im w)$  plane. The unit circle  $|\zeta| = 1$  collapses to the vertical slit  $w = e^{i\theta} - e^{-i\theta} = 2i\sin\theta \implies \xi = 0$ ,  $\eta \in [-2, 2]$ , this way the cylinder wall becomes the straight segment  $\xi = 0$  from  $\eta = -2$  to  $\eta = 2$  [81]. Approaching that segment from the right half-plane  $(\xi \to 0^+)$  or the left half-plane  $(\xi \to 0^-)$  corresponds, respectively, to coming from the exterior or the interior of the circle; the mapping is therefore one-to-one everywhere except on the slit, where it is two-to-one. The original and transformed coordinates may be seen in figure 5.1 and figure 5.2 respectively. The far field deforms little while the points near the cylinder experience the largest deformations.



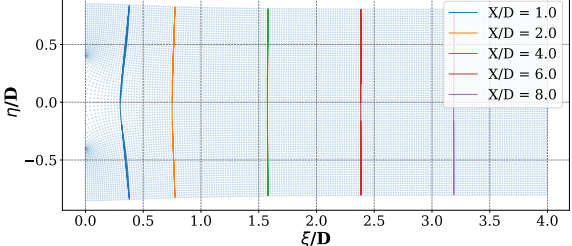


Figure 5.1: Cartesian coordinates (physical plane).

**Figure 5.2:** After Joukowski mapping  $(\xi, \eta)$  plane.

The Joukowski map is analytic except at the isolated point  $\zeta = 0$  (where  $1/\zeta$  has a pole) and at  $\zeta = \pm i$  (where  $f'(\zeta) = 1 + \zeta^{-2}$  vanishes). Away from those singularities it is conformal, preserving angles and

local orientation and, crucially, leaving harmonic functions harmonic. Consequently, an expansion that is incompressible in the Joukowski domain remains incompressible after mapping back to Cartesian coordinates.

In figure 5.3, the first mode is shown after applying the Joukowski transform. The cylinder gap disappears in the transformed plane. The resulting deformation of the transformation is also most clearly seen in this region of the cylinder. In the far field the deformation is minimal.

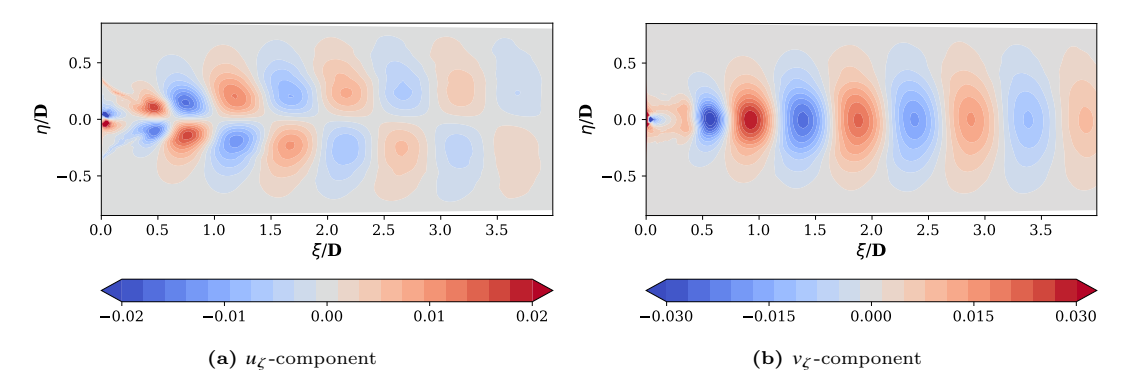


Figure 5.3: Joukowski transformation of first spatial mode

#### 5.2.1. Choice of Modal Basis in the $\zeta$ -plane

The POD spatial modes are represented using a toroidal stream function basis. The POD basis are fitted after a Joukowski map is applied. The coordinates and the respective velocity components u and v are converted to the velocity components  $u_{\zeta}$  and  $v_{\zeta}$  in the  $\zeta$ -plane respectively. The points on the cylinder edge are mapped to the straight line segment from  $\eta = -2$  to  $\eta = 2$  at  $\xi = 0$  in the  $\zeta$  plane. A basis expansion where the function value is 0 at  $\xi = 0$  enforces the no-slip condition by construction. The kinematic no-slip condition therefore requires that both velocity components satisfy  $u_{\zeta}(\xi=0,\eta)=0$  and  $v_{\zeta}(\xi=0,\eta)=0, \forall \eta\in (-2,2)$ . Writing the flow in terms of a stream function  $u_{\zeta}=\partial_{\eta}\psi, v_{\zeta}=-\partial_{\xi}\psi$ , the two constraints are as implemented through the boundary condition in equation (B.C. $\psi$ ). Note that the boundary condition  $\psi(0,\eta)=0$  is stronger than necessary as it enforces the  $u_{\zeta}$  component to be zero on the entire axis  $\eta=0$ , rather than just on the segment  $\eta\in (-2,2)$ . However, since the mean flow is subtracted and only small fluctuations occur near this boundary, few modes carry significant energy in this region. The stricter condition is therefore not expected to substantially degrade the quality of the fits compared to a constraint applied solely on the line segment  $\eta\in (-2,2)$ .

$$\psi(0,\eta) = 0, \qquad \partial_{\xi}\psi(0,\eta) = 0$$
 (B.C. $\psi$ )

The POD spatial modes are expressed in the  $\zeta$ -plane using tensor-product basis functions of the form of equation (5.4). Here  $B_n(\xi)$  and  $B_m(\eta)$  are arbitrary basis functions depending only on the  $\xi$  and  $\eta$  coordinates respectively. Note that the mean is subtracted from the flow. Therefore the far field constraint that the flow should equal the free stream velocity is automatically fulfilled.

$$T_{N_x,N_y}(\xi,\eta) = \sum_{n=0}^{N_x} \sum_{m=0}^{N_y} a_{kn} \underbrace{B_n(\xi)}_{\text{streamwise cross-stream}} \underbrace{B_m(\eta)}_{\text{streamwise cross-stream}}$$
(5.4)

The coefficients  $a_{nm}$  are obtained by solving the least-squares problem in equation (5.5). All fitting is therefore carried out in the  $\zeta$ -plane and the true Cartesian velocity components are only recovered after the fitting.

$$\min_{a_{nm}} \left\| (u_{\zeta}, v_{\zeta}) - \nabla \times \left[ T_{N_x, N_y} \, \hat{\boldsymbol{e}}_z \right]_{(\xi, \eta)} \right\|_2^2 \tag{5.5}$$

The functions  $B_n(\xi)$  are responsible for the streamwise representation while  $B_m(\eta)$  resolve the cross–stream structure. The two families of functions are chosen so that (i) the no–slip boundary condition at the cylinder surface is satisfied, (ii) truncations remain divergence–free, and (iii) only a modest number of modes is required to approximate the velocity field in both the near and the far wake. The third point here also has the benefit of reducing the data requirements for representing the field.

The basis functions tested are:

- $\Lambda_k(\xi) = \frac{1}{\sqrt{\Gamma(k+1)}} \int_0^{\xi} L_k(s) e^{-s/2} ds$  the integrated Laguerre functions.
- $\chi_n(\eta)$  the Gaussian–Hermite functions.

The integrated Laguerre function are defined in equation (5.6) while the Hermite basis functions are shown as in equation (5.7). Here  $L_k$  is the probabilists' Laguerre polynomial [82] and  $\Gamma$  is the gamma function. The choice for a Hermite basis ensures mass conservation through each vertical slice. A proof of this is provided in appendix D. The choice of Hermite basis function is furthermore a logical choice as these functions generally provide accurate fits for diffusion problems [83] and should therefore provide an accurate fit for the far field. Because every  $L_k(0) = 1$  the family obeys  $\Lambda_k(0) = 0$ ,  $\Lambda'_k(0) = \frac{1}{\sqrt{\Gamma(k+1)}}$ , the stream function therefore itself vanishes on the cylinder wall. Furthermore, the velocities decay exponentially downstream, just like the true wake behind a cylinder.

$$\Lambda_k(\xi) = \frac{1}{\sqrt{\Gamma(k+1)}} \int_0^{\xi} L_k(s) e^{-s/2} ds, \qquad k = 0, 1, \dots$$
 (5.6a)

$$L_k(\xi) = \sum_{m=0}^k \binom{k}{m} \frac{(-\xi)^m}{m!}, \qquad k = 0, 1, \dots$$
 (5.6b)

$$\chi_n(\eta) = \frac{H_n(\eta/\eta_0)}{\pi^{1/4} \sqrt{2^n n! \, \eta_0}} e^{-\eta^2/(2\eta_0^2)} \quad (n = 0, 1, \dots)$$
 (5.7)

The corresponding velocity components that are fitted follow from the planar curl,  $u_{\zeta} = \partial_{\eta} T$ ,  $v_{\zeta} = -\partial_{\xi} T$ . The relation between the fitted pair  $(u_{\zeta}, v_{\zeta})$  and the physical velocity components (u, v) is obtained from the Jacobian of the Joukowski map as per equation (5.8).

$$\mathbf{J}(x,y) = \frac{1}{R} \begin{pmatrix} \Re(1+\zeta^{-2}) & -\Im(1+\zeta^{-2}) \\ \Im(1+\zeta^{-2}) & \Re(1+\zeta^{-2}) \end{pmatrix}, \qquad \zeta = \frac{x+iy}{R}$$
 (5.8)

The Jacobian of equation (5.8) provides  $(u, v)^{\mathsf{T}} = \mathbf{J}^{-1}(x, y) (u_{\zeta}, v_{\zeta})^{\mathsf{T}}$ . The velocity components  $u_{\zeta}$  and  $v_{\zeta}$  are therefore first fit in the Joukowski plane and subsequently converted back to the Cartesian velocity components u and v.

#### 5.2.1.1. Enforcing the No-slip Condition

Each integrated Laguerre function satisfies  $\Lambda_k(0) = 0$ , therefore the tensor product in equation (5.4) automatically gives  $\psi(0,\eta) = 0$  for every  $\eta$ , which in turn forces the tangential velocity component  $u_{\zeta} = \partial_{\eta} \psi$  to vanish on the cylinder wall. The wall–normal component involves the derivative  $\partial_{\xi} \psi$ . Evaluating the expansion at  $\xi = 0$  yields equation (5.9). Here  $W_n$  is the linear relation that is required to equal 0 as per equation (5.10). The normal velocity disappears provided equation (5.10) is met.

$$v_{\zeta}(0,\eta) = -\sum_{n=0}^{N_{y}} \underbrace{\left(\sum_{k=0}^{N_{x}} \frac{a_{kn}}{\sqrt{\Gamma(k+1)}}\right)}_{=:W_{n}} \chi_{n}(\eta)$$
(5.9)

$$W_n = \sum_{k=0}^{N_x} \frac{a_{kn}}{\sqrt{\Gamma(k+1)}} = 0, \qquad n = 0, \dots, N_y$$
 (5.10)

In order to meet the constraint one coefficient per Hermite column is eliminated. This is chosen to be the highest-order Laguerre coefficient. Because each mode enters  $v_{\zeta}(0,\eta)$  multiplied by  $\Lambda'_{k}(0) = 1/\sqrt{\Gamma(k+1)}$ , the cancellation must act on the weighted coefficients  $a_{kn}/\sqrt{\Gamma(k+1)}$ . Setting the weighted sum to zero and solving for  $a_{N_x,n}$  gives equation (5.11).

$$a_{N_x,n} = -\sum_{k=0}^{N_x - 1} \frac{\sqrt{\Gamma(N_x + 1)}}{\sqrt{\Gamma(k + 1)}} a_{kn}, \qquad n = 0, \dots, N_y$$
 (5.11)

Substituting equation (5.11) into the design matrix removes one column per column-block and therefore reduces the number of unknowns from  $(N_x+1)(N_v+1)$  to  $N_x(N_v+1)$ .

#### 5.2.1.2. Design Matrix with and without Constraint

For each pair of polynomial indices (k, n) the discrete velocity samples of an integrated Laguerre-Hermite basis populate two columns, as shown in equation (5.12), for each  $k = 0, \ldots, N_X$  and  $n = 0, \ldots, N_Y$ . These columns are valid for  $k = 0, ..., N_x$ .

$$\mathbf{d}_{k,n}^{(u_{\zeta})} = \Lambda_k \, \chi_n' \tag{5.12a}$$

$$\mathbf{d}_{k,n}^{(\nu_{\zeta})} = -\Lambda_k' \chi_n \tag{5.12b}$$

In equation (5.12)  $\Lambda_k = \Lambda_k(\xi)$  and  $\chi_n = \chi_n(\eta)$  are evaluated at the  $N_s$  measurement points. Equation (5.12) therefore lists the full set of columns before the weighted column-sum constraint of equation (5.11) is enforced.

Embedding the constraint proceeds by eliminating the highest-order Laguerre coefficient in each Hermite column and rewriting it with the lower-order ones through (5.11). Substituting this relation gives the shifted columns as in equation (5.14). Here  $k=0,\ldots,N_x-1$ .

$$\widetilde{\mathbf{d}}_{k,n}^{(u_{\xi})} = (\Lambda_k - r_k \Lambda_{N_x}) \chi_n',$$

$$\widetilde{\mathbf{d}}_{k,n}^{(v_{\xi})} = -(\Lambda_k' - r_k \Lambda_{N_x}') \chi_n$$
(5.13)

$$\widetilde{\mathbf{d}}_{k,n}^{(v_{\zeta})} = -\left(\Lambda_{k}' - r_{k}\Lambda_{N_{x}}'\right)\chi_{n} \tag{5.14}$$

The weight  $r_k$  defined in equation (5.15) originates from the derivative  $\Lambda'_{N_r}(0)$ .

$$r_k = \sqrt{\frac{\Gamma(N_x + 1)}{\Gamma(k + 1)}} \tag{5.15}$$

Collecting all Hermite indices  $n=0\dots N_y$  yields the block matrices of for the  $u_\zeta$ - and  $v_\zeta$ -components in equation (5.16).

$$\widetilde{\mathbf{D}}_{k}^{(u_{\zeta})} = \left[\widetilde{\mathbf{d}}_{k,0}^{(u_{\zeta})} | \dots | \widetilde{\mathbf{d}}_{k,N_{v}}^{(u_{\zeta})} \right], \tag{5.16a}$$

$$\widetilde{\mathbf{D}}_{k}^{(\nu_{\zeta})} = \left[\widetilde{\mathbf{d}}_{k,0}^{(\nu_{\zeta})} | \dots | \widetilde{\mathbf{d}}_{k,N_{\sigma}}^{(\nu_{\zeta})} \right]$$
(5.16b)

Stacking first all  $u_{\zeta}$ -components and then all  $v_{\zeta}$ -components constructs the reduced design matrix of equation (5.17).

$$\widetilde{\mathbf{M}} = \left[ \underbrace{\widetilde{\mathbf{D}}_{0}^{(u_{\zeta})} | \dots | \widetilde{\mathbf{D}}_{N_{x}-1}^{(u_{\zeta})}}_{u_{\zeta}-\text{rows}} | \underbrace{\widetilde{\mathbf{D}}_{0}^{(v_{\zeta})} | \dots | \widetilde{\mathbf{D}}_{N_{x}-1}^{(v_{\zeta})}}_{v_{\zeta}-\text{rows}} \right] \in \mathbb{R}^{2N_{s} \times N_{x}(N_{y}+1)}$$
(5.17)

Given the  $\widetilde{M}$  the least-squares system may be defined as in equation (5.18). Here  $\widetilde{\mathbf{a}} \in \mathbb{R}^{N_x(N_y+1)}$  are the desired coefficients to be solved and  $u_{\zeta}^{\text{data}}$  are the stacked  $u_{\zeta}$  and  $v_{\zeta}$  velocity components in the  $\zeta$ -plane coordinates.

$$\min_{\widetilde{\mathbf{a}}} \left\| \widetilde{\mathbf{M}} \widetilde{\mathbf{a}} - \mathbf{u}_{\zeta}^{\text{data}} \right\|_{2}^{2}$$
(5.18)

The system is solved via a QR factorisation using the python scipy.linalg.lstsq library [76]. This enforces the no-slip condition by construction.

#### 5.3. Error Quantification of Fits

In order to assess how well the Integrated Laguerre–Hermite basis captures the true spatial modes, a local pointwise error and a global root-mean-square error (RMSE) for each fit are defined. These error measures serve two purposes: (i) to evaluate how closely each fitted mode reproduces the original velocity field in Cartesian coordinates, and (ii) to gauge how fit inaccuracies might propagate through the stochastic reduced-order model (SROM) described in section 3.2.2.

#### 5.3.1. Local Percentage Speed Error

In figure 5.4, an example of the second spatial mode alongside its fitting can be seen. This fit is a fitting with  $N_x = 20$ ,  $N_y = 20$  and  $\eta_0 = 4$ . From visual inspection slight differences can be seen in the near field of the cylinder. The observed differences are quantified with a local percentage speed error.

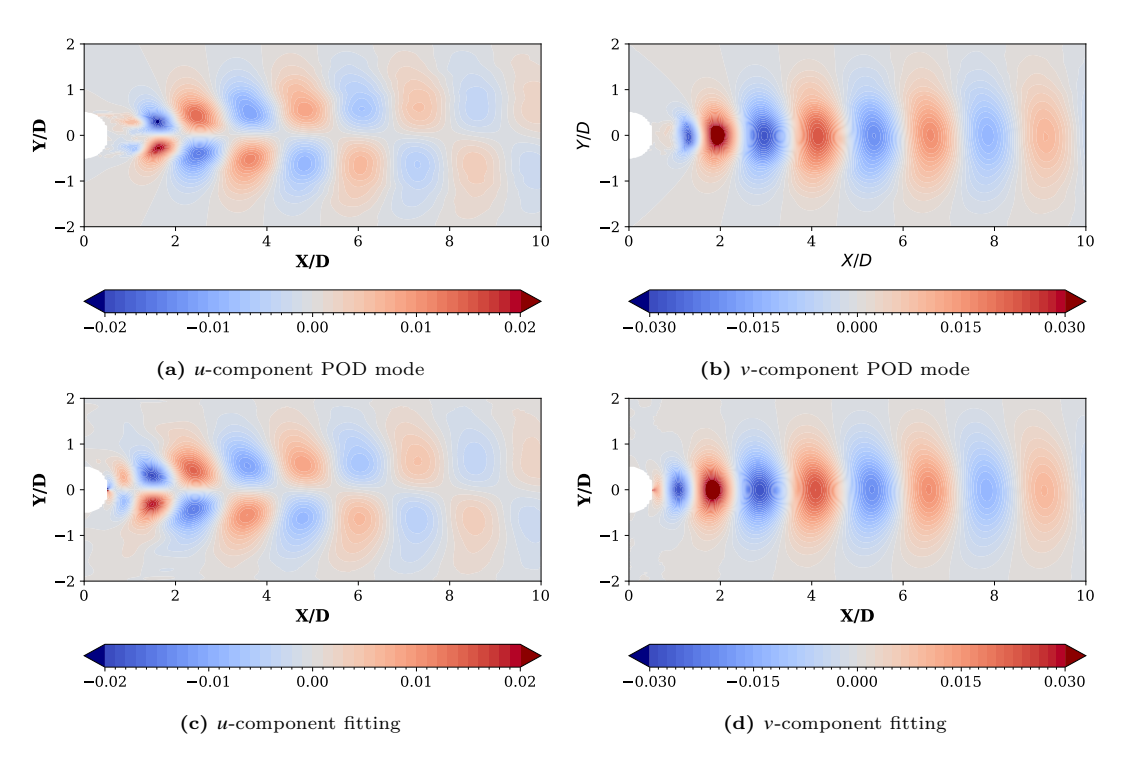


Figure 5.4: Spatial mode 2 from POD (a,b) and its Integrated Laguerre–Hermite fit (c,d), using  $N_x = 20$ ,  $N_y = 20$ ,  $\eta_0 = 4$ .

For a given spatial mode, let  $(u_i, v_i)$  denote the original Cartesian velocity components at point i, and  $(u_i^f, v_i^f)$  the corresponding fitted values obtained after mapping back from the Joukowski plane. A local

percentage speed error at point i is defined as in equation (5.19).

$$e_i = 100 \frac{\|\mathbf{u}_i^f - \mathbf{u}_i\|}{\|\mathbf{u}_i\|}, \quad \|\mathbf{u}\| = \sqrt{u^2 + v^2}$$
 (5.19)

In figure 5.5, the field of  $e_i$  is shown for the second spatial mode fitted with parameters  $\eta_0 = 4$ ,  $N_x = 20$ , and  $N_y = 20$ . It is evident that the largest pointwise errors occur in the near-wake region, where velocity gradients are strongest and the toroidal basis struggles to resolve the field. The centres of points along the y-axis are also not well captured.

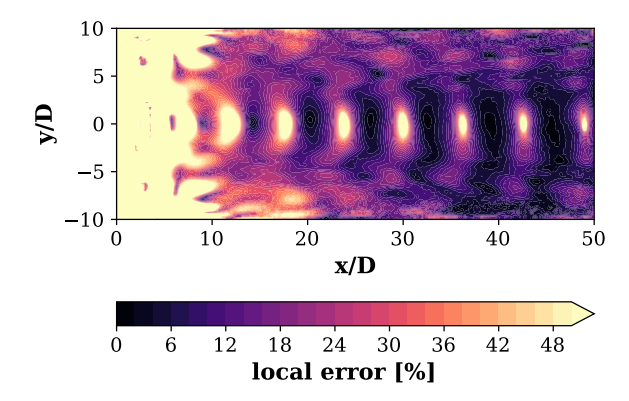


Figure 5.5: Local percentage speed error  $e_i$  (cf. (5.19)) for mode 2, with  $\eta_0 = 4$ ,  $N_x = 20$ ,  $N_y = 20$ .

#### 5.3.2. Global Root-Mean-Square Error (RMSE)

While the local error  $e_i$  highlights spatial regions of poor fit, a single scalar measure is desired to compare different truncations  $(N_x, N_y)$ . Accordingly, the global RMSE for mode m is defined as in equation (5.20).

$$\varepsilon_{\text{rms}}^{(m)} = \sqrt{\frac{\sum_{i=1}^{N_s} \left[ (u_i - u_i^f)^2 + (v_i - v_i^f)^2 \right]}{\sum_{i=1}^{N_s} (u_i^2 + v_i^2)}}$$
(5.20)

In equation (5.20)  $N_s$  is the total number of spatial sample points. The  $\varepsilon_{\rm rms}^{(m)}$  measures the  $L^2$ -norm of the velocity-difference field, normalized by the  $L^2$ -norm of the original velocity field for that mode. Values of  $\varepsilon_{\rm rms}$  close to zero indicate excellent overall agreement.

#### 5.3.3. Dependence on $(N_x, N_y)$

To explore how the fit accuracy depends on the tensor-product truncation orders  $N_x$  and  $N_y$ , a grid search is performed over  $N_x \in \{6, 8, 10, 12, 14, 16, 18, 20\}$ ,  $N_y \in \{6, 8, 10, 12, 14, 16, 18, 20\}$ . For each pair  $(N_x, N_y)$ ,  $\varepsilon_{\rm rms}^{(m)}$  is computed for modes m = 1, 2, 3, 4. The results for the first four modes are displayed in figure 5.6. In all cases,  $\varepsilon_{\rm rms}$  remains above approximately 20%, even at the highest truncations. The performance does not improve for higher order modes and the error will likely only increase as the spatial modes cover smaller spatial patterns that are more difficult to capture. The remaining global error plots can be seen in appendix F.

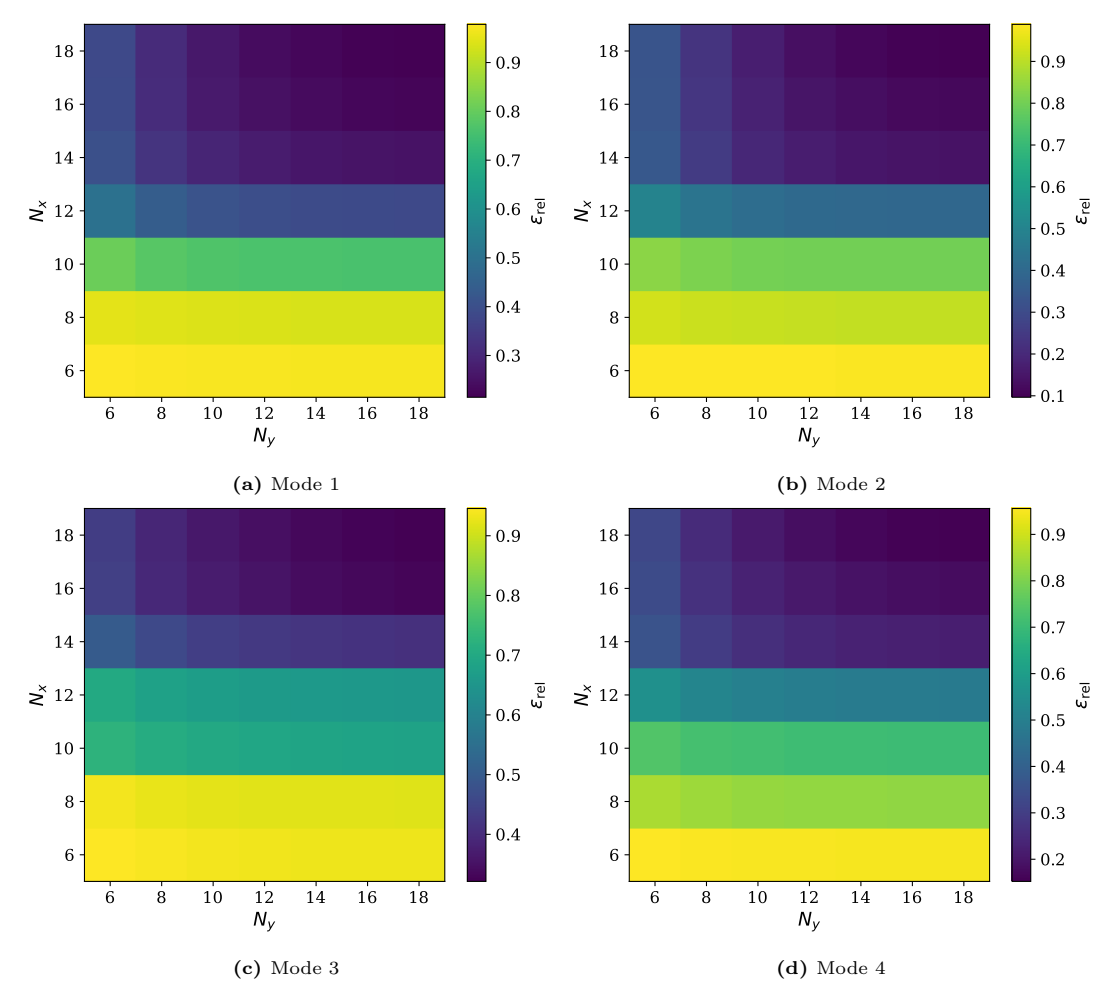


Figure 5.6: Global RMSE  $\varepsilon_{\text{rms}}^{(m)}$  (cf. (5.20)) as a function of  $(N_x, N_y)$ . Each contour plot corresponds to one of the first four spatial modes.

#### 5.3.4. Impact of Stream Function Fits on the SROM Reconstruction

The root mean square errors (RMSE) reported in the previous section indicate that the Integrated Laguerre–Hermite basis fits introduce non-negligible errors, typically around 20%. These individual fitting errors may accumulate when the fitted modes serve as the spatial basis within the stochastic reduced-order model (SROM) described in section 3.2.2. This section illustrates how these spatial mode fitting errors propagate into the SROM reconstruction performance.

Due to computational constraints, performing optimal fits for all spatial modes (over 200 modes up to the energy cut-off) is not feasible. Therefore, this analysis is limited to the first ten spatial modes, which capture approximately 64% of the total flow energy and significantly influence the turbulent kinetic energy (TKE) reconstruction.

For comparison, 20 stochastic realisations of the SROM are generated according to the methodology described in Section 3.2.2, employing spectral colouring to enforce consistent phases for the first ten dominant modes. Two distinct sets of realisations are generated: one using the original POD spatial modes (POD basis) and another using spatial modes fitted with the Integrated Laguerre–Hermite basis. For each mode the truncation orders that minimizes the global RMSE error are chosen from the tested values of  $N_x \in \{6, 8, 10, 12, 14, 16, 18, 20\}$  and  $N_y \in \{6, 8, 10, 12, 14, 16, 18, 20\}$ .

Each set is compared with the original flow data, and ensemble averages are calculated over the 20 realisations to mitigate statistical variability inherent to the stochastic approach.

The comparison metric chosen is the turbulent kinetic energy (TKE), defined solely in terms of streamwise

(u') and cross-stream (v') velocity fluctuations as per equation (5.21).

$$TKE_{uv}(x, y) = \frac{u'^{2}(x, y) + v'^{2}(x, y)}{2}$$
(5.21)

The reconstruction error at each spatial location (x, y) is quantified as in equation (5.22).

$$TKE_{error,uv}(x,y) = \frac{|TKE_{original,uv}(x,y) - TKE_{generated,uv}(x,y)|}{TKE_{original,uv}(x,y)}$$
(5.22)

Figure 5.7 presents the spatial distribution of TKE reconstruction errors. Figure 5.7(a) illustrates the error distribution for the original POD basis. Errors approaching 80% are observed across a significant portion of the domain, primarily due to the limited energy captured by the first ten modes. However, regions along the centerline (y = 0) downstream of the cylinder exhibit relatively lower errors, approximately 20%.

Figure 5.7(b) shows the corresponding errors when using the Integrated Laguerre–Hermite basis. This basis yields notably higher errors compared to the POD basis, particularly near the cylinder and outside the conical shape of the wake. Errors exceeding 80% dominate these regions. This occurs because the fitted spatial modes slightly overestimate velocity fluctuations in regions where the actual fluctuations are minimal, thereby causing large relative errors.

The difference between the two methods, depicted in figure 5.7(c), highlights explicitly where the Integrated Laguerre–Hermite basis performs poorly relative to the POD basis. The most pronounced differences occur immediately downstream of the cylinder outside of the conically shaped wake where the Integrated Laguerre-Hermite basis overestimates the velocity greatly.

Overall, the spatial distribution plots clearly indicate that the Integrated Laguerre–Hermite basis, despite its mathematical convenience, introduces substantial reconstruction inaccuracies when used in the SROM frameworks. These inaccuracies are attributable to the low variability in large sections of the flow. A relatively high basis order is also required to reproduce these modes as is evident from the contour plots in figure 5.6. Excluding the low variance points from the analysis is expected to improve the fittings. This can also be done by reducing the weighting of points in this region and performing a weighted-least squares (WLSQ) fitting.

Because only the first ten spatial modes are retained, the local TKE<sub>error,uv</sub> is evaluated against a truncated reconstruction. Overestimating the amplitude of one fitted mode can therefore reduce the TKE error at a given point if the overshoot accidentally compensates for fluctuating energy that would otherwise be carried by the discarded higher-order modes. This apparent improvement is an artefact of the truncation: were all POD modes included, the same overshoot would instead manifest as an increased error at that location. Hence a low local TKE error does not, by itself, guarantee that the underlying velocity field has been captured faithfully; it can also indicate a cancellation between fitting errors and modal truncation.

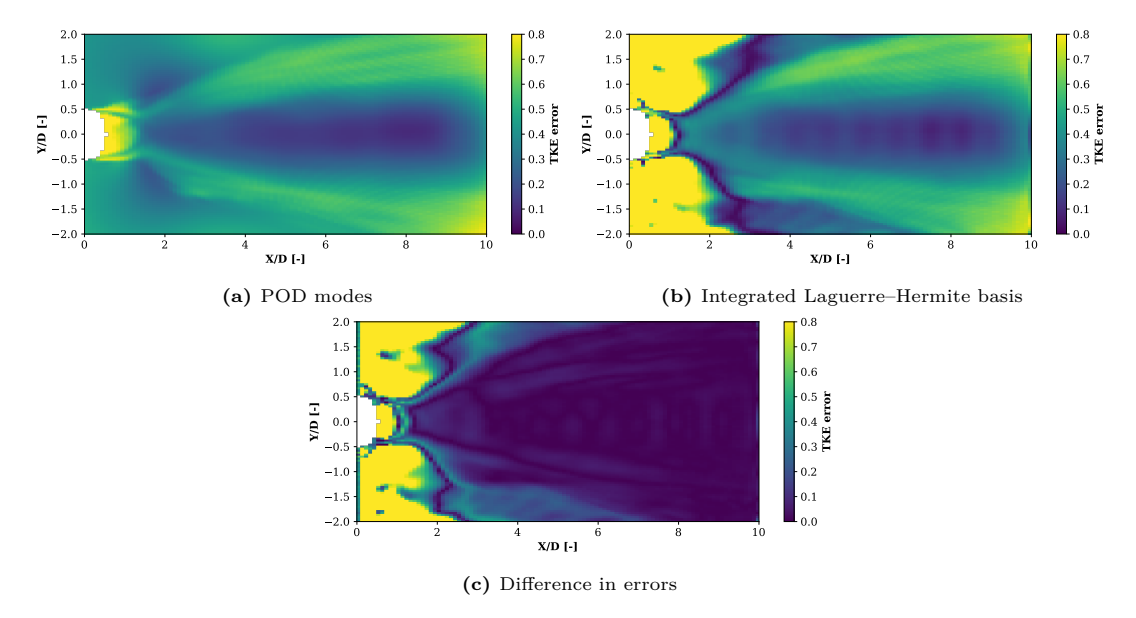


Figure 5.7: Spatial distribution of relative TKE reconstruction errors (TKE<sub>error,uv</sub>) for (a) original POD basis, (b) Integrated Laguerre–Hermite basis, and (c) the difference between the two methods.

#### 5.3.5. Projection and Subspace Errors

The snapshot matrix A is factored by the singular-value decomposition  $A = U \Sigma V^{\mathsf{T}}$  with singular values  $\sigma_1 \geq \sigma_2 \geq \cdots \geq \sigma_T$ . According to the Eckart-Young-Mirsky theorem [84], the best rank-10 approximation in the Frobenius norm is the truncated SVD as per equation (5.23).

$$A_{10} = U_{(:,1:10)} \Sigma_{(1:10,1:10)} V_{(:,1:10)}^{\mathsf{T}}$$
(5.23)

The relative RMS error of the truncated SVD is defined as in equation (5.24). Here  $||\cdot||_F$  denotes the Frobenius norm of the matrix.

$$\varepsilon_{\text{opt}} = \frac{\|A - A_{10}\|_{\text{F}}}{\|A\|_{\text{F}}} = \sqrt{\frac{\sum_{k>10} \sigma_k^2}{\sum_{k\geq 1} \sigma_k^2}}$$
(5.24)

For the present data set  $\varepsilon_{\rm opt} = 0.60103$ ; hence, at most  $1 - \varepsilon_{\rm opt}^2 \approx 64\%$  of the kinetic energy can be recovered by any ten–dimensional subspace. As figure 4.7 confirms, the cumulative energy of the first ten singular values is indeed 64 %.

Let the fitting of the modes U be F as described by equation (5.25). The fitted-mode matrix F has exactly the same dimensions as the leading POD matrix  $U_{(:,1:10)}$ . The zeros in matrix are the w-component values that are not fit and are set to zero.

$$F = \begin{bmatrix} u_1 & u_2 & \cdots & u_{10} \\ v_1 & v_2 & \cdots & v_{10} \\ 0 & 0 & \cdots & 0 \end{bmatrix} \in \mathbb{R}^{3M \times 10}$$
 (5.25)

Projecting the snapshots onto F and reconstructing gives equation (5.26).

$$\varepsilon_{\text{fit}} = \frac{\|A - FF^{\mathsf{T}}A\|_{\text{F}}}{\|A\|_{\text{F}}} = 0.66881.$$
 (5.26)

Relative to the optimal error, the additional penalty introduced by enforcing divergence-free, no-slip and zero-w constraints is then  $\Delta \varepsilon = \varepsilon_{\rm fit} - \varepsilon_{\rm opt} = 0.06678$ 

Each column  $\mathbf{a}_j$   $(j=1,\ldots,T)$  of the snapshot matrix  $A \in \mathbb{R}^{3M \times T}$  contains all three velocity components at the M spatial points for a single instant in time, that is,  $\mathbf{a}_j$  is one complete flow snapshot. Its squared Euclidean norm  $\|\mathbf{a}_j\|_2^2 = \sum_{p=1}^{3M} u_{p,j}^2$  equals the instantaneous kinetic energy of that snapshot. Summing over all time steps yields the Frobenius norm of equation (5.27).

$$||A||_{\mathcal{F}}^{2} = \sum_{j=1}^{T} ||\mathbf{a}_{j}||_{2}^{2} = \sum_{p=1}^{3M} \sum_{j=1}^{T} u_{p,j}^{2}$$
(5.27)

Equation (5.27) represents the total space—time kinetic energy contained in the data set. A spatial location p contributes in proportion to the variance of its velocity signal,  $\text{var}(u_p(t)) = \frac{1}{T} \sum_{j=1}^T u_{p,j}^2$ . Regions with strong fluctuations—such as the core of the von Kármán street—therefore carry a larger weight in the global RMS errors  $\varepsilon_{\text{opt}}$  and  $\varepsilon_{\text{fit}}$  than regions near or just outside the conical wake.

The pointwise TKE error used earlier is valuable because it highlights where the SROM reconstruction over- or under-predicts local fluctuation energy. The global Frobenius-norm measure  $\varepsilon_{\rm fit}$  plays a complementary role: it reports the total net kinetic-energy mismatch. Hence it reflects the combined impact of energy that is lost by truncating the expansion to ten modes similar to the energy cut-off. Furthermore the  $\Delta\varepsilon$  highlights how much the energy in the flow is lost or misplaced. This illustrates how much the physical constraints hinder the representation of the modes. Where local over- and underpredictions balance each other, the TKE map still shows large errors, whereas the global norm reveals that the overall energetic discrepancy is smaller. In this sense the two metrics should be interpreted together: the TKE map diagnoses where the model is deficient, while  $\varepsilon_{\rm fit}$  indicates how severely those deficiencies affect the flows total energy as a whole.

## Conclusions and Recommendations

The objective of this thesis was to investigate methods for the establishment of a model for the wake behind wind turbine towers. The ultimate goal was then to use the outputs of a proposed model to conduct wind turbine load calculations, specifically for the downwind idling situation.

This chapter addresses the research questions as were outlined in chapter 1. The chapter serves to draw the general conclusions and recommendations from this research. It is structured into two sections. Firstly, section 6.1 addresses the research questions and the overall conclusion. Subsequently, in section 6.2, suggestions for future work are presented.

#### 6.1. Conclusions

The primary objective of this research was to develop a stochastic reduced-order model (SROM) capable of providing stochastic realisations of tower wake flow, suitable for use in wind turbine load simulations, particularly in the downwind idling scenario.

At the Reynolds numbers considered, capturing a significant share of the flow energy demands many modes; far more than what is typically observed at lower Reynolds numbers [64, 67, 68]. Because the spectrum is broad, the von Kármán street spans several modes. Even within the same transcritical vortex-shedding regime, vortex wavelength and wake width vary appreciably.

The primary observation made between the quasi-2D POD modes and the 3D modes is that the w-component of the velocity is captured with slightly more structure. The von Kármán street that is present in the first few modes in the 3D modes has a higher absolute value and is noticeably larger than the w-component seen in the quasi-2D simulated case. The same spatial patterns appear, but ordered differently by singular values. Likely this is attributable to the different coordinate system as the polar coordinate system captures more of the near wake where the majority of the energy of the shifting modes appear, whereas the quasi-2D field captures more of the far wake.

A notable limitation lies in the accurate representation of the near-wake region, directly downstream of the cylinder. This region is particularly challenging due to the prevalence of high-frequency, small-scale structures, which are not well resolved by the model. For the remainder of the domain the mode truncation of either the 95% energy or SVHT criterion demonstrated to result in reasonable TKE errors. These small, high-frequency fluctuations are effectively filtered out by the blade's large chord and span, so their contribution to the loads are negligible.

A single spatial basis cannot span the transcritical Reynolds range, because the modes themselves evolve with Reynolds number. The Grassmann manifold basis interpolation was tested as a method to perform an interpolation of the spatial basis. The basis performs better than the bases that lie on either end of the geodesic, but the improved performance is not large and the optimum does not necessarily reside in between the two bases. The primary modes are captured well with the method, but noticeable deviations quickly emerge for higher order modes.

6.2. Recommendations 70

The Grassmann interpolation method interpolates on the subspace of the bases. Therefore, mode pairs may be phase shifted as a rotation of the pairs is an equally valid solution in the subspace. The frequency shift that is applied requires the mode pairs to reside in a specific phase with respect to other modes. The applicability of the Grassmann manifold interpolation in combination with the frequency shift is therefore more limited.

As wind speed rises, so do the flow energy and the corresponding singular values. A suitable singular should be assigned to each mode. Such a singular value should reside somewhere between the singular values from the datasets on either side of the geodesic, but the exact placement is not immediately evident.

Overall the Grassmann manifold interpolation requires the manual tuning of many parameters and assignment of time series for a large amount of modes. The primary modes do not carry the relatively large amounts of energy as is seen in lower Reynolds studies. To then capture a significant fraction of the energy in the flow many more modes are needed. For a smaller amount of modes the interpolation method seems more suitable as the tuning is easier and the modes carry the most resemblance. High alignment is seen for the first mode pair and the Grassmann manifold can effectively predict this mode pair. The pair was not found to reside exactly halfway along the geodesic and phase alignment is necessary to attain the highest MAC value.

The mode correlation decays exponentially, a trend that fits simple decaying functions. The modal correlation of the first mode was found to match the correlation of forcing seen on cylinders at lower Reynolds numbers for the 3D simulations of the oscillating cylinders, but not for the stationary cylinder. The differences may be attributable to the no-penetration boundary and the limited height of the simulated cylinders.

The modes from the 3D simulations are similar in appearance to the quasi-2D modes with a small difference seen in the Strouhal number. The w-component of the velocity was illustrated to be small. The correlation coefficient may be fitted to any desired observed correlation. A three dimensional flow can therefore be constructed using modes obtained through a quasi-2D simulation as such a simulation effectively captures the same flow patterns.

Stream function fitting was performed on the u and v-components of the flow. The fitting was demonstrated to require many basis functions to attain fits. The quality of the fits quickly deteriorates for higher order spatial modes. Many points were included that carry little variance and this makes the fittings more difficult with large errors seen in these regions. The far wake is captured with far greater accuracy. By imposing the physical restraints through the stream function fitting the kinetic energy in the flow does not deviate largely.

The proposed model in this thesis is restricted to movements of the tower in the side-side direction. As illustrated in the literature review, movements in different directions and frequencies influence the structures behind the cylinder. The current model does not consider how these different flow structures translate into different spatial mode patterns. Smoothly transitioning between these mode patterns is not possible within the framework of the model. When large fore-aft movements occur for an undamped turbine, this model is not applicable.

Through this research 3D SROM models were found to be effective at capturing the turbulent kinetic energy of the flow and the correlation along the height of a tower can be effectively enforced. The proposed model is limited to single wind speed from which the flow modes are derived as the interpolation of modes between wind speeds was not found to be effective enough at these high Reynolds numbers. The model therefore suits tower sections with nearly uniform diameter, low wind shear and minimal fore-aft motion. Wind shear and turbulence intensity decorrelate the flow. Hence, the von Kármán street is seen over a smaller section of the tower. A more correlated flow is believed to be a more conservative estimate for load simulations of the down wind idling situation.

#### 6.2. Recommendations

Recent literature suggests that Permuted POD (PPOD) may offer improved performance in capturing translating flow structures [66]. Testing this method may result in modes that capture a significant amount of energy inside a single pair mode. This may make the Grassmann manifold interpolation more

6.2. Recommendations 71

effective as fewer modes would have to be interpolated, although its applicability with PPOD is yet unexplored.

The applicability of the model with imposed shear and changing diameter along the tower may be tested. Current studies suggest that these effects decorrelate the flow [16, 18]. Studying whether this may be resolved through imposing changes to the correlation coefficient or whether the modes shapes change significantly may be explored further. Testing this initially for lower Reynolds numbers and only subsequently for these high Reynolds number cases is preferred as the computational cost of the CFD simulations are significant.

Another important constraint is that the developed ROM does not advance for each time step. Rather it generates a complete time series for a specified length of time. This renders it incompatible with simulation environments such as BHAWC and HAWC2 [85], which rely on time-stepped inputs. Tower motions are simulated in these software. As outlined in the literature overview, an ideal model would consider the movements of the tower when determining the shape of the wake. The model in this thesis only considers the modes of an anti-symmetric von Kármán street, rather than a broader range of modes that may occur depending on the motion of the cylinder. Making a reduced order flow model where flow modes transition smoothly depending on the oscillatory motion remains an unclear unexplored challenge.

For larger side-to-side motion of the tower, the wake becomes more coherent and the correlation coefficient in the SROM ought to increase with motion amplitude. A proposed procedure for implementation in turbine-simulation environments is therefore to generate the flow in short blocks and update the correlation coefficient at the end of each block using the current tower motion. To prevent artificial discontinuities at block boundaries, a brief transition window between successive blocks—during which flow statistics blend smoothly—would also be required. The idea has not yet been validated in practice and therefore remains a proposal for future implementation.

The thesis evaluated the generated flows mainly through turbulent kinetic energy (TKE). More error metrics are desired in order to confirm the efficacy of the model. Other metrics may include enstrophy or helicity. Subspace error metrics such as the Grassmann geodesic distance [74] or the Asimov distance [75] should also be employed to better compare the effectiveness of the Grassmann interpolation method.

The flow proved to be largely two-dimensional. A POD may be performed on the w-component of vorticity of the flow. This effectively makes it two dimensional. The w-component may further be investigated by performing a POD solely on this component. More spatial patterns are then likely to be found. This can then serve as a verification step to assert that the assumption of two-dimensional flow for the three-dimensional model remains valid.

- [1] Victhalia Zapata Castillo et al. "Future global electricity demand load curves". English. In: *Energy* 258 (Nov. 2022). Funding Information: The paper benefitted from funding from the European Research Council under grant ERC-CoG PICASSO (n° 819566). Publisher Copyright: © 2022 The Authors. ISSN: 0360-5442. DOI: 10.1016/j.energy.2022.124741.
- [2] Ivan Komusanac et al. Wind Energy in Europe: 2021 Statistics and the Outlook for 2022-2026. WindEurope Business Intelligence, Feb. 2022. URL: https://windeurope.org.
- [3] Luis Vera-Tudela and Martin Kühn. "Analysing wind turbine fatigue load prediction: The impact of wind farm flow conditions". In: Renewable Energy 107 (2017), pp. 352-360. ISSN: 0960-1481. DOI: https://doi.org/10.1016/j.renene.2017.01.065. URL: https://www.sciencedirect.com/science/article/pii/S0960148117300757.
- [4] Yang Ma, Pedro Martinez-Vazquez, and Charalampos Baniotopoulos. "Wind turbine tower collapse cases: a historical overview". In: *Proceedings of the Institution of Civil Engineers-Structures and Buildings* 172.8 (2019), pp. 547–555.
- [5] James Carroll, Alasdair McDonald, and David McMillan. "Failure rate, repair time and unscheduled O&M cost analysis of offshore wind turbines". In: Wind Energy 19.6 (2016), pp. 1107-1119. DOI: https://doi.org/10.1002/we.1887. eprint: https://onlinelibrary.wiley.com/doi/pdf/10.1002/we.1887. URL: https://onlinelibrary.wiley.com/doi/abs/10.1002/we.1887.
- [6] Th Von Karman. "Über den Mechanismus des Widerstandes, den ein bewegter Körper in einer Flüssigkeit erfährt". In: Nachrichten von der Gesellschaft der Wissenschaften zu Göttingen, Mathematisch-Physikalische Klasse 1911 (1911), pp. 509–517.
- [7] Jürgen Wagner. Visualisation of the vortex street behind a circular cylinder in air, using glycerol vapour. Wikimedia Commons. Self-photographed; accessed 13 June 2025. URL: https://en.wikipedia.org/wiki/File:Karmansche\_Wirbelstr\_kleine\_Re.JPG.
- [8] B. Mutlu Sumer and Jørgen Fredsøe. *Hydrodynamics Around Cylindrical Structures*. Vol. 12. Advanced Series on Ocean Engineering. Reprinted 1999. Singapore: World Scientific Publishing Co. Pte. Ltd., 1997, pp. 3, 7, 11.
- [9] Vincenz Strouhal. Über eine besondere Art der Tonerregung. Stahel, 1878.
- [10] John H Lienhard et al. Synopsis of lift, drag, and vortex frequency data for rigid circular cylinders. Vol. 300. Technical Extension Service, Washington State University Pullman, WA, 1966.
- [11] Mahdi Bandizadeh Sharif et al. "A review of the flow-induced vibrations (FIV) in marine circular cylinder (MCC) fitted with various suppression devices". In: Ocean Engineering 289 (2023), p. 116261. ISSN: 0029-8018. DOI: https://doi.org/10.1016/j.oceaneng.2023.116261. URL: https://www.sciencedirect.com/science/article/pii/S0029801823026458.
- [12] Jr. Cincotta J. J., G. W. Jones, and R. W. Walker. *Aerodynamic Forces on a Stationary and Oscillating Circular Cylinder at High Reynolds Numbers*. Technical Report NASA-TR-R-300. Public Use Permitted. Accession Number: 69N17304. Hampton, VA, United States: NASA Langley Research Center, Feb. 1969. URL: https://ntrs.nasa.gov/citations/19690007972.
- [13] Tsutomu Adachi. "Effects of surface roughness on the universal Strouhal number over the wide Reynolds number range". In: Journal of Wind Engineering and Industrial Aerodynamics 69-71 (1997). Proceedings of the 3rd International Colloqium on Bluff Body Aerodynamics and Applications, pp. 399–412. ISSN: 0167-6105. DOI: https://doi.org/10.1016/S0167-6105(97) 00172-4. URL: https://www.sciencedirect.com/science/article/pii/S0167610597001724.
- [14] JCK Cheung and WH Melbourne. "Turbulence effects on some aerodynamic parameters of a circular cylinder at supercritical numbers". In: *Journal of wind engineering and industrial aerodynamics* 14.1-3 (1983), pp. 399–410.

[15] J. Fredsoe and B.M. Sumer. *Hydrodynamics Around Cylindrical Structures (Revised Edition)*. Advanced Series On Ocean Engineering. World Scientific Publishing Company, 2006. ISBN: 9789814476980. URL: https://books.google.nl/books?id=LLPICgAAQBAJ.

- [16] Owen M Griffin. "Vortex shedding from bluff bodies in a shear flow: a review". In: *Journal of Fluid Engineering* (1985).
- [17] David Surry. "Some effects of intense turbulence on the aerodynamics of a circular cylinder at subcritical Reynolds number". In: *Journal of Fluid Mechanics* 52.3 (1972), pp. 543–563.
- [18] Hiroshi Tanaka DrEng. "PRESSURE CORRELATIONS ON A VIBRATING CYLINDER". In: Proceedings of the Fourth International Conference on Wind Effects on Buildings and Structures: Heathrow 1975. Cambridge University Press. 1975, pp. 227–232.
- [19] Gerrit H. Toebes. "Fluidelastic Features of Flow Around Cylinders". In: Proceedings of the International Research Seminar on Wind Effects on Buildings and Structures. Presented on 15 September 1967. Ottawa, Canada: Colorado State University Libraries, Sept. 1967, pp. 323–341.
- [20] A Kozakiewicz, BM Sumer, and J Fredsøe. "Spanwise correlation on a vibrating cylinder near a wall in oscillatory flows". In: *Journal of fluids and structures* 6.3 (1992), pp. 371–392.
- [21] Christoffer Norberg. "Fluctuating lift on a circular cylinder: review and new measurements". In: Journal of Fluids and Structures 17.1 (2003), pp. 57–96.
- [22] Seong Mo Yeon, Jianming Yang, and Frederick Stern. "Large-eddy simulation of the flow past a circular cylinder at sub-to super-critical Reynolds numbers". In: *Applied Ocean Research* 59 (2016), pp. 663–675.
- [23] K Ebstrup et al. "Numerical investigation of vortex-induced forces on a wind turbine tower segment at very high Reynolds numbers". In: *Journal of Physics: Conference Series*. Vol. 2767. 2. IOP Publishing. 2024, p. 022048.
- [24] Kyle D Squires, Vivek Krishnan, and James R Forsythe. "Prediction of the flow over a circular cylinder at high Reynolds number using detached-eddy simulation". In: *Journal of Wind Engineering and Industrial Aerodynamics* 96.10-11 (2008), pp. 1528–1536.
- [25] Robert D. Blevins. *Flow-Induced Vibration*. 2nd. Malabar, Florida: Krieger Publishing Company, 2001. ISBN: 1-57524-183-8.
- [26] ME Davies. "A comparison of the wake structure of a stationary and oscillating bluff body, using a conditional averaging technique". In: *Journal of Fluid Mechanics* 75.2 (1976), pp. 209–231.
- [27] Owen M Griffin and Steven E Ramberg. "The vortex-street wakes of vibrating cylinders". In: *Journal of Fluid Mechanics* 66.3 (1974), pp. 553–576.
- [28] Gerrit H Toebes. "The unsteady flow and wake near an oscillating cylinder". In: *Journal of Basic Engineering* 91.3 (1969), p. 493.
- [29] S. E. Ramberg and O. M. Griffin. "Vortex Formation in the Wake of a Vibrating, Flexible Cable". In: Journal of Fluids Engineering 96.4 (Dec. 1974), pp. 317-322. ISSN: 0098-2202. DOI: 10.1115/1. 3447164. eprint: https://asmedigitalcollection.asme.org/fluidsengineering/article-pdf/96/4/317/5642061/317\\_1.pdf. URL: https://doi.org/10.1115/1.3447164.
- [30] R. E. D. Bishop and A. Y. Hassan. "The Lift and Drag Forces on a Circular Cylinder in a Flowing Fluid". In: *Proceedings of the Royal Society of London. Series A, Mathematical and Physical Sciences* 277.1368 (1964), pp. 32–50. ISSN: 00804630. URL: http://www.jstor.org/stable/2414647 (visited on 06/17/2025).
- [31] Turgut Sarpkaya. "Fluid forces on oscillating cylinders". In: Journal of the Waterway, Port, Coastal and Ocean Division 104.3 (1978), pp. 275–290.
- [32] C.H.K. Williamson and A. Roshko. "Vortex formation in the wake of an oscillating cylinder". In: Journal of Fluids and Structures 2.4 (1988), pp. 355-381. ISSN: 0889-9746. DOI: https://doi.org/10.1016/S0889-9746(88)90058-8. URL: https://www.sciencedirect.com/science/article/pii/S0889974688900588.
- [33] M.M. Zdravkovich. "Review and classification of various aerodynamic and hydrodynamic means for suppressing vortex shedding". In: Journal of Wind Engineering and Industrial Aerodynamics 7.2 (1981), pp. 145–189. ISSN: 0167-6105. DOI: https://doi.org/10.1016/0167-6105(81)90036-2. URL: https://www.sciencedirect.com/science/article/pii/0167610581900362.

[34] A. Ongoren and D. Rockwell. "Flow structure from an oscillating cylinder Part 1. Mechanisms of phase shift and recovery in the near wake". In: *Journal of Fluid Mechanics* 191 (1988), pp. 197–223. DOI: 10.1017/S0022112088001569.

- [35] T. Sarpkaya. "A critical review of the intrinsic nature of vortex-induced vibrations". In: Journal of Fluids and Structures 19.4 (2004), pp. 389-447. ISSN: 0889-9746. DOI: https://doi.org/10.1016/j.jfluidstructs.2004.02.005. URL: https://www.sciencedirect.com/science/article/pii/S0889974604000350.
- [36] Dimitrios Livanos. "Investigation of Vortex Induced Vibrations on Wind Turbine Towers". Master of Science Thesis. Delft, Netherlands: Delft University of Technology, Oct. 2018. URL: https://repository.tudelft.nl/record/uuid:90b62a9f-0740-4798-8a9a-7b2708756268.
- [37] Ika Kurniawati et al. "Vortex shedding load on a full-scale wind turbine tower at transcritical Reynolds numbers". In: *Journal of Wind Engineering and Industrial Aerodynamics* 252 (2024), p. 105821. ISSN: 0167-6105. DOI: https://doi.org/10.1016/j.jweia.2024.105821. URL: https://www.sciencedirect.com/science/article/pii/S0167610524001843.
- [38] Ika Kurniawati et al. "Vortex-induced vibrations and post-lock-in cross-wind oscillations of wind turbine tower based on field measurements". In: Journal of Wind Engineering and Industrial Aerodynamics 258 (2025), p. 106010. ISSN: 0167-6105. DOI: https://doi.org/10.1016/j.jweia. 2025.106010. URL: https://www.sciencedirect.com/science/article/pii/S0167610525000 066.
- [39] S Bahramiasl and E de Langre. "Loss of lock-in in VIV due to spanwise variations of diameters". In: Ocean Engineering 220 (2021), p. 108446.
- [40] Aaron Towne, Oliver T. Schmidt, and Tim Colonius. "Spectral proper orthogonal decomposition and its relationship to dynamic mode decomposition and resolvent analysis". In: *Journal of Fluid Mechanics* 847 (May 2018), pp. 821–867. ISSN: 1469-7645. DOI: 10.1017/jfm.2018.283. URL: http://dx.doi.org/10.1017/jfm.2018.283.
- [41] Daniel B. Araya, Tim Colonius, and John O. Dabiri. "Transition to bluff-body dynamics in the wake of vertical-axis wind turbines". In: *Journal of Fluid Mechanics* 813 (2017), pp. 346–381. DOI: 10.1017/jfm.2016.862.
- [42] Dewanshu Deep, Ashwin Sahasranaman, and S. Senthilkumar. "POD analysis of the wake behind a circular cylinder with splitter plate". In: European Journal of Mechanics B/Fluids 93 (2022), pp. 1-12. ISSN: 0997-7546. DOI: https://doi.org/10.1016/j.euromechflu.2021.12.010. URL: https://www.sciencedirect.com/science/article/pii/S0997754621002065.
- [43] S. J. Andersen and J. P. Murcia Leon. "Stochastic wind farm flow generation using a reduced order model of LES". English. In: Wake Conference 2023, 20/06/2023 22/06/2023, Visby, Sweden. Vol. 2505. Journal of Physics: Conference Series. Wake Conference 2023; Conference date: 20-06-2023 Through 22-06-2023. United Kingdom: IOP Publishing, 2023. DOI: 10.1088/1742-6596/2505/1/012050.
- [44] Zhendong Luo and Goong Chen. Proper orthogonal decomposition methods for partial differential equations. Academic Press, an imprint of Elsevier, 2019.
- [45] Oliver T. Schmidt and Tim Colonius. "Guide to Spectral Proper Orthogonal Decomposition". In: AIAA Journal 58.3 (2020), pp. 1023-1033. DOI: 10.2514/1.J058809. eprint: https://doi.org/10.2514/1.J058809. URL: https://doi.org/10.2514/1.J058809.
- [46] Kunihiko Taira et al. "Modal Analysis of Fluid Flows: An Overview". In: AIAA Journal 55.12 (2017), pp. 4013-4041. DOI: 10.2514/1.J056060. eprint: https://doi.org/10.2514/1.J056060.
   URL: https://doi.org/10.2514/1.J056060.
- [47] Steven L. Brunton and J. Nathan Kutz. "Singular Value Decomposition (SVD)". In: Data-Driven Science and Engineering: Machine Learning, Dynamical Systems, and Control. Cambridge University Press, 2019, pp. 3–46, 235–246.
- [48] Moritz Sieber, C. Oliver Paschereit, and Kilian Oberleithner. "Spectral proper orthogonal decomposition". In: *Journal of Fluid Mechanics* 792 (2016), pp. 798–828. DOI: 10.1017/jfm.2016.103.
- [49] Nadine Aubry. "On the hidden beauty of the proper orthogonal decomposition". In: *Theoretical and Computational Fluid Dynamics* 2.5 (1991), pp. 339–352.

[50] Sasan Sarmast et al. "Mutual inductance instability of the tip vortices behind a wind turbine". In: *Journal of Fluid Mechanics* 755 (2014), pp. 705–731.

- [51] Peter Welch. "The use of fast Fourier transform for the estimation of power spectra: a method based on time averaging over short, modified periodograms". In: *IEEE Transactions on audio and electroacoustics* 15.2 (1967), pp. 70–73.
- [52] Julius S Bendat and Allan G Piersol. Random data: analysis and measurement procedures. John Wiley & Sons, 2011.
- [53] Gerhard Heinzel, Albrecht Rüdiger, and Roland Schilling. Spectrum and spectral density estimation by the Discrete Fourier Transform (DFT), including a comprehensive list of window functions and some new at-top windows. Technical Report. Accessed: 2025-04-03. Max-Planck-Institut für Gravitationsphysik, 2002. URL: https://hdl.handle.net/11858/00-001M-0000-0013-557A-5.
- [54] HexFluid. spod\_python: Pythonic Spectral Proper Orthogonal Decomposition. Online; accessed 13 January 2025. 2020.
- [55] J. H. Tu et al. "On dynamic mode decomposition: theory and applications". In: *Journal of Computational Dynamics* 1.2 (2014), pp. 391–421.
- [56] Matan Gavish and David L Donoho. "The optimal hard threshold for singular values is 4/\sqrt {3}". In: *IEEE Transactions on Information Theory* 60.8 (2014), pp. 5040–5053.
- [57] Jakob Mann. "The spatial structure of neutral atmospheric surface-layer turbulence". In: *Journal of Fluid Mechanics* 273 (1994), pp. 141–168. DOI: 10.1017/S0022112094001886.
- [58] Poul Sørensen, Anca D. Hansen, and Pedro André Carvalho Rosas. "Wind models for simulation of power fluctuations from wind farms". In: Journal of Wind Engineering and Industrial Aerodynamics 90.12 (2002). Fifth Asia-Pacific Conference on Wind Engineering, pp. 1381-1402. ISSN: 0167-6105. DOI: https://doi.org/10.1016/S0167-6105(02)00260-X. URL: https://www.sciencedirect.com/science/article/pii/S016761050200260X.
- [59] S. J. Andersen and J. P. Murcia Leon. "Predictive and stochastic reduced-order modeling of wind turbine wake dynamics". In: *Wind Energy Science* 7.5 (2022), pp. 2117–2133. DOI: 10.5194/wes-7-2117-2022. URL: https://wes.copernicus.org/articles/7/2117/2022/.
- [60] John Panickacheril John, Diego A Donzis, and Katepalli R Sreenivasan. "Laws of turbulence decay from direct numerical simulations". In: *Philosophical Transactions of the Royal Society A* 380.2218 (2022), p. 20210089.
- [61] T Tatsumi. "The theory of decay process of incompressible isotropic turbulence". In: *Proceedings of the Royal Society of London. Series A. Mathematical and Physical Sciences* 239.1216 (1957), pp. 16–45.
- [62] Tomomasa Tatsumi. "Statistical fluid mechanics and statistical mechanics of fluid turbulence". In: *Journal of Physics: Conference Series*. Vol. 318. 4. IOP Publishing. 2011, p. 042024.
- [63] Emil Simiu and DongHun Yeo. Wind effects on structures: Modern Structural Design for Wind. 4th ed. Wiley-Blackwell, 2019. ISBN: 978-1-119-37588-3.
- [64] Graham Riches, Robert Martinuzzi, and Chris Morton. "Proper orthogonal decomposition analysis of a circular cylinder undergoing vortex-induced vibrations". In: *Physics of Fluids* 30.10 (2018).
- [65] BERND R. NOACK et al. "A hierarchy of low-dimensional models for the transient and post-transient cylinder wake". In: Journal of Fluid Mechanics 497 (2003), pp. 335–363. DOI: 10.1017/S0022112003006694.
- [66] Hanna M Ek et al. "Permuted proper orthogonal decomposition for analysis of advecting structures". In: Journal of Fluid Mechanics 930 (2022), A14.
- [67] Benet Eiximeno et al. "On the wake dynamics of an oscillating cylinder via proper orthogonal decomposition". In: Fluids 7.9 (2022), p. 292.
- [68] HF Wang, HL Cao, and Y Zhou. "POD analysis of a finite-length cylinder near wake". In: Experiments in fluids 55 (2014), pp. 1–15.

[69] J. F. Céspedes Moreno, J. P. Murcia León, and S. J. Andersen. "Convergence and efficiency of global bases using proper orthogonal decomposition for capturing wind turbine wake aerodynamics". In: Wind Energy Science 10.3 (2025), pp. 597–611. DOI: 10.5194/wes-10-597-2025. URL: https://wes.copernicus.org/articles/10/597/2025/.

- [70] Ronald N. Bracewell. The Fourier Transform and Its Applications. 3rd. McGraw-Hill, 2000.
- [71] P. K. Yeung, X. M. Zhai, and Katepalli R. Sreenivasan. "Extreme events in computational turbulence". In: *Proceedings of the National Academy of Sciences* 112.41 (2015), pp. 12633-12638. DOI: 10.1073/pnas.1517368112. eprint: https://www.pnas.org/doi/pdf/10.1073/pnas.1517368112. URL: https://www.pnas.org/doi/abs/10.1073/pnas.1517368112.
- [72] David Amsallem and Charbel Farhat. "Interpolation method for adapting reduced-order models and application to aeroelasticity". In: AIAA journal 46.7 (2008), pp. 1803–1813.
- [73] Miroslav Pastor, Michal Binda, and Tomáš Harčarik. "Modal assurance criterion". In: Procedia Engineering 48 (2012), pp. 543–548.
- [74] Ke Ye and Lek-Heng Lim. "Schubert varieties and distances between subspaces of different dimensions". In: SIAM Journal on Matrix Analysis and Applications 37.3 (2016), pp. 1176–1197.
- [75] Daniel Asimov. "The grand tour: a tool for viewing multidimensional data". In: SIAM journal on scientific and statistical computing 6.1 (1985), pp. 128–143.
- [76] Pauli Virtanen et al. "SciPy 1.0: fundamental algorithms for scientific computing in Python". In: *Nature methods* 17.3 (2020), pp. 261–272.
- [77] S Chandrasekhar and L Woltjer. "On force-free magnetic fields". In: *Proceedings of the National Academy of Sciences* 44.4 (1958), pp. 285–289.
- [78] Brian Cantwell and Donald Coles. "An experimental study of entrainment and transport in the turbulent near wake of a circular cylinder". In: *Journal of fluid mechanics* 136 (1983), pp. 321–374.
- [79] Johan Hoffman and Claes Johnson. "Resolution of d'Alembert's paradox". In: *Journal of mathematical fluid mechanics* 12 (2010), pp. 321–334.
- [80] Václav Uruba, Pavel Procházka, and Vladislav Skála. "On the 3D dynamics of the wake behind a circular cylinder". In: *Topical Problems of Fluid Mechanics, Institute of Thermomechanics of the Czech Academy of Sciences* (2020), pp. 240–248.
- [81] Roland Schinzinger and Patricio AA Laura. Conformal mapping: methods and applications. Courier Corporation, 2012, pp. 53–56.
- [82] NIST Digital Library of Mathematical Functions. Release 1.2.4 of 2025-03-15. F. W. J. Olver et al. URL: https://dlmf.nist.gov/.
- [83] Florin Radu, Vitoriano Ruas, and Paulo Trales. "Hermite finite elements for convection-diffusion equations". In: arXiv preprint arXiv:1512.07642 (2015).
- [84] G.H. Golub, Alan Hoffman, and G.W. Stewart. "A generalization of the Eckart-Young-Mirsky matrix approximation theorem". In: *Linear Algebra and its Applications* 88-89 (1987), pp. 317–327. ISSN: 0024-3795. DOI: https://doi.org/10.1016/0024-3795(87)90114-5. URL: https://www.sciencedirect.com/science/article/pii/0024379587901145.
- [85] DTU Wind Energy. About HAWC2. https://www.hawc2.dk/about-hawc2. Accessed 27 June 2025. 2025. (Visited on 06/27/2025).



# Spatial Modes

In this appendix the spatial POD modes for the 11 ms<sup>-1</sup> dataset are presented.

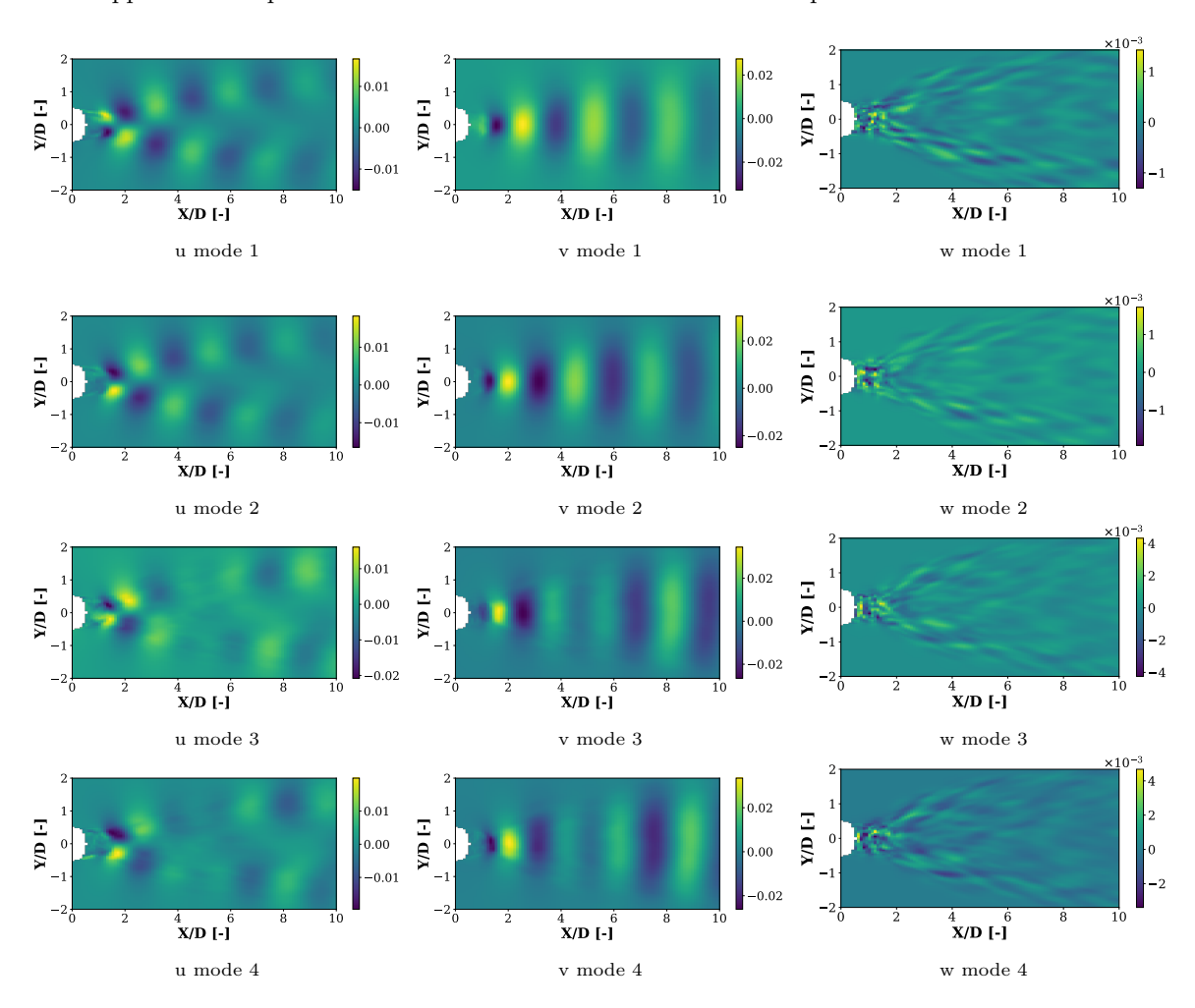


Figure A.1: First four 11  $\text{ms}^{-1}$  dataset POD modes of the velocity components u, v, and w.

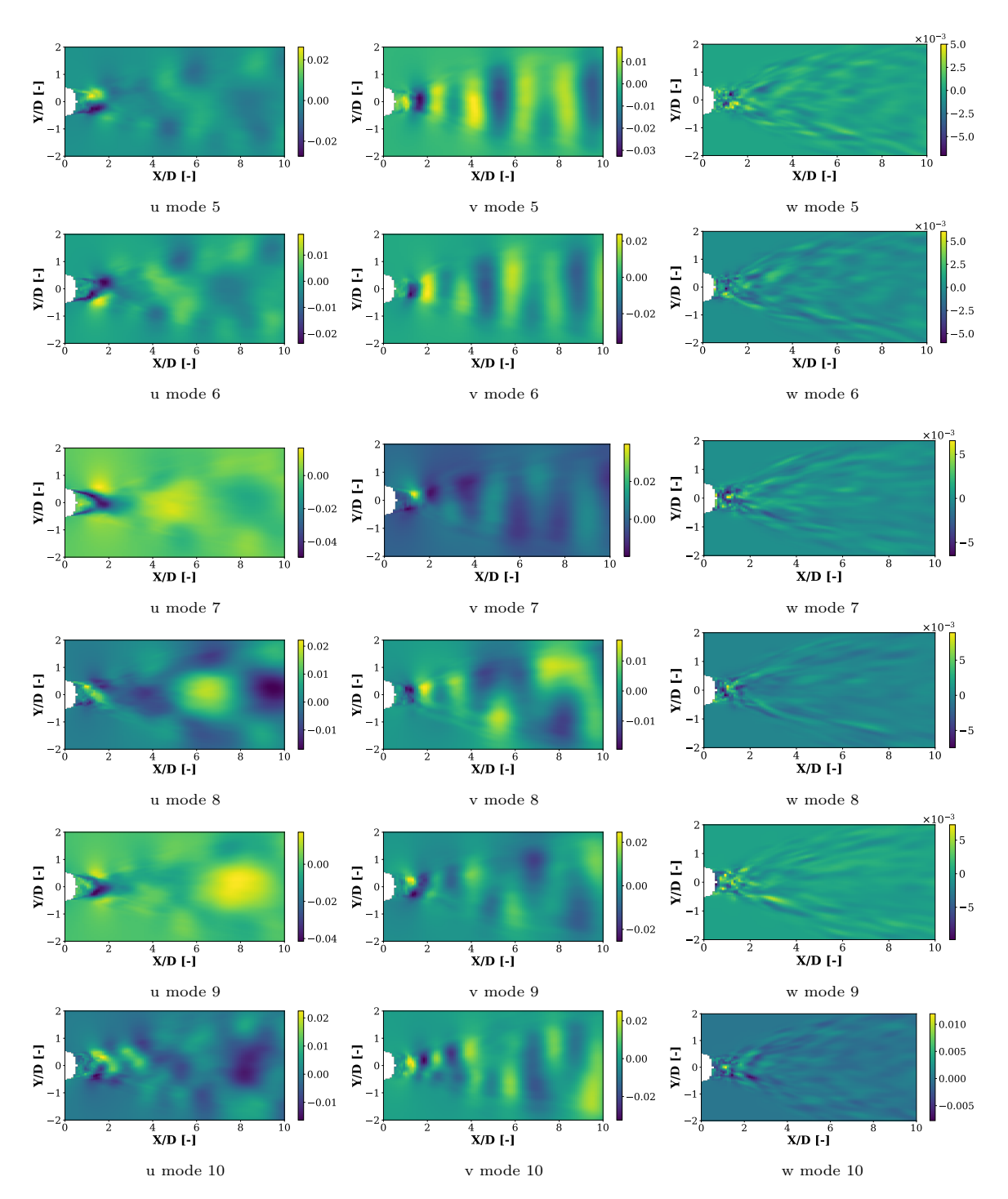


Figure A.2:  $11 \text{ ms}^{-1}$  dataset POD modes 5-10 of the velocity components u, v, and w.

## Proof that the Spectral Error Is Equivalent to a Variance Ratio

The spectral error, was introduced by [69] and is reproduced here in equation (B.1).

$$E_{S_{-i,j}} = \frac{\int_0^\infty (\hat{S}_i(f) - \hat{S}_j(f)) df}{\int_0^\infty \hat{S}_j(f) df}$$
(B.1)

Here  $\hat{S}_i(f)$  and  $\hat{S}_j(f)$  are the one-sided power spectral densities (PSDs) of the velocity component at a fixed spatial point, obtained from two separate realisations i and j.

#### Equivalence to a variance ratio

Let  $u_i(t)$  and  $u_j(t)$  denote the zero-mean velocity time series of the two realisations, sampled over a sufficiently long interval T. Parseval's theorem [70] states that

$$\int_0^\infty \hat{S}_i(f) \, df = \frac{1}{T} \int_{-T/2}^{T/2} u_i^2(t) \, dt = \sigma_i^2$$
 (B.2)

with  $\sigma_i^2$  the variance of  $u_i(t)$ , and analogously for  $\sigma_j^2$ . Substituting this result in equation (B.1) gives

$$E_{S_{-i,j}} = \frac{\sigma_i^2 - \sigma_j^2}{\sigma_j^2} = \frac{\sigma_i^2}{\sigma_j^2} - 1.$$

Hence the spectral error is exactly the fractional difference between the variances of the two signals, establishing its equivalence to a variance comparison.



### Rotational Extension of the MAC Criterion

The main text evaluates the Modal–Assurance Criterion (MAC) after re-ordering the slice modes with a permutation matrix  $P_z \in \mathcal{P}_k$ ,

$$\mathcal{P}_k = \{ P \in \{0, 1\}^{k \times k} : P^{\mathsf{T}} P = I, \det P = 1 \}.$$

Such a matrix merely exchanges column indices; it cannot perform the  $2 \times 2$  rotations that would bring a sine–cosine pair into perfect phase. The resulting MAC values therefore form a lower bound on the true sub-space similarity.

This simplification is acceptable when the leading pair already shows MAC  $\gtrsim 0.9$ ; however, it can mis-assign higher modes. A mode whose unrotated MAC is 0.5 might rotate by 90° to achieve MAC = 1, yet the permutation step would have paired it elsewhere.

#### Joint permutation-rotation problem

To avoid such mis-assignment, the permutation and the in-plane rotations must be selected simultaneously. With  $C := U_{\text{combined}}^{\mathsf{T}} U_{\text{slice},z}$ , consider the block–diagonal special-orthogonal set

$$\mathcal{B}_k = \left\{ Q = \operatorname{diag}(R_1(\theta_1), R_2(\theta_2), \dots, R_m(\theta_m), 1, \dots, 1) \right\}, \quad R_j(\theta) = \begin{pmatrix} \cos \theta & -\sin \theta \\ \sin \theta & \cos \theta \end{pmatrix}$$

Each block  $R_j$  supplies the single degree of freedom required to align one sine–cosine pair, while the unity entries leave any unpaired modes, such as slow drift modes seen in section 4.1, untouched.

The ideal alignment is obtained from equation (C.1).

$$\max_{\substack{P \in \mathcal{P}_k \\ Q \in \mathcal{B}_k}} \sum_{i=1}^k \left| (C P Q)_{ii} \right| \tag{C.1}$$

In this study the first few global modes are compared. When insights are desired into the similarity of many modes, and the modes are observed to be reordered, equation (C.1) should be utilized. This optimization uses a discrete search over k! permutations with a continuous search over m rotation angles; even for moderate k the factorial growth makes brute-force methods infeasible. The mode pairs must furthermore be clearly identified for this method to be applicable.

 $\mathbb{D}$ 

# Derivation of mass conservation for Hermite stream function basis

Define the Hermite basis with fixed width  $y_0$  as in equation (D.1). Where  $H_n$  are the physicists Hermite polynomials [82].

$$\chi_n(y) = \frac{H_n(y/y_0)}{\pi^{1/4} \sqrt{2^n n! y_0}} e^{-y^2/(2y_0^2)} \quad (n = 0, 1, \dots)$$
 (D.1)

orthonormal under  $\int_{-\infty}^{\infty} \chi_m \chi_n \, dy = \delta_{mn}.$ 

On a single x-slice position  $x_0$  the stream function is defined as in equation (D.2). Here  $B_k(x)$  are arbitrary basis functions that only depend on x.

$$\psi(x_0, y) = \sum_{k=0}^{N_x} \sum_{n=0}^{N_y} a_{kn} B_k(x_0) \chi_n(y), \qquad u = \partial_y \psi, \ v = -\partial_x \psi$$
 (D.2)

The mass flux Q though each vertical slice at a position  $x_0$  is given by equation (D.3).

$$Q := \int_{-\infty}^{\infty} u \, dy = \sum_{k=0}^{N_x} \sum_{n=0}^{N_y} a_{kn} B_k(x_0) \underbrace{\int_{-\infty}^{\infty} \partial_y \chi_n \, dy}_{I_n}$$
(D.3)

The integrals  $I_n$  are the physicists Hermite functions that tend to zero because  $\chi_n(y) \to 0$  as  $|y| \to \infty$ .

$$I_n = \chi_n(y)|_{y=-\infty}^{y=\infty} = 0$$
 (D.4)

$$I_n = \int_{-\infty}^{\infty} \partial_y \chi_n \, dy = 0 \qquad \forall \, n \ge 0.$$
 (D.5)

Hence mass is conserved:

Q = 0 for any coefficients  $\{a_n\}$  and any N.



## Correlation Coefficient Fits

In this appendix, the correlation coefficient fits are presented alongside tables of the respective parameters for their curves.

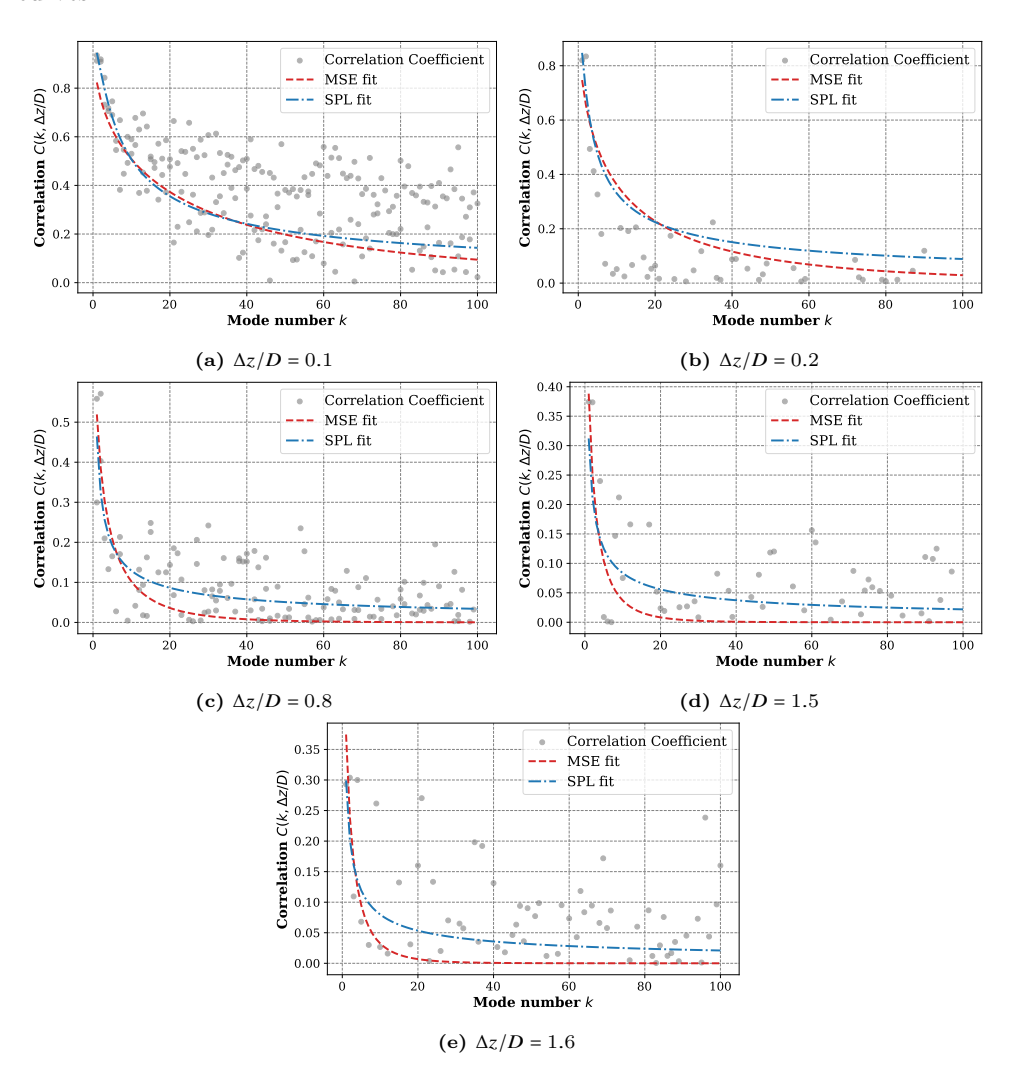


Figure E.1: Correlation coefficient fitting use MSE and SPL curves of oscillating cylinder with 2a/D = 0.1.

**Table E.1:** Optimised parameters for the two-variable decay models of oscillating cylinder with 2a/D = 0.1.

Model	а	α	β	p
MSE	0.934	0.496	0.340	-
$\operatorname{SPL}$	8.92	1.76	1.48	0.394

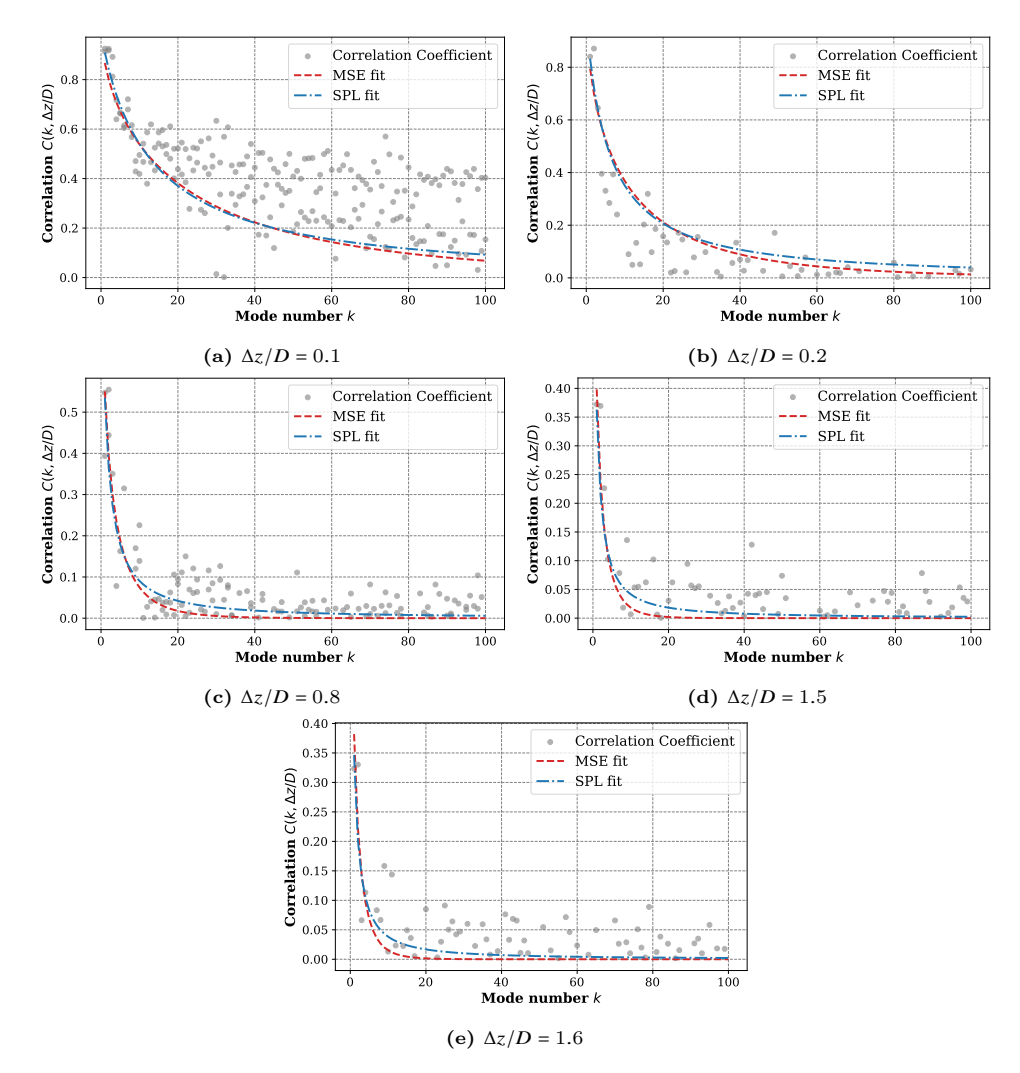


Figure E.2: Correlation coefficient fitting use MSE and SPL curves of stationary cylinder.

 $\textbf{Table E.2:} \ \ \textbf{Optimised parameters for the two-variable decay models of stationary cylinder}.$ 

Model	а	α	β	p
MSE	0.70	0.69	0.64	-
$\operatorname{SPL}$	0.67	1.0	0.90	1.40



# Spatial Modes RMSE Plots

This appendix illustrates the RMSE plots for modes 5 to 15.

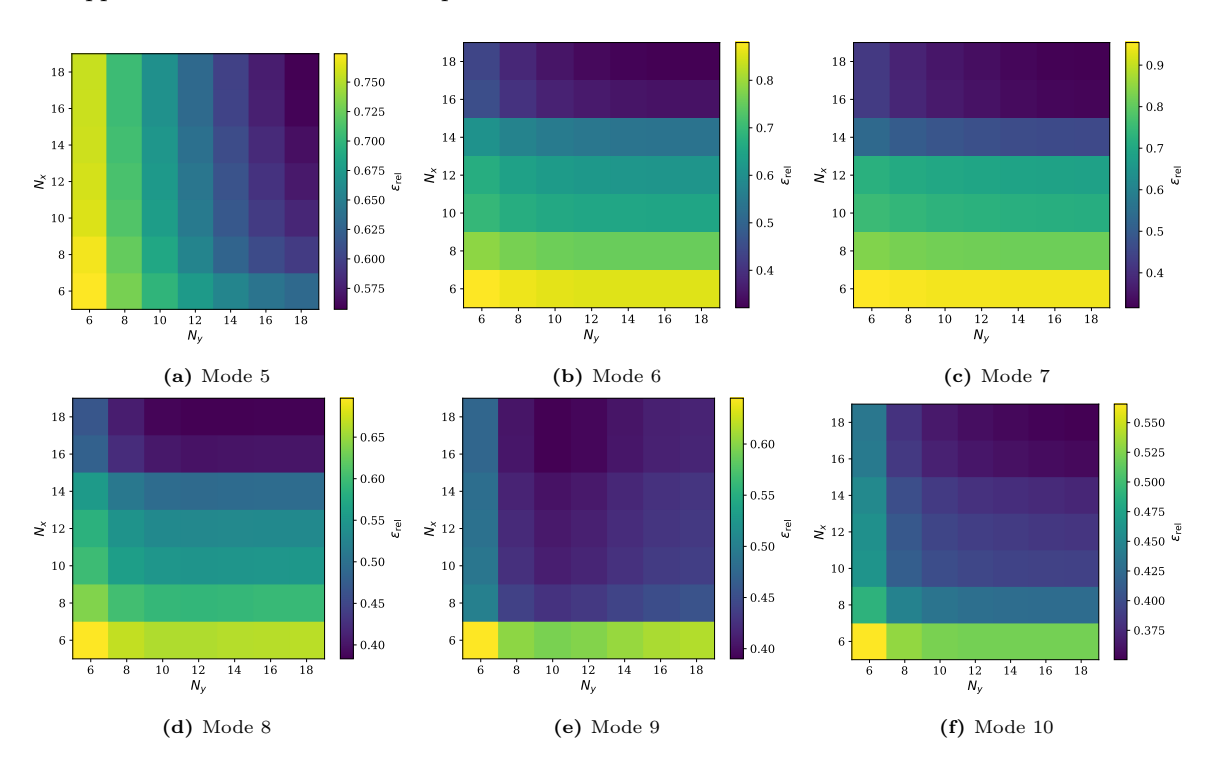
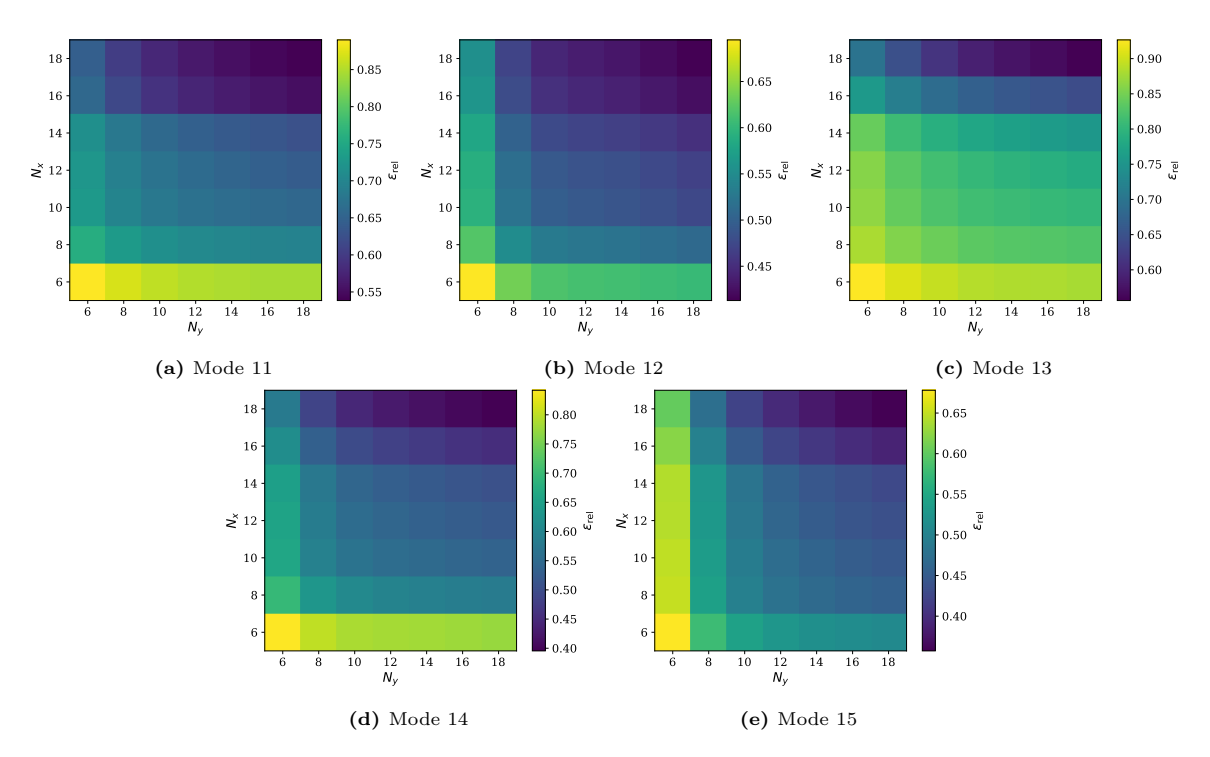


Figure F.1: RMSE for remaining spatial modes 5-10.



**Figure F.2:** RMSE for remaining spatial modes 11-15